Ph.D. thesis in physics

Spin-torque induced high frequency excitations and switching in spin-valve nanocontacts

by Dipl.-Phys. **Eike Moritz Eggeling**
born October 25th, 1980
in Warendorf, Germany

University of Bielefeld
Department of Physics
Thin Films and Physics of Nanostructures
Germany

AIT Austrian Instiute of Technology Vienna
Health and Enviroment Departement
Nanosystems
Austria

Dissertation zur Erlangung des Doktorgrades der Naturwissenschaften (Dr. rer. nat.) der Fakultät für Physik der Universität Bielefeld

Reviewers

Prof. Dr. Günter Reiss
Priv. Doz. Dr. Hubert Brückl

Date of submission: Mai 28th, 2012

Jury of Disputation

Prof. Dr. Günter Reiss
Priv. Doz. Dr. Hubert Brückl
Prof. Dr. Andreas Hütten
Prof. Dr. Peter Reimann

Date of Disputation: June 15th, 2012

Declaration

I wrote this thesis by myself and used none but the indicated resources.

Vienna, Mai 24th, 2012

Eike Moritz Eggeling

道

Contents

1 Introduction

1.1 Abstract

This thesis presents a novel spintronic design of a nano-sized high frequency oscillator, which is a cutting edge physics research field with a huge potential for future applications in the areas of mobile telecommunication and information- as well as in biomedical-technologies. In this device, a direct current flow through a nanocontact generates a spin polarized current in a spin-valve multilayer, which exerts a spin-transfer torque (STT) on the magnetic moments of a free magnetic layer. This torque can either cause the moments to switch their orientation or to drive them into a harmonic precession. The latter periodically modulates the voltage drop at the giant magnetoresistance (GMR) spin-valve multilayer patterned mesa in the sub-GHz frequency regime. Applications for the presented STT driven oscillator concept can be identified for example, as nano-sized high frequency source, as fast and non-volatile computer memory cell, or as nano-sized magnetic field sensor. The system provides clear advantages over the existing technological concepts of voltage controlled oscillators in terms of size, performance and dynamics.

This work in particular investigates the spin-torque-related dynamics of nonuniform magnetic vortex-like states in spin-valve nanocontacts, employing an unpinned artificial antiferromagnet as polarizer and amorphous CoFeB as free layer. Subgigahertz spectra are obtained for nanocontact radii of 40 to 130 nm. Low critical current density and reversibility of the dynamic spectra with respect to the current are obtained and compared to numerical and analytical models. The oscillation frequency, spectral power density and linewidth depend on the in-plane magnetic field and reach extreme values (i.e. maxima and minima) close to the free layer magnetization switching field. For certain field and current regimes metastable dynamic states are clearly demonstrated.

The influence of the magnetic free layer moment and of the nanocontact size on these spin-torque related phenomena are investigated. Different GMR multilayers are fabricated and subsequently optimized for magnetotransport performance. In this work three particular architecture types are presented, which show both current induced switching of the magnetic moments and, in certain cases, sub-GHz excitation dynamics related to magnetic vortex precession. The latter could only be observed for multilayers with a low magnetic moment amorphous CoFeB free layer and only for contact radii below 100 nm. The current and frequency dependence of the oscillation on the point contact radius and magnetic field is investigated and discussed with regard to a potential magnetic field sensor application in the nano scale. Additionally, multiple excitation modes are shown to exist at zero or small magnetic fields as a result of a highly inhomogeneous metastable magnetic state below the nanocontact.

The results of this thesis clearly demonstrate the feasibility of a nano-sized oscillation source and provided a detailed study of the key fabrication-, measurement- and performance-factors. Further, a numerical and analytical description of the basic physics phenomena is presented.

1.2 Kurzfassung

In der vorliegenden Doktorarbeit wird ein neuartiges spin-elektronisches Konzept eines nano-skaligen Oszillators (STO) vorgestellt, welches, sowohl aus der Sicht der aktuellen Grundlagen-forschung, als auch bezüglich möglicher praktischer Anwendung von hohem Interesse ist. In diesem Bauteil führt der direkte Elektronenfluss durch ein nanokontaktiertes magnetisches Spin-Ventil-Schicht-System zu einem spinpolarisierten Strom, der ein Drehmoment auf die Momente einer freien magnetischen Schicht ausübt. Dieses Drehmoment kann sowohl zu einem statis-chen Schalten der magnetischen Momente, als auch zu einer harmonischen Präzessionsbewegung führen. Im Fall einer Präzessionsbewegung wird an dem Schichtsystem eine periodische Mod-ulation des Riesenmagnetowiderstands im sub-GHz Frequenzbereich generiert. Anwendungen für ein solches Elektronenspin-getriebenes System finden sich zum Beispiel als ultrakompakte Hochfrequenzquelle im Bereich der mobilen Telekommunikation, als schnelle und zugleich nicht flüchtige Speicherzelle im Bereich der Datenspeicherung, oder als nanoskalieger Magnetfeldsen-sor im Bereich der Biologie- und Medizintechnik. Dabei verfügt der STO über klare Vorteile gegenüber derzeitig verwendeter Technologien bezüglich der Abmessungen, Betriebseigenschaften und Dynamik.

Der Fokus dieser Arbeit liegt in der Untersuchung der mit dem Elektronenspin-Moment verbundenen Dynamiken von wirbelartigen magnetischen Zuständen in nanokontaktierten Spin-Ventilen, die einen künstlichen Antiferromagneten als Polarisationsschicht und amorphes CoFeB als manipulierbare magnetische Schicht beinhalten. Spektren im sub-GHz Frequenzbereich wur-den für verschiedene Nanokontakt-Radien zwischen 40 und 130 nm erfasst. Äußerst geringe kri-tische Stromdichten und im Bezug zum Strom reversible Oszillationsdynamiken wurden gemessen und mit aktuellen numerischen und analytischen Modellen verglichen. Es zeigte sich eine Ab-hängigkeit von der Oszillationsfrequenz, der spektralen Leistungsdichte und der Linienbreite der Oszillationsdynamiken von den magnetischen Feldern in der Flächenebene, insbesondere nahe des Schaltfelds der Elemente.

Im Weiteren konzentriert sich diese Untersuchung auf den Einfluss des magnetischen Mo-ments der manipulierbaren Schicht und auf die Abhängigkeit des Nanokontakt-Radius auf die mit dem Elektronenspin Moment verbundenen Phänomene. Zu diesem Zweck wurden verschiedene Riesenmagnetowiderstands-Schichtsysteme hergestellt und auf ihre magnetischen Eigenschaften hin optimiert. Als Ergebnis wurden drei spezielle Schichtarchitekturen erreicht, die Strom-induziertes Schalten der magnetischen Momente sowie in speziellen Fällen auch Präzessionsdy-namiken zeigen. Letztere konnten nur für Schichtsysteme mit CoFeB als manipulierbare Schicht und für Nanokontakt-Radi unter 100 nm gemessen werden. Außerdem wurde die Abhängigkeit des Stroms und der Frequenz der Präzessionsdynamiken vom Nanokontakt-Radius auf parallel existierende Oszillationsmoden evaluiert, die aus den ausgeprägten inhomogenen metastabilen magnetischen Zuständen unter dem Nanokontakt resultieren.

Die Ergebnisse dieser Arbeit zeigen eindeutig die Realisierbarkeit einer nanoskaligen Oszil-

lationsquelle und liefern eine detaillierte Untersuchung der kritischen Fertigungs-, Mess- und Betriebsfaktoren. Darüber hinaus wird eine numerische und analytische Beschreibung der grundlegenden physikalischen Phänomene präsentiert.

1.3 General introduction

The spin-electronic (spintronic) is considered as the next evolutionary step in the technological progress of semiconductor electronics. The spintronic effectively combines both physical properties, the electron charge as well as the quantum-mechanical electron spin, in its novel devices, which have a high potential to initiate a new era of future technology. This thesis demonstrates a new spintronic design of a nano-sized electron spin driven oscillator, selected for one of the cover pages of the journal "physica status solidi - Rapid Research Letters" in a focus issue on spintronics (Fig. 1). Application areas for this system can be identified in the mobile telecommunication- and information- as well as biomedical-technology, i.e as nano-sized oscillation source [1, $^{Silva;JMMM;08}$], or as fast and non-volatile computer memory cell [2, $^{Kammerer;NatC;11}$], as well as magnetic field sensor [3, $^{Braganca;Nanot;10}$]. In such devices, driven by an electron spin-transfer torque (STT), a magnetic vortex precesses in a free magnetic layer of a giant-magnetoresistance (GMR) multilayer patterned mesa, periodically modulating the voltage drop at the multilayer in the sub-GHz to GHz frequency regime. Such a system provides clear advantages to existing voltage controlled oscillator concepts in terms of size, performance and dynamics.

The foundations of the STT theory were set in 1996, where Slonczewski [4, $^{Slonczewski;JMMM;96}$] and Berger [5, $^{Berger;PRB;96}$] independently predicted a new possibility to interact with the magnetization of a ferromagnetic layer in a magnetic multilayer, different to applying a magnetic field. They proposed that the transfer of the quantum-mechanical electron spin of a spin-polarized current flow perpendicular through the multilayer should, under certain conditions, be able to induce a magnetization change. Their predictions considered two possible types of STT induced magnetic dynamics, a switching type and a steady-state precession type. The existence of both phenomena could be evidenced in the following years [6, $^{Tsoi;PRL;98}$], [7, $^{Kiselev;Nat;03}$] and initiated a tremendous research effort in the field of spin-torque.

In the recent years, apart from single-domain spin-transfer oscillators (STOs) [8, $^{Lee;NatM;04}$], [9, $^{Rippard;PRL;04}$], the stable gyrotropic precession of a magnetic vortex in spin-valves with nanopillars [10, $^{Pribiag;NatP;07}$] and nanocontacts [11, $^{Pufall;PRB;07}$],[12, $^{Mistral;PRL;08}$] is of special interest. Such excitation occurs at low current densities, also in the absence of an external magnetic field [13, $^{Devolder;APL;09}$] and is associated with high emitted power and narrow linewidths, [14, $^{Dussaux;NatC;10}$] which are required in the mentioned applications of STOs as high frequency (HF) sources. Interest has grown further with the demonstration of phase-locking in double-point-contact nano-oscillators [15, $^{Mancoff;Nat;05}$],[16, $^{Kaka;Nat;05}$] and more recently the phase synchronization of vortices in an array of four nanocontacts, [17, $^{Ruotolo;NatN;09}$] lead-

ing to significant power amplification compared to a single contact. The incorporation of a perpendicular magnetized polarizer in the multilayer is shown to be beneficial for the switching [18, *Mangin;NatM;06*] and oscillation [19, *Houssameddine;NatM;07*] performance. Besides the all metallic GMR multilayers the spin-torque effect is demonstrated to exist in multilayers incorporating a crystalline tunneling barrier, showing the tunnel magnetoresistance (TMR) effect [20, *Sankey;NatP;08*],[21, *Kubota;NatP;08*],[14, *Dussaux;NatC;10*].

When the present thesis was started in 2007 the main question was how a new highly efficient spin-torque driven device can be build based on the existing knowledge. In the very beginning most of the necessary laboratory and measurement infrastructure was build. Based on the research results of the literature, point contact devices on GMR spin-valves with exchange
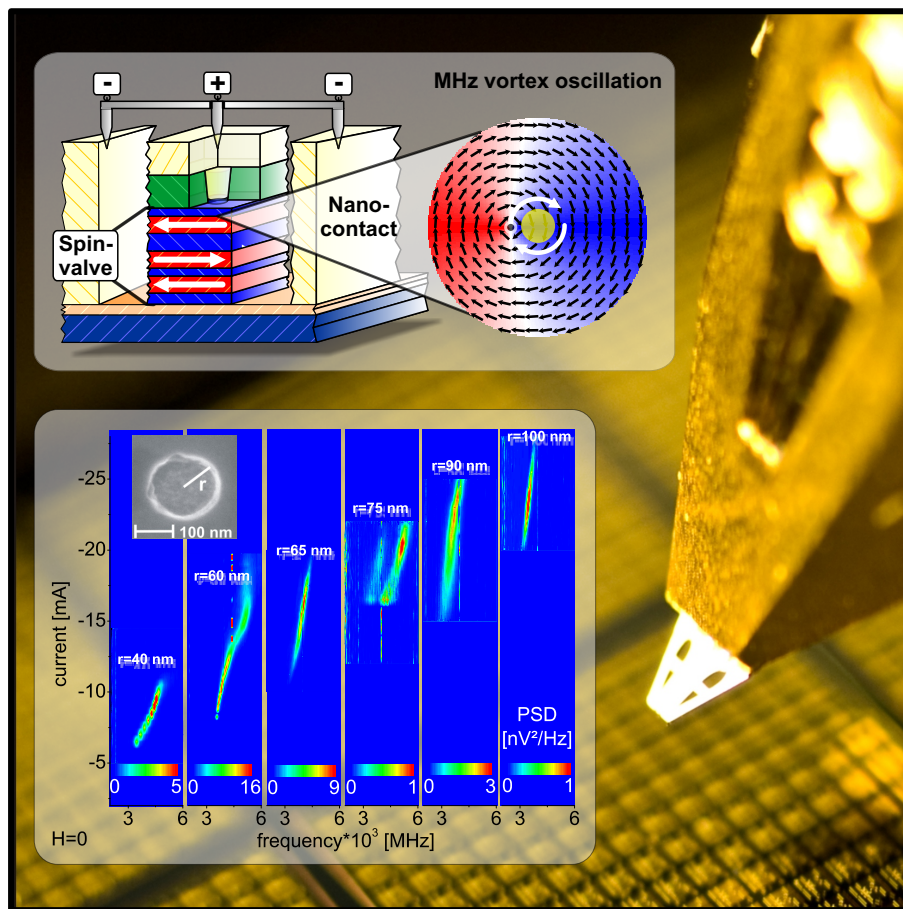
Figure 1: A nanocontact confines the current flow through a spin-valve multilayer (upper image). Spin-torque driven magnetic vortex dynamics are observed in dependence on the contact size and applied current, provoking microwave oscillations at zero magnetic field. The oscillation spectra (lower image) show the evolution of single and multiple radio frequency modes as a function of the contact size to be explained in this thesis. (adapted from [22, *Eggeling;BCover;11*])

biased polarizer and CoFe/NiFe free layer seemed to be a promising starting point for our investigation. These structures have been used to evaluate the fabrication process and to develop the measurement setup. On the other hand, at the time the motivation was to investigate low anisotropy, ferromagnetic CoFeB as free layer material, which is generally leading to high MR values and at the same time has a lower magnetic moment than polycrystalline CoFe films. In addition an artificial antiferromagnet as hard magnetic layer was investigated, which has not been employed before in STT nanocontact experiments. Moreover, of particular interest was the at the time unstudied influence of the nanocontact size on the excitation dynamics. At the end of this study, the motivation was to investigate the dependence of the oscillation frequency on external magnetic fields in perspective to a potential magnetic field sensor application.

1.4 Thesis outline

Chapter 2.1 introduces the basic theory background related to STT driven devices. First, the giant magnetoresistance effect in spin-valve multilayers is presented, followed by a basic description of ferromagnetic domain structures. A section regarding the most prominent magnetic thin film coupling mechanisms follows. The STT effect is then introduced and theoretically extended to the concept of STT driven vortex oscillations. The chapter concludes with a section on characteristic applications for STT devices.

In chapter 3, the most important experimental techniques relevant to this thesis are summarized, comprising different thin film deposition, lithography, etching and characterization techniques. The chapter concludes with two sections about the developed nano fabrication process and the built measurement setup.

The main experimental content of the present investigation on the STT induced high frequency excitations and switching in spin-valve nanocontacts is presented in chapter 4. First, the multilayer design and magnetotransport properties of spin-valve nanocontacts with natural and artificial antiferromagnet are presented in section 4.1. Subsequently, the transport measurements are discussed. The results of the measured STT driven vortex oscillations are investigated in section 4.2, while special focus is put onto the conditions for the existence of excitation. In the following sections the results on the vortex precession dependence on the nanocontact size are presented. Further, the influence of the free layer moment and the current induced switching effects are discussed. The chapter concludes with a section on numerical simulations of the spin-valve nanocontact system. In section 4.3 the influence of external magnetic fields along the easy- and hard-axis in-plane directions are presented. Further, the dependence of the oscillation frequency is discussed in regard to magnetic field sensing application in the nano scale. The chapter concludes with a section about the metastability observations and their submode structure. Finally, the results of this work are summarized and an outlook on the perspectives of STO devices is given in chapter 5.

References

[1] T.J. Silva and W.H. Rippard. Developments in nano-oscillators based upon spin-transfer point-contact devices. *Journal of Magnetism and Magnetic Materials*, 320(7):1260 – 1271, 2008.

[2] M. Kammerer, M. Weigand, M. Curcic, M. Noske, M. Sproll, A. Vansteenkiste, B. Van Waeyenberge, H. Stoll, G. Woltersdorf, CH. Back, and G. Schuetz. Magnetic vortex core reversal by excitation of spin waves. *Nat Commun*, 2:279–279, April 2011.

[3] B.A. Wilson J.A. Katine S. Maat P.M. Braganca, B.A. Gurney and J.R. Childress. Nanoscale magnetic field detection using a spin torque oscillator. *Nanotechnology*, 21(23):235202, 2010.

[4] J.C. Slonczewski. Current-driven excitation of magnetic multilayers. *J. Magn. Magn. Mater.*, L1:159, 1996.

[5] L. Berger. Emission of spin waves by a magnetic multilayer traversed by a current. *Phys. Rev. B*, 54:9353, 1996.

[6] J. Bass W.C. Chiang M. Seck V. Tsoi P. Wyder M. Tsoi, A.G.M. Jansen. Excitation of a magnetic multilayer by an electric current. *Phys. Rev. Lett.*, 80:4281, 1998.

[7] S. I. Kiselev, J. C. Sankey, I. N. Krivorotov, N. C. Emley, R. J. Schoelkopf, R. A. Buhrman, and D. C. Ralph. Microwave oscillations of a nanomagnet driven by a spin-polarized current. *Nature*, 425(6956):380–383, September 2003.

[8] K.-J. Lee, A. Deac, O. Redon, J.-P. Nozieres, and B. Dieny. Excitations of incoherent spin-waves due to spin-transfer torque. *Nat. Mater.*, 3(12):877–881, December 2004.

[9] W. H. Rippard, M. R. Pufall, S. Kaka, S. E. Russek, and T. J. Silva. Direct-current induced dynamics in $co_{90}fe_{10}/ni_{80}fe_{20}$ point contacts. *Phys. Rev. Lett.*, 92:027201, January 2004.

[10] V. S. Pribiag, I. N. Krivorotov, G. D. Fuchs, P. M. Braganca, O. Ozatay, J. C. Sankey, D. C. Ralph, and R. A. Buhrman. Magnetic vortex oscillator driven by d.c. spin-polarized current. *Nat Phys*, 3(7):498–503, July 2007.

[11] M. R. Pufall, W. H. Rippard, M. L. Schneider, and S. E. Russek. Low-field current-hysteretic oscillations in spin-transfer nanocontacts. *Phys. Rev. B*, 75:140404, April 2007.

[12] Q. Mistral, M. van Kampen, G. Hrkac, J.-V. Kim, T. Devolder, P. Crozat, C. Chappert, L. Lagae, and T. Schrefl. Current-driven vortex oscillations in metallic nanocontacts. *Phys. Rev. Lett.*, 100:257201, Jun 2008.

[13] P. Crozat C. Chappert M. Manfrini M. van Kampen W. Van Roy L. Lagae G. Hrkac T. Devolder, J.-V. Kim and T. Schrefl. Time-resolved zero field vortex oscillations in point contacts. *App. Phys. Lett.*, 95(1):012507, 2009.

[14] A. Dussaux, B. Georges, J. Grollier, V. Cros, A.V. Khvalkovskiy, A. Fukushima, M. Konoto, H. Kubota, K. Yakushiji, S. Yuasa, K.A. Zvezdin, K. Ando, and A. Fert. Large microwave generation from current-driven magnetic vortex oscillators in magnetic tunnel junctions. *Nat Commun*, 1:8–, April 2010.

[15] F. B. Mancoff, N. D. Rizzo, B. N. Engel, and S. Tehrani. Phase-locking in double-point-contact spin-transfer devices. *Nature*, 437(7057):393–395, September 2005.

[16] S. Kaka, M. R. Pufall, W. H. Rippard, T. J. Silva, S. E. Russek, and J. A. Katine. Mutual phase-locking of microwave spin torque nano-oscillators. *Nature*, 437(7057):389–392, September 2005.

[17] A. Ruotolo, V. Cros, B. Georges, A. Dussaux, J. Grollier, C. Deranlot, R. Guillemet, K. Bouzehouane, S. Fusil, and A. Fert. Phase-locking of magnetic vortices mediated by antivortices. *Nat Nano*, 4(8):528–532, August 2009.

[18] S. Mangin, D. Ravelosona, J. A. Katine, M. J. Carey, B. D. Terris, and Eric E. Fullerton. Current-induced magnetization reversal in nanopillars with perpendicular anisotropy. *Nat Mater*, 5(3):210–215, March 2006.

[19] D. Houssameddine, U. Ebels, B. Delaet, B. Rodmacq, I. Firastrau, F. Ponthenier, M. Brunet, C. Thirion, J.-P. Michel, L. Prejbeanu-Buda, M.-C. Cyrille, O. Redon, and B. Dieny. Spin-torque oscillator using a perpendicular polarizer and a planar free layer. *Nat Mater*, 6(6):447–453, Jun 2007.

[20] J. C. Sankey, Y.-T. Cui, J. Z. Sun, J. C. Slonczewski, R. A. Buhrman, and D. C. Ralph. Measurement of the spin-transfer-torque vector in magnetic tunnel junctions. *Nat Phys*, 4(1):67–71, January 2008.

[21] H. Kubota, A. Fukushima, K. Yakushiji, T. Nagahama, S. Yuasa, K. Ando, H. Maehara, Y. Nagamine, K. Tsunekawa, D. D. Djayaprawira, N. Watanabe, and Y. Suzuki. Quantitative measurement of voltage dependence of spin-transfer torque in mgo-based magnetic tunnel junctions. *Nat Phys*, 4(1):37–41, January 2008.

[22] M. Eggeling, T. Dimopoulos, R. Heer, and H. Brückl. back-cover rrl focus issue spintronics: Magnetic vortex excitation dependence on the magnetic free layer and size of spinvalve nanocontacts. *physica status solidi (RRL) - Rapid Research Letters*, doi: 10.1002/pssr.201190029, 2011.

2 Basic theoretical background for spin-torque driven devices

This chapter presents the basic theoretical concepts for spin-transfer torque (STT) driven devices. The giant magnetoresistance effect in spin-valve multilayers and the magnetic phenomena of the ferromagnetic domain structures are introduced. Subsequently, the most relevant magnetic thin film coupling mechanisms are discussed. Further, the STT effect is introduced and is then theoretically extended to the concept of STT driven vortex oscillations. Finally, characteristic applications for STT devices are summarized.

2.1 The giant magnetoresistance effect

In 2007 Peter Grünberg and Albert Fert were honored with the Nobel Prize in Physics for their independent discovery of the giant magnetoresistance (GMR) effect. In the late 1980s, they discovered and interpreted the physical phenomenon of very large magnetoresistance effects in thin film multilayers that can be influenced by magnetic fields [1, $^{Fert;RMP;08}$], [2, $^{RSAS;07}$]. This new magnetoresistive effect completely differed from the since 1856 known small anisotropic magnetoresistance (AMR) effect discovered by Thomson, where the resistance of a current flow through a ferromagnet is depending on whether a magnetic field is applied parallel or perpendicular to the flow direction [3, $^{Campbell;FM;82}$]. The GMR effect was quickly used for applications like magnetic disc read heads and as magnetic field sensor. Moreover, a new research field in physics was established: the spintronic.

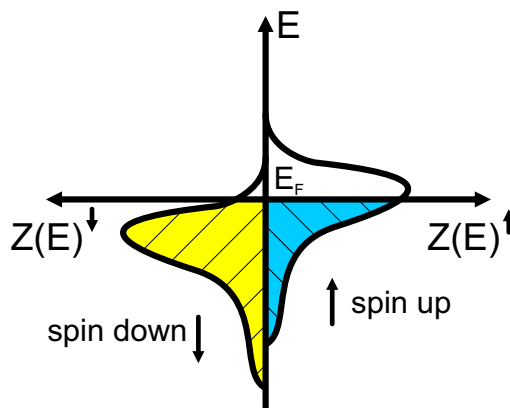Figure 2: Ferromagnetic materials show a large and unequal density of states $Z(E)$ for spin up and spin down electrons near the Fermi level E_F.

The physics of ferromagnetic materials play an important role for the understanding of the GMR effect. In contrast to dia- and paramagnetic materials, where randomly oriented magnetic moments order antiparallel or parallel to an applied magnetic field, ferromagnetic

materials exhibit a spontaneous magnetic order already at zero field. The ferromagnetism can be quantum mechanically modeled, based on the electronic band structure of the material in which the magnetism is caused by the exchange interactions of the electrons [4, $^{Guentheroth;99}$],[5, $^{Flude;95}$]. The latter are electrostatic in nature (Coulomb-interactions) in combination with the symmetry of the total wave function (Pauli principle).

The Pauli principle forces perfectly delocalized electrons of a specific band to "keep a certain distance" to electrons with parallel spins. This leads to a reduction in the Coulomb repulsion causing a gain in the electrons potential energy. If the band structure of the material is such that the gain in potential energy is larger than the kinetic energy necessary to adopt the parallel spin orientation, then ferromagnetic order is energetically favored. This is the case if the electron density of states is large at the Fermi energy (Fig. 2). Additionally, the exchange integral of the atoms, for which the electron clouds overlap, need to be large, i.g. a strong Coulomb interaction. In the Stoner-Model, the criterion for ferromagnetism is defined

$$I * Z^0(E_F) > 1 \ , \tag{2.1}$$

where I is the Stoner exchange parameter and $Z^0(E_F)$ is the density of states at the Fermi level. The 3d metals like Fe, Co and Ni fulfill this criterion at room temperature [6, $^{Mohn;03}$].
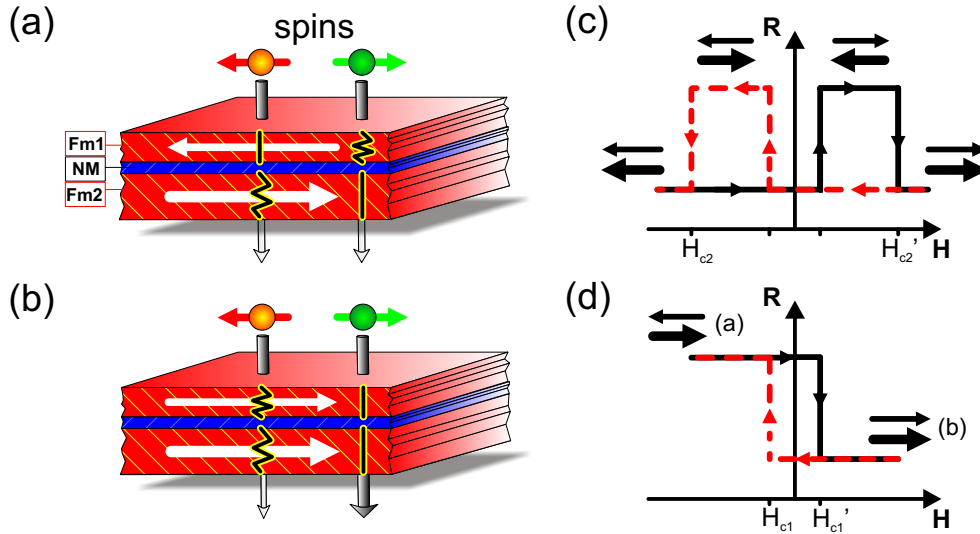

Figure 3: (a) For antiparallel aligned ferromagnetic (FM) layers both spin channels get equally scattered. (b) For parallel alignment only one spin channel gets strongly scattered. Major (c) and minor (d) resistance loops for the abrupt hysteretic switching of the layer magnetizations depending on the field-history.

If current flows through a thin layer of such a ferromagnetic material spin up and spin down electrons experience largely different resistances, mainly due to scattering processes at the differently populated density of states. This scattering dependence is utilized in a so called

spin-valve, which is formed by a multilayer system composed of two thin ferromagnetic layers separated by a nonmagnetic material. The layer with the lower magnetic rigidity is usually referred to as magnetic "free layer" and the one with the higher rigidity as "polarizer", since this layer is used to spin polarize the current flow, as we will see later. Figure 3(a) shows such a GMR spin-valve system with antiparallel orientation of the layer magnetizations (white arrows). For an electron current passing through the spin-valve the GMR effect defining phenomenon is that the total resistance of the stack is depending on the relative orientation of the FM layers magnetization directions, due to the different scattering probabilities of both spin channels. For an antiparallel alignment of the layer magnetizations the stack resistance is higher than for the parallel case (Fig. 3(b)). The major and minor resistance versus magnetic field loops in figure 3(c),(d) show abrupt hysteretic switching of the magnetization orientations at certain switching fields H_c. These switching loops are characteristic for the stack material composition and its micro magnetic structure, as well as for the geometrical sample architecture in regard to the applied magnetic field (chapter 2.2).
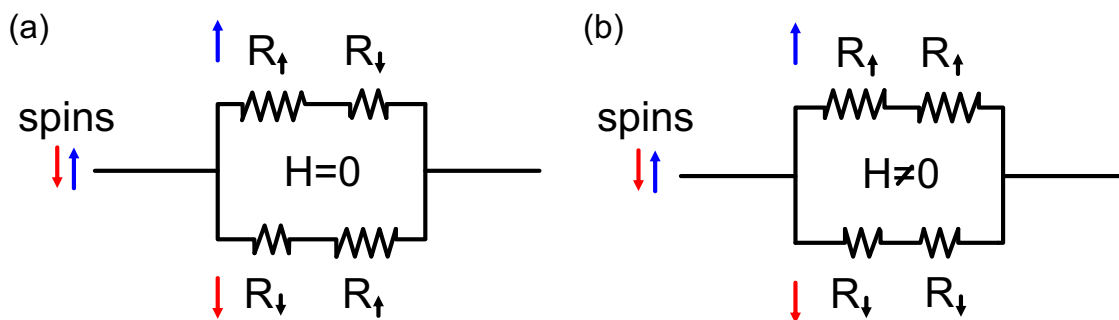

Figure 4: (a) Circuit diagram for antiparallel oriented layers at zero field. The magnetic layers are represented by resistences $R_\uparrow$ and $R_\downarrow$. (b) Circuit diagram for parallel oriented layers at non-zero field. Both figures are based on Ref. [2, [RSAS;07]].

The GMR effect can be understood from the circuit scheme depicted in Fig. 4, where the spin up and spin down resistances for the two magnetization alignments are shown. For the antiparallel orientation of the FM layers at zero field the total resistance, R_{ap}, adds up to

$$R_{ap} = \frac{(R_\uparrow + R_\downarrow) \cdot (R_\uparrow + R_\downarrow)}{R_\uparrow + R_\downarrow + R_\downarrow + R_\uparrow} = \frac{(R_\uparrow + R_\downarrow)^2}{2(R_\uparrow + R_\downarrow)} = \frac{(R_\uparrow + R_\downarrow)}{2} \ . \tag{2.2}$$

where $R_\uparrow$ and $R_\downarrow$ represent the layer resistances for the spin up and spin down currents, respectively. For the parallel orientation at a certain magnetic field the resistance sum, R_p, is

$$R_p = \frac{R_\uparrow R_\downarrow}{(R_\uparrow + R_\downarrow)} \ . \tag{2.3}$$

The difference between both equations defines the magneto resistance of the system

$$\Delta R = R_p - R_{ap} = -\frac{(R_\uparrow - R_\downarrow)^2}{2(R_\uparrow + R_\downarrow)} \ . \tag{2.4}$$

The giant magnetic resistance is commonly defined as

$$GMR[\%] = (\frac{R_{ap} - R_p}{R_p}) * 100 .$$

(2.5)

The effect is typically up to a few 10's of percent at room temperature.

2.2 Magnetic domains and hysteresis

The magnetic order of a ferromagnetic layer is subdivided into areas, so called domains, where the magnetic moments are aligned into one direction. The domains arrange in a way that minimizes the magnetic energy of the system. The magnetization direction of neighboring domains changes gradually in the domain walls. Generally, there are two types of domain walls existing, the Bloch wall and the Néel wall. The Bloch wall requires that some of the magnetic moment is oriented
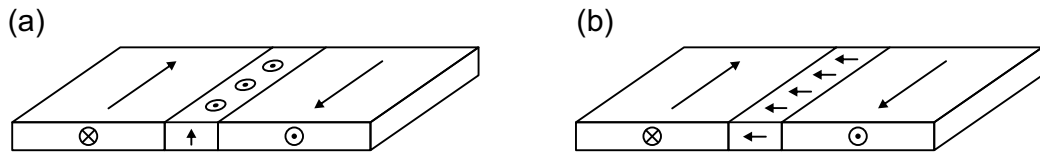

Figure 5: (a) Bloch wall with some magnetic moments pointing normal to the plane of the film. (b) Néel wall with all magnetic moments oriented in the film plane.

normal to the film plane (Fig. 5(a)). In the Néel wall, all moments are oriented in the plane (Fig. 5(b)). The application of a magnetic field H_{ext} can change the magnetization M, i.e. the domain orientation, in a hysteretic fashion (Fig. 6). The magnetic layer has reached its saturation when all moments are pointing into a single direction. The application of a magnetic field changes the
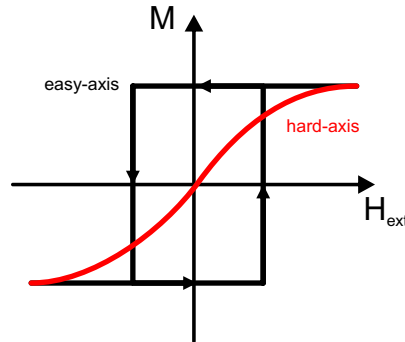

Figure 6: Easy- and hard axis switching curves.

micro domain state via domain wall movement and rotation. During the domain wall movement, domains with moments parallel to the external field grow on the expense of otherwise oriented domains. In a rotation-type of reversal, the magnetic domain magnetization rotates towards the field direction without any change in size.

The shape of the magnetization versus external field curve $M(H_{ext})$ depends on the magnetocrystalline anisotropy of the material, on the shape anisotropy for patterned films with lateral spatial restrictions and other types of anisotropies induced during deposition or post-deposition treatment in the presence of a magnetic field. The combination of various anisotropies give rise to an easy and hard magnetization axis, along which the magnetization reversal is governed by different processes. Figure 6 illustrates the two extreme cases for easy- and hard-axis switching.

2.3 Thin film magnetic coupling mechanisms

Several types of coupling effects can be observed in magnetic thin film systems, which influence the hysteresis curves of spin-valve multilayers. Of special interest for the present work are coupling mechanisms that enhance the magnetic rigidity of a ferromagnet in order to make it most insensitive to the external magnetic field. In the following, prominent types of coupling mechanisms are summarized.

I) A frequently used coupling mechanism to enhance the rigidity of a spin-valve is the so called exchange bias, which describes a type of unidirectional exchange anisotropy that is caused by a coupling between a ferro- and antiferromagnetic material. The origin of the effect is assumed to be the exchange coupling of the magnetic moment fine structure close to the interfaces of the FM and AF, since the AF bulk presents no net magnetic moment (Fig. 7(a)). The effect was discovered in 1956 by W.H. Meiklejohn and C.P. Bean [7, $Meiklejohn;PR;56$].
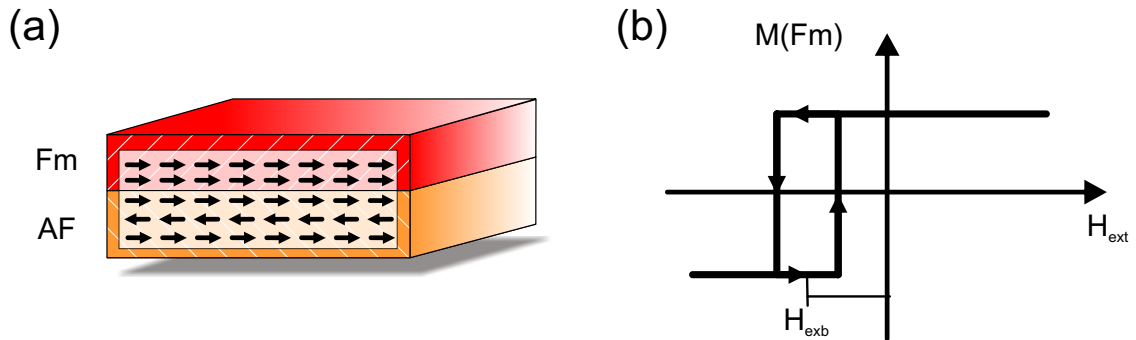
Figure 7: (a) Pinning of the magnetic moments of a ferromagnetic layer FM to the moments of an antiferromagnet at layer interfaces. (b) The coupling effect shifts the magnetic minor loop.

The so called pinning of the FM to the AF is experimentally realized in a field cooling procedure. The material composition needs to be chosen in a way that ensures that the critical temperature necessary to destroy the magnetic order of the AF (Néel temperature)

is below the one for the FM material (Curie temperature). In the first procedure step the stack containing the FM and AF is heated above the Néel temperature and subsequently, a high magnetic field is applied to saturate the FM layer. In a next step the temperature is decreased with this applied "cooling" field below the AF's Néel temperature. The exchange interaction close to interfaces cause the magnetic moments of the AF to align to the field induced order of the FM layer. This treatment generally results in a biased hysteresis curve like it is depicted in figure 7(b), which is shifted in the negative/opposite direction of the cooling field.

The exchange bias is shown to be equivalent to the assumption of an unidirectional anisotropy energy term [8, $^{Thomas;03}$]:

$$E = HM_s cos\theta - K_u cos\phi + ... \qquad (2.6)$$

where θ is the angle between magnetization and applied field vector H, M_s is the saturation magnetization of the FM, K_u is the unidirectional anisotropy constant per unit volume and ϕ is the angle between the applied field and the direction of the cooling field. If the cooling field and applied field are aligned, solutions of this equation lead to an effective field H':

$$H' = H - K_u/M_s. \qquad (2.7)$$

The exact description of the effects origin down to the nano scale is still subject of ongoing research activity.

II) Instead of employing an AF to enhance the polarizer rigidity, it is also possible to use an artificial antiferromagnet (AAF) (Fig. 8(a)), which couples two FMs by means of the so called Ruderman-Kittel-Kasuya-Yosida (RKKY) coupling. The latter can cause ferromagnetic or antiferromagnetic coupling depending on the thickness of the spacing layer between the FMs. The effect can be explained by a conducting electron model, which sets up the magnetization orientation in FM layers [9, $^{Parkin;PRL;91}$]. In this work an asymmetric type of AAF is employed, meaning that the FM layers present unequal thicknesses. This difference leads to a net magnetic moment of the AAF:

$$m_{net}^{AAF} = m_1 - m_2 = M_1 t_1 - M_2 t_2 , \qquad (2.8)$$

where $M_{1,2}$ are the magnetic moments and $t_{1,2}$ are the thicknesses of the FMs.

The general switching behavior of the AAF under the influence of a magnetic field can be understood in an simple model assuming a coherent rotation of single domain state (Stoner-Wohlharth model [10, $^{Stoner;PT;48}$]) like it is sketched in figure 8(a). The energy per unit area, E, of the AAF system can then be defined as [11, $^{Dieny;JP;90}$],[12,

Folkerts;JMMM;91],[13, *Wiese;06*]:

$$E = - \underbrace{J_{lin}cos(\varphi_1 - \varphi_2) - J_{bq}cos^2(\varphi_1 - \varphi_2)}_{E_C} + \underbrace{K_1 t_1 sin^2\varphi_1 + K_2 t_2 sin^2\varphi_2}_{E_A}$$
$$- \underbrace{\mu_0 H(M_1 t_1 cos\varphi_1 + M_2 t_2 cos\varphi_2))}_{E_Z} ,$$

where E_C is the coupling energy, E_A is the anisotropy energy, E_Z is the Zeeman energy, $\varphi_{1,2}$ are the angles between the layer magnetization vectors and the applied field direction, J_{lin} and J_{bq} are linear and quadratic interlayer exchange coupling parameters and K_1 and K_2 are the uniaxial anisotropy constants per unit volume. The numerical solution [14, *Dimopoulos;02*] of the energy minimization of the equation in terms of φ_1 and φ_2 is summarized in figure 8(b) and illustrates the switching cycle for both magnetic moment vector orientations from negative to positive saturation.
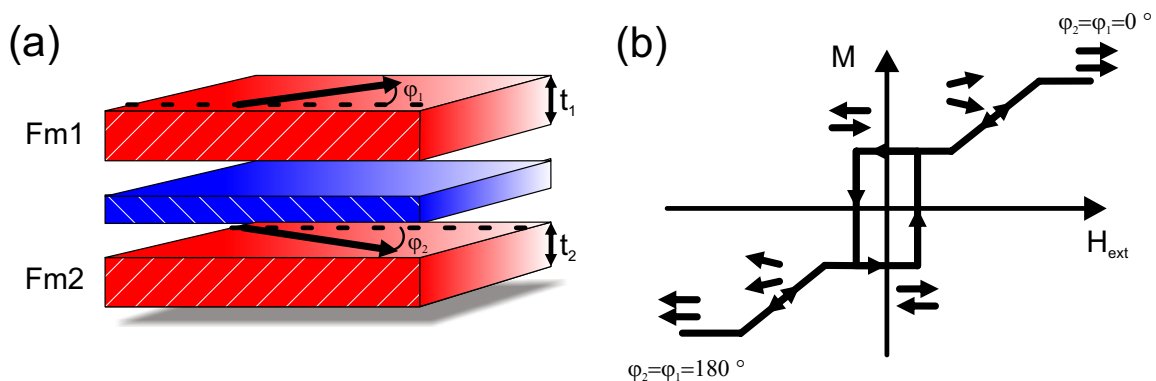

Figure 8: (a) Sketch of an artificial antiferromagnet. (b) Switching loop of an artificial antiferromagnet (based on [14, *Dimopoulos;02*]).

Figure 9 shows the measurement of the AF coupling strength as a function of the Ru thickness for AAFs of CoFe(1.5)/Ru(x nm)/CoFe(2.5), where the value of the AF coupling is given by [14, *Dimopoulos;02*]):

$$J_{AF} = -H_{sat}\frac{M_1 t_1 M_2 t_2}{M_1 t_1 + M_2 t_2} . \tag{2.9}$$

For the samples of this work the second coupling maximum is employed (0.76 nm Ru).
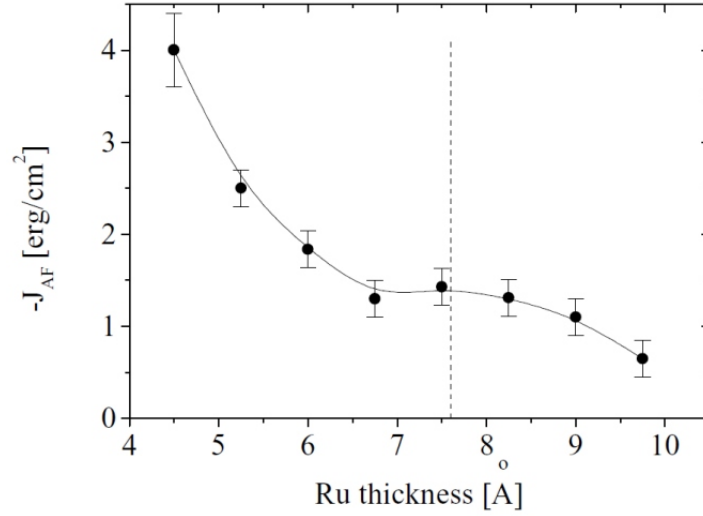
Figure 9: AF coupling strength vs Ru thickness for AAFs of CoFe(1.5)/Ru(x nm)/CoFe(2.5) (taken from [14, *Dimopoulos;02*]).

III) Another mechanism type is the Néel coupling (also referred to as orange-peel coupling), which is caused by the topographic roughness of the multilayers [15, *Neel;AP2;67*]. The sketch in figure 10(a) illustrates such a GMR double multilayer where the individual layer roughness is correlated. The latter causes magnetic dipoles to couple the layers ferromagnetically, as it is shown in figure 10(b). This kind of coupling, often appearing between the spin-valve free layer and polarizer, is minimized in this work by the optimization of the spin-valve buffer roughness (see chapter 4.1).
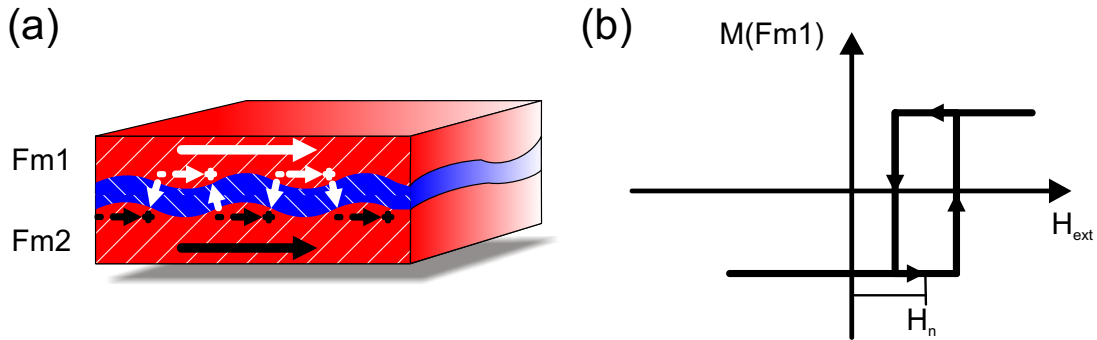

Figure 10: (a) Orange-peel coupling caused by correlated roughness of ferromagnetic layer Fm1 and Fm2. (b) Magnetic minor loop for Orange-peel coupled layers.

IV) Another magnetostatic coupling type for small structure sizes is the dipole coupling at the ferromagnetic layer edges (Fig. 11(a)), which is present in nanosized pillar structures. The flux closure at edges leads to a reduction of the systems magnetic energy and is therefore energetically favored [16, $^{Moon;99}$]. The effect can lead to an antiferromagnetic coupling of the layers like it is presented in figure 11(b).
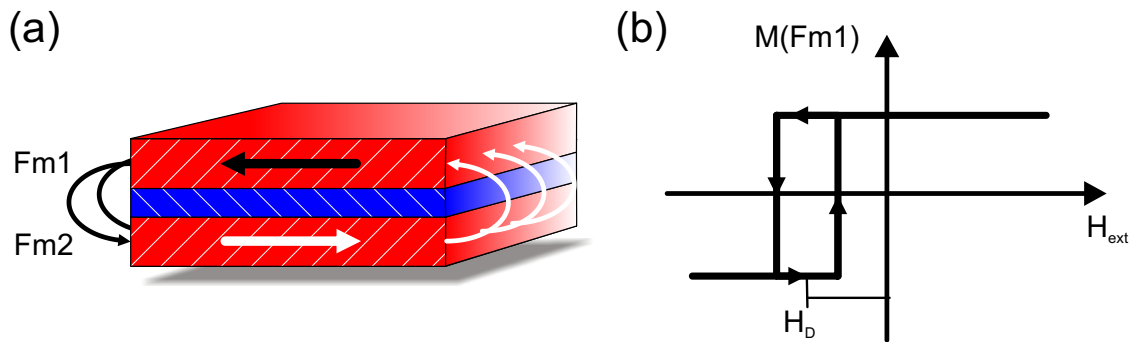

Figure 11: (a) Dipole coupling at the sample edges leads for small structures to antiferromagnetic type of coupling. (b) Magnetic minor loop for dipole coupled layers.

2.4 The spin-transfer torque effect

In contrast to the conventional manner of manipulating the magnetization of a magnetic multilayer by means of a magnetic field, it is under certain conditions possible to change the magnetization profile directly by a current flow perpendicular to the layers. This change can be caused by the transfer of spin angular momentum from a spin polarized current to the magnetic moments of the incorporated ferromagnets, an effect which was theoretically predicted by Slonczewski [17, *Slonczewski;JMMM;96*] and Berger [18, *Berger;PRB;96*] independently in 1996. Their predictions considered two possible types of magnetic dynamics that spin-transfer torque can excite, a switching type and steady-state precession type. The first measurement of spin-transfer torque induced resistance changes in point contacts were made by Tsoi et al. in 1998 [19, *Tsoi;NatP;98*]. Five years later Kiselev et al. [20, *Kiselev;Nat;03*] observed the spin-torque driven high-frequency precession type for the first time in spin-valve pillars (geometries see Fig.14(a)(b)).

In the following the basics of the spin-transfer torque effect will be defined in regard to a macrospin model of the ferromagnets incorporated in the magnetic multilayer. In this approximation the magnetization of a layer is assumed to be spatially uniform throughout its motion and can therefore be treated as a single macrospin. This approximation is afterwards extended to the dynamic precession of a rigid vortex magnetization profile in the spin-valve free layer. An introduction to a further theoretically investigation of the phenomena in terms of micromagnetic modeling of the macrospin dynamics can be found in Ref. [21, *Ralph;JMMM;08*].

2.4.1 Macrospin definition of the spin-transfer torque

We assume a spin polarized current, for which the spin polarization vector forms an angle with the magnetization of the ferromagnet (FM) trough which it passes. This results to a torque exerted on the spin current tending to align its polarization to the FM's magnetization. Due to the conservation of momentum an equal but opposite torque is exerted on the ferromagnet moments - the so called spin-transfer torque. For large enough spin current density it is possible to manipulate the orientation of the FM's magnetization via this spin-torque. Figure 12(a) illustrates this effect for a nanosized spin-valve pillar.

Figure 12(b) shows a vector model of the electron current flow from the free layer to the polarizer perpendicular through the spin-valve structure for an almost parallel alignment of free layer magnetization, $\vec{m}$, and polarizer magnetization, $\vec{M}$. The magnitude of this current flow can be written as

$$I = I_{up} + I_{down} , \qquad (2.10)$$

where I_{up} and I_{down} represent the currents carried by spin-up and spin-down electrons. Outside the spin-valve structure the spin components are randomly orientated in spin space, as a result, the current shows no spin polarization. In a simplified model[1] it is assumed that spins parallel oriented to the polarizer transmit through its nonmagnet-ferromagnet interface and antiparallel

---

[1]ferromagnetic band structure related scattering effects are discussed in chapter 2.1.
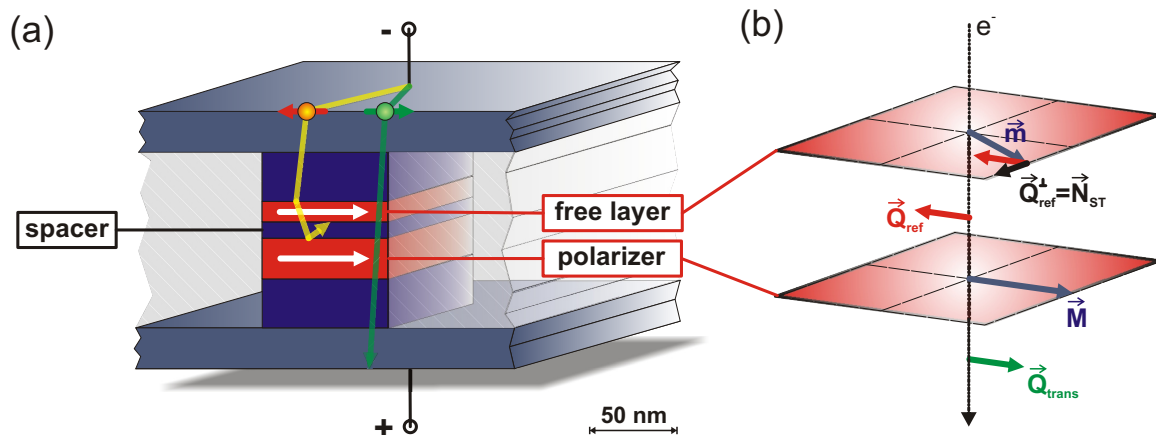
Figure 12: (a) Current flow for both spin channels through a nanosized GMR spin-valve pillar. (b) Vector model of the spin-transfer torque created by a spin polarized current.

spins become totally reflected by scattering events (any polarization effects at the free layer are neglected). For this reason at the polarizer-spacer interface a spin current

$$\vec{Q}_{ref} = I_{up}\vec{s}_{up} - I_{down}\vec{s}_{down} = \eta(\theta)\frac{I\hbar}{2e}\vec{M}_u \qquad (2.11)$$

is formed in antiparallel direction to $\vec{M}$, where $\vec{s}_{up}$ and $\vec{s}_{down}$ represent the unit vectors of the spin-up and spin-down directions, $\vec{M}_u$ is the unit vector in $\vec{M}$ direction, $\hbar$ is Plank's constant, e is the electron charge and the current polarization $\eta(\theta)$ is

$$\eta(\theta) = \frac{(I_{up} - I_{down})}{I_{up} + I_{down}} \,, \qquad (2.12)$$

depending on the angle, θ, between the magnetization vectors $\vec{m}$ and $\vec{M}$ [22, [Xiao;06]]. The spin polarized current $\vec{Q}_{ref}$ is back scattered into the free layer and can be separated in two in-plane vector components, one parallel and one perpendicular to the free layer moment vector $\vec{m}$. The perpendicular component represents the spin-transfer torque which exerts on the free layer moment

$$\vec{Q}_{ref}^{\perp} = \vec{N}_{ST} = \eta(\theta)\frac{I\hbar}{2e}\vec{m} \times (\vec{M} \times \vec{m}) \,. \qquad (2.13)$$

For an electron current flow from the free layer to the polarizer this torque pulls $\vec{m}$ away from $\vec{M}$. For opposite current polarity the same assumptions lead to a spin-torque pointing into the opposite direction, pulling $\vec{m}$ into parallel alignment with $\vec{M}$. The spin-torque definition in formula 2.13 was first proposed by Slonczewski for a ballistic current-driven excitation in magnetic multilayers [17, [Slonczewski;JMMM;06]] and is widely used in the literature.

2.4.2 Spin-transfer torque and the Landau-Lifschitz-Gilbert equation

The dynamic motion of a magnetic moment in an effective magnetic field, H_{eff}, and under the influence of a spin-current can be described by the Landau-Lifschitz-Gilbert equation in addition

to the spin-torque term defined in equation 2.13

$$\frac{\partial \vec{m}}{\partial t} = \underbrace{-\gamma_0 \vec{m} \times \vec{H}_{eff}}_{precession} + \underbrace{\alpha(\vec{m} \times \frac{\partial \vec{m}}{\partial t})}_{damping} + \underbrace{\vec{N}_{ST}}_{spin-torque} \quad , \qquad (2.14)$$

where γ_0 is the gyromagnetic ratio and α is the Gilbert damping [23, $^{Kim;CM;10}$]. In a spontaneous generated effective magnetic field without any spin-torque contribution, the magnetic moment $\vec{m}$ starts to precess around H_{eff} on a damped spiral trajectory until it aligns parallel. The spin-torque, $\vec{N}_{ST}$ counteracts to the damping and can manipulate the moment trajectory. A rightly balanced, continuously exerting spin-torque can stabilize an stable angular precession around H_{eff} (Fig.13(a)). Another trajectory is possible when a strong easy-plane anisotropy
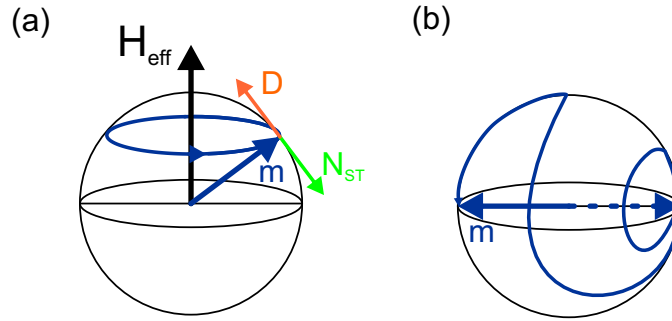

Figure 13: (a) Vector model for the terms in the Landau-Lifschitz-Gilbert equation for stable precession conditions. (b) A current pulse can switch magnetization direction.

and a weaker uniaxial anisotropy with two stable static magnetic states is assumed. A current pulse of a certain strength can then cause a large angle precession to develop, after which the moment relaxes to a 180 degree reversed direction (Fig. 13(b)). A current pulse of opposite polarity can switch the moment back into its previous direction. It should be noted here, that in this macrospin approach all angular momentum is assumed to be absorbed by the magnetic moment and any effect of orbital moments is ignored, as well as any temperature influence. A more rigorous approach can be found in Ref. [24, $^{Sun;JRD;06}$],[21, $^{Ralph;JMMM;08}$].

2.4.3 Spin-transfer torque and device geometries

In order to establish a spin current density sufficient enough to manipulate the moments of the spin-valve free layer the typical technological approach is to narrow the lateral current flow cross-section through the multilayer either employing the architecture of a pillar (Fig. 14(a)) or of a point-contact (Fig. 14(b)). The fabrication is either achieved mechanically by a tip-contact [19, $^{Tsoi;NatP;98}$] or by lithographical patterning and etching of the spin-valve multilayer (see chapter 3.5). The high spin-current density leads to the generation of a high in-plane Oersted field, H_{Oe}, which must be taken into account for the development of micromagnetic dynamics. For typical
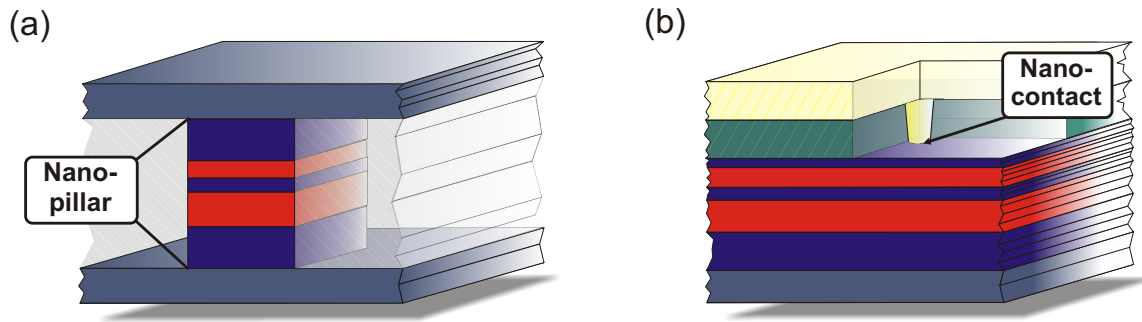
(a)

(b)

Nano-
pillar

Nano-
contact

Figure 14: Schematic of a rectangular pillar (a) and point-contact (b) geometry for spin-valve multilayer.

materials and lateral dimension larger than approximately 250 nm in diameter the Oersted field contribution is expected to be much stronger than the spin-transfer force, prohibiting any spin-torque dynamics [21, $^{Ralph;JMMM;08}$]. In chapter 4.2.5 this influence on the magnetic spin-valve layers is simulated in detail.

The main advantage of the point contacts geometry in comparison to pillar devices is that the excitation falls into the for many applications interesting sub-GHz to low GHz frequency regime even at zero external magnetic field and its relatively narrow oscillation linewidth. On the other hand, these excitations need a higher spin current density to be initialized, because of the spin-torque needed to manipulate a domain, which is strongly coupled to the overall magnetization of the extended free layer [21, $^{Ralph;JMMM;08}$].

In order to achieve high spin-torque efficiencies, the optimization of the spin-valve stack and its nanostructuring have been the subject of intensive research activity. For instance, instead of all-metallic spin-valves, magnetic tunnel junctions have been employed, incorporating an MgO tunneling barrier, which leads to a much higher current spin polarization and therefore higher spin-torque efficiency [25, $^{Sankey;NatP;08}$],[26, $^{Dussaux;NatC;10}$],[27, $^{Sun;JMMM;08}$]. On the other hand, to obtain the necessary high current densities, ultra thin tunneling barriers have to be incorporated that are technologically far more challenging to realize compared to all metallic spin-valves. Another possible improvement is the incorporation of an out-of-plane polarizer, which has been shown to increase the spin-torque effect significantly in terms of switching [28, $^{Mangin;NatM;06}$] and precession [29, $^{Houssameddine;NatM;07}$] performance. The pinning of the polarizer is also an important factor for the device performance. The incorporation of two differently pinned polarizers on top and below the free layer is shown to increase the spin-torque efficiency [30, $^{Berger;JAP;03}$]. For an array of point contacts, phase locking of two and more closely spaced oscillators could be shown to increase the output power of the devices significantly [31, $^{Kaka;Nat;05}$],[32, $^{Ruotolo;NatN;09}$]. Besides the activities in spin-valve multilayers the spin-torque effects can as well be found in nanostructures like ferromagnetic wires, where the spin-torque is

under certain conditions able to move domain walls in the wire. A summary of this research field can be found in Ref. [33, $^{Beach;JMMM;08}$].

2.5 Spin-transfer driven vortex oscillations

A magnetic vortex is the lowest energy configuration of magnetic structures just above the single domain length scale [34, $^{Shinjo;S;00}$],[35, $^{Wachowiak;S;02}$]. Such a vortex state can be driven into highly coherent sub-GHz to GHz steady-state oscillation via a direct spin-polarized current in pillar [36, $^{Pribiag;Nat;07}$] and point contact [37, $^{Mistral;PRL;08}$] devices. Figure 15 illustrates such a vortex oscillation of the magnetization profile in a nanosized disc. There are several attempts in the recent years to analytically and numerically model the vortex dynamics in order to explain the experimental findings for pillars [38, $^{Ivanov;PRL;07}$],[39, $^{Guslienko;CM;09}$],[40, $^{Khvalkovskiy;APL;09}$],[26, $^{Dussaux;NatC;10}$] and point contacts [37, $^{Mistral;PRL;08}$],[41, $^{Berkov;PRB;09}$], [23, $^{Kim;CM;10}$]. Some of the most challenging parts are the correct theoretical description of the nucleation mechanism of single and multi-mode excitations and the exact implementation of the spatially varying spin-transfer torque components in the multilayer, as well as the detailed influences of the Oersted field and temperature on the systems [42, $^{Stiles;SDCMS;06}$]. All models
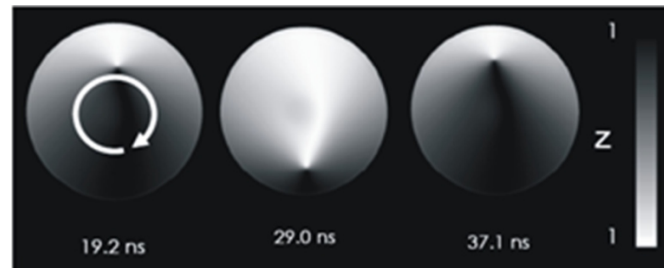

Figure 15: Simulation of a magnetic vortex core oscillation in a circular disc (taken from Ref. [43])

are based primarily on a formalism using a modification of Thiele's equation to describe the motion of a rigid vortex entirely in terms of the core position in the film-plane. Figure 16(a) illustrates such an oscillation model for a pillar geometry at high perpendicular magnetic field and zero temperature, described by the following equation [26, $^{Dussaux;NatC;10}$]:

$$\underbrace{\vec{G} \times \frac{d\vec{X}}{dt}}_{\vec{F}_G} - \underbrace{\frac{\partial W}{\partial \vec{X}}}_{\vec{F}_R} - \underbrace{\hat{D}\frac{d\vec{X}}{dt}}_{\vec{F}_\alpha} + \vec{F}_{ST} = 0 \ , \tag{2.15}$$

where $\vec{G} = -2\pi p L M_s/\gamma e_z$ is the gyrovector, p is the core polarity, L is the thickness, M_s is the saturation magnetization, γ is the gyromagnetic ratio and e_z is the unit vector along the normal direction, $W(\vec{X})$ is the potential of the off-center vortex with the core position $\vec{X}$ and $\hat{D}$ is the damping dyadic. The first two terms, corresponding to the gyrotropic force $\vec{F}_G$ and restoring
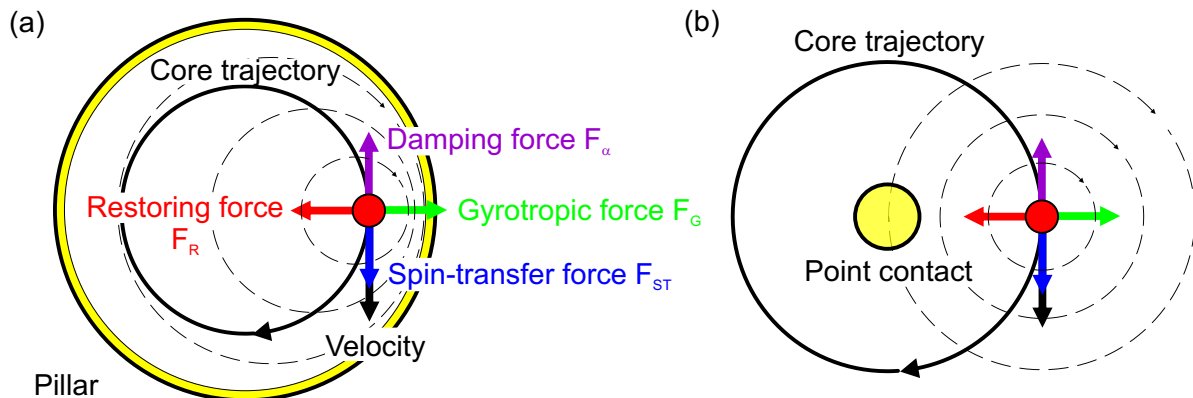
Figure 16: (a) Vortex core oscillation for a circular pillar geometry and high perpendicular field (based on Ref. [26, $^{Dussaux;NatC;10}$]). (b) Model of magnetic vortex core oscillation for a point contact geometry.

force $\vec{F}_R$, respectively are radial with respect to the vortex trajectory. Their balance sets the frequency of motion. The last two terms, corresponding respectively to viscous damping, $\vec{F}_\alpha$ and spin-transfer force, $\vec{F}_{ST}$ are tangent to the trajectory. Their compensation sets the amplitude of the orbit for a fixed and uniform polarizer [26, $^{Dussaux;NatC;10}$]. In the case of a fixed and uniform polarizer, this model leads to expressions for the spin-transfer force

$$F_{ST} = \sigma\pi J p_z M_s La e_\chi \tag{2.16}$$

and the damping force

$$F_\alpha = -2\pi\alpha\eta\frac{M_s}{\gamma}\omega La p e_\chi \ , \tag{2.17}$$

where $\sigma = \hbar P_{spin}/2\,|e|\,LM_s$ with P_{spin} being the spin polarization of the current, J is the current density (defined as positive for electrons flowing from free layer to the polarizer), a is the orbit radius and e_χ is the unit vector tangential to the orbit of the core, p_z is the out-of-plane component of the polarizer, α is the damping constant, $\eta\hat{E} = \hat{D}/\alpha G$ is a damping parameter, $\hat{E}$ is a unit tensor, and $\omega = 2\pi f$ is the rotational speed. An expression for the fraction of the critical current density for the onset of sustained vortex oscillation, J_c, and the oscillation frequency can be derived by equalizing equation 2.16 and 2.17 to [26, $^{Dussaux;NatC;10}$]:

$$\frac{f}{J_c} = \frac{1}{8\pi}(\frac{\gamma\hbar P}{eLM_s\alpha\eta})p_z \ . \tag{2.18}$$

This dependence is shown to be in excellent agreement with measurements performed on TMR spin-valve pillars under the influence of high perpendicular magnetic field [26, $^{Dussaux;NatC;10}$].

The main difference of a point contact to a pillar device is the extended free layer, which is not confining the vortex motion to a short range boundary (Fig. 16(b)). Experimental investigations for point contacts show that even at zero applied magnetic field the nucleation and oscillation

of a magnetic vortex is possible [44, $^{Devolder;APL;09}$],[45, $^{Manfrini;APL;09}$],[46, $^{Kampen;JPD;09}$],[47, $^{Eggeling;APL;11}$]. Also the vortex nucleation current density and the spectral linewidth is different compared to pillars. The quality factor of the point contact oscillation is typically about one order of magnitude smaller than the one for measurements of pillar spin-valves. A theory describing the dynamics in the point contact geometry needs to take into account these phenomena.

Kim et al. first suggested a theoretical model for nanocontact excitations existing only for perpendicular to the sample-plane applied magnetic fields [37, $^{Mistral;PRL;08}$] and in a later work for zero applied magnetic field, where they assume the vortex oscillations to stem from in-plane spin-torques [23, $^{Kim;CM;10}$]. The only condition in this model for a self-oscillatory state in nanocontact is the existence of a vortex in the system. Therefore they predict no critical current for the onset of oscillation. In this theory the spin-torque relevant for the point contact geometry is divided into two components

$$F_{ST} = F_{CPP} + F_{CIP} \, , \tag{2.19}$$

one perpendicular-to-plane (CPP) and one in-plane (CIP). These torques are caused by the corresponding CPP and CIP current flows under the point contact (Fig. 17). Without the application of a magnetic field the authors assume that CIP-spin-torques are the dominant mechanism for self-sustained vortex oscillations for large orbits in the point contact geometry. This theory assumes a force constellation similar to the one depicted in figure 16(b), where the
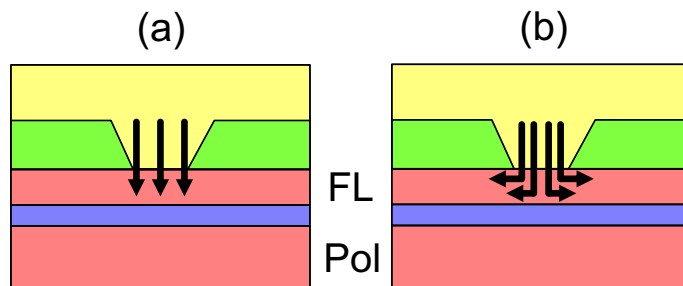

Figure 17: Spin polarized current flow component perpendicular-to-plane (a) and in-plane (b). (based on [23, $^{Kim;CM;10}$])

conic structure of the Zeeman potential, which is caused by the current generated Oersted field, leads to a force that pulls the vortex towards the nanocontact center, while the nonadiabatic spin torque counteracts this force pushing the vortex radially outwards. The torque acts as a "boost" along the circular trajectory of the vortex orbit, while Gilbert damping acts to oppose this motion. According to the model the orbit radius is independent of the applied current and nanocontact size, and depends only on material parameters. Further, their theory predicts physical solutions only for one current polarity, which corresponds to the case where the electrons flow outward from the nanocontact. They intuitively interpret this current flow as outward "pressure" exerted by the spin torques that counterbalances the Gilbert damping and therefore prevents the vortex

spiraling into the contact center, which corresponds to the position of energy minimum in the Zeeman energy.

The frequency of the vortex oscillation is found to vary linearly as a function of current and is assumed to be

$$\omega \cong \frac{\kappa \, |I|}{GR_0} \, , \tag{2.20}$$

where $\omega = 2\pi f$ is the gyration frequency, $\kappa < 1$ is a correction factor, I is the current, G is the magnitude of the gyrovector and R_0 is the stationary orbit radius. The power-spectrum is described by a Lorentzian lineshape with a linewidth (FWHM)

$$\Delta\omega_{LT} = \Delta\omega_0(1 + \nu^2) \, , \tag{2.21}$$

where $\Delta\omega_0$ is a "linear" linewidth proportional to the temperature and $\nu = \alpha D/G$ is a "non-linearity" parameter with the damping dyadic D [23, $^{Kim;CM;10}$]. At higher temperatures their model predicts an inhomogeneously broadening of the line shape due to fluctuations in the orbital radius, causing a Gaussian lineshape, with a current-dependent linewidth that varies like $\sqrt{I}$.

2.6 Characteristic applications

The spin-transfer torque effect can be applied to create a wide range of nano-devices with potential application as nano-sized microwave oscillation sources, ultra compact magnetic field sensors or fast and nonvolatile memory cells.
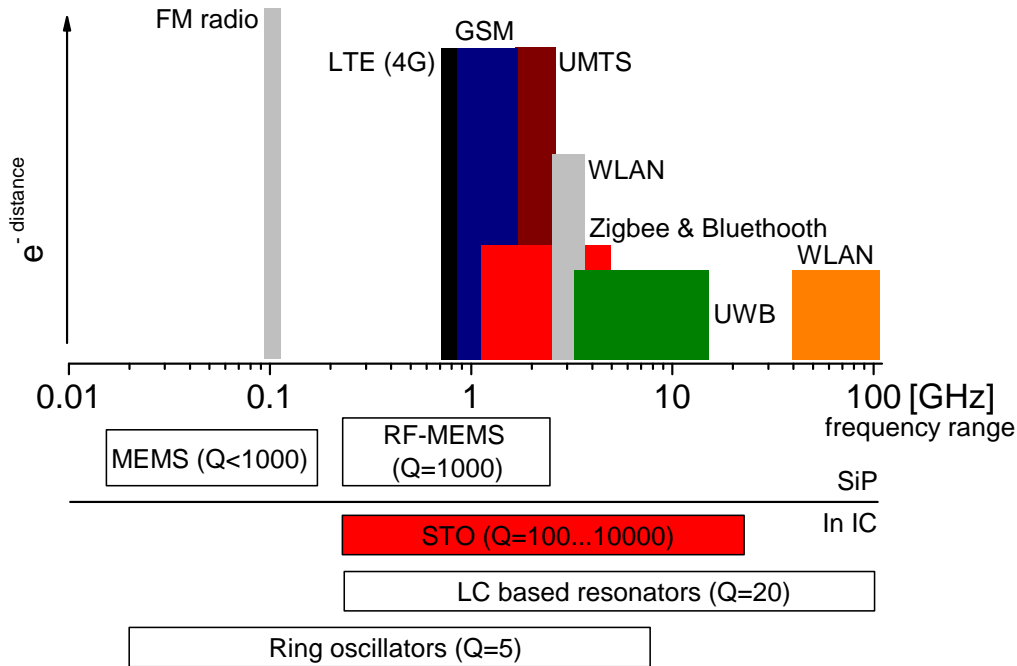

Figure 18: Frequency spectrum from 10 MHz to 100 GHz in comparison to communication application regimes and oscillation source concepts. Interesting application for spin-torque oscillators (STOs) are mobile telephone standards, like the Global System for Mobile Communications (GSM), the Universal Mobile Telecommunications System (UMTS) and Long Term Evolution standard (LTE). STOs could as well be used for near field communications, for frequencies within the Zigbee or Bluetooth standards and for ultra wide band (UWB) applications or wireless local area network (WLAN). The high quality factor and low cost of planar integrated circuit (IC) STOs are advantages to LC based voltage-controlled-oscillators and system-in-package (SiP) micro-electro-mechanical (MEM) devices (based on [48, [VanRoy;08]]).

Microwave oscillation from 200 MHz to several tens of GHz with a linewidth as narrow as 1 MHz at a frequency of 0.8 GHz can be generated with nanopilar and point contact devices [26, [Dussaux;NatC;10]],[49, [Silva;JMMM;08]]. These can serve as current tunable oscillation sources for next generation telecommunication devices, e.g. for mobile GSM, UMTS or wireless LAN modules as well as for near field communication like Bluetooth or Zigbee (see Fig. 18). Additionally,

STOs could potentially be applied for on-chip clocks, wireless chip-to-chip as well as wireless on chip communication, as microwave-mixer, or for phased-array transceivers [50, $^{Wolf;JRD;06}$] and GHz frequency detectors are possible [51, $^{Sankey;PRL;06}$]. With an active source device size[2] in the order of several μm^2 a new design dimension can be entered (for example a 10 μm^2 shaped multilayer could contain easily an array of 10×10 nanocontacts). This size is up to three orders of magnitude smaller than existing devices, like for instance voltage controlled oscillators (VCOs) or micro-electro-mechanical (MEMs) oscillators (see Tab. 1). Beside the exceptional size STOs can provide advantages in terms of agility, quality factors and tunable range in comparison to the standard technologies (Tab. 1).

The main remaining technological challenge at present is the still low output power of a single STO device, even if a perpendicular magnetic field is applied, e.g., for fields of 5 kOe the output power is in the order of several nW in a good case [26, $^{Dussaux;NatC;10}$]. This is still approximately three orders of magnitude too low for practical applications [52, $^{Katine;JMMM;08}$]. Multiple element synchronization and an improved stack design, especially TMR stacks with high spin-transfer efficiencies may prove the solution to overcome this problem.

$f = 5 - 10$ GHz	VCO-LC	VCO-L high k	RF MEMS	VCO-STO
Size	500 μm^2	1 mm^2	1 mm^2	1-10 μm^2
Quality factor Q	18 (classical on chip inductor)	100 (enhanced inductor)	1000	> 1000
Tunable range	20 %	10 %	1 %	10-100 %
Agility	microseconds	microseconds		nanoseconds
Output power	- 10 dBm	0 dBm	0 dBm	**$<$ - 15 dBm**

Table 1: *Comparison of the STO to other existing oscillator technologies (based on Ref. [48, $^{VanRoy;08}$]).*

The magnetic field dependence of the oscillation properties, especially of all the oscillation frequency, can lead to the development of field sensors, which could be applied for read heads of magnetic disk drives, biosensing applications like magnetic bead detection, as well as for magnetic imaging [53, $^{Braganca;NT;10}$].

Magnetic memory cells is another large field for applications using the spin-torque effect. One of the most recent findings is the possibility to store information in the orientation of a magnetic vortex core, which can be switched by current pulses leading to the reversal due to induced vortex oscillation dynamics [54, $^{Kammerer;NatC;11}$] and is an advancement of a previous version of similar storage concept [55, $^{Waeyenberge;Nat;06}$]. A different memory concept is the spin-torque-magnetic-random-access-memory ST-MRAM (or SMT-MRAM) in which the orientation of a free magnetic layer can be directly switched by the spin-transfer torque (see chapter 2.4).

---

[2]without any electric connections lines

The information is encoded in the magnetoresistive state of the GMR or TMR element. For

	Standard MRAM (90 nm)*	DRAM (90 nm)†	SRAM (90 nm)†	SMT-MRAM (90 nm)*	FLASH (90 nm)†	FLASH (32 nm)†	SMT-MRAM (32 nm)*
Cell size (μm^2)	0.25 256 Mb/cm	0.25 256 Mb/cm	1–1.3 64 Mb/cm	0.12 512 Mb/cm	0.1 512 Mb/cm	0.02 2.5 Gb/cm	0.01 5 Gb/cm
Read time	10 ns	10 ns	1.1 ns	10 ns	10–50 ns	10–50 ns	1 ns
Program time	5–20 ns	10 ns	1.1 ns	10 ns	0.1–100 ms	0.1–100 ms	1 ns
Program energy per bit	120 pJ	5 pJ Needs refresh	5 pJ	0.4 pJ	30–120 nJ	10 nJ	0.02 pJ
Endurance	$>10^{15}$	$>10^{15}$	$>10^{15}$	$>10^{15}$	$>10^{15}$ read, $>10^6$ write	$>10^{15}$ read, $>10^6$ write	$>10^{15}$
Nonvolatility	yes	no	no	yes	yes	yes	yes

*MRAM performance values projected by the authors.
†Values from the International Technology Roadmap for Semiconductors (ITRS).

Figure 19: Projected performance of MRAM an ST-MRAM, including the performance of conventional semiconductor memories DRAM, SRAM and FLASH (taken from Ref. [50, $Wolf;JRD;06$])

the resistance read-out a current below the switching threshold is applied. The advantage of the ST-MRAM to competing memory designs is that it combines the properties of fast read and write speed at low power consumption with nonevolitibility of the information at zero current. The ST-MRAM concept provides a much better scalability and much lower switching current in respect to prior evolutionary MRAM concepts e.g., the toggle MRAM or standard MRAM, which use current-generated magnetic fields to rotate the magnetization of the free layer [50, $Wolf;JRD;06$]. The table in Figure 19 shows some of these key features of the ST-MRAM in comparison to competing memory concepts, like DRAM, SRAM and FLASH.

Apart from these concepts, magnetic domain wall movement could lead to magnetic logic on chip components, as well as to the so called race track memory, where the spin-transfer torque of a current flow through a wire drives magnetic domain walls in and out of a detection area. There, the information is decoded in the domain orientation with respect to a GMR element and can be written by large external fields i.g., from a domain wall stray field [50, $Wolf;JRD;06$]. This concept could lead to an exceptional high information density.

References

[1] A. Fert. Nobel lecture: Origin, development, and future of spintronics. *Reviews of Modern Physics*, 80:1517, 2008.

[2] The Royal Swedish Academy of Sciences (Kungl. Vetenskapsakademien). The discovery of giant magnetoresistance. *AAPPS Bulletin*, 17(6), December 2007.

[3] I.A. Campbell and A. Fert. Transport properties of ferromagnets. *Ferromagnetic Materials, ed. E. P. Wohlfarth (Nord-Holland, Amsterdam)*, Vol. 3:p. 747, 1982.

[4] U. Rüdiger G. Güntheroth. *Magnetische Schichtsysteme - Magnetische Festkörper*. Institut für Festkörperforschung des Forschungszentrum Jülich Gmbh. Jülich, 1999.

[5] P. Flude. *Electron Correlations in Molecules and Solids*. Springer New York, 1995.

[6] P. Mohn. *Magnetism in the Solid State*. Springer-Verlag, Berlin, Heidelberg, 2003.

[7] W. H. Meiklejohn and C. P. Brean. New magnetic anisotropy. *Phys. Rev.*, 102:1413, 1956.

[8] A. Thomas. *Preparation and characterisation of magnetic single and double barrier junctions*. PhD thesis, University of Bielefeld, 2003.

[9] S.S.P. Parkin. Systematic variation of the strength and oscillation period of indirect magnetic exchange coupling trough the 3d, 4d, and 5d transition metals. *Phys. Rev. Lett.*, Vol. 67:p. 3598, 1991.

[10] E.P. Wohlfarth E.C. Stoner. *Philos. Trans. R. Soc. London Ser. A*, 240:599, 1948.

[11] J. P. Gavigan B. Dieny and J. P. Rebouillat. Magnetisation processes, hysteresis and finite-size effects in model multilayer systems of cubic or uniaxial anisotropy with antiferomagnetic coupling between adjacent ferromagnetic layers. *Journal of Physics: Condensed Matter*, 2:159, 1990.

[12] W. Folkerts. Calculated magnetic phase diagrams and magnetoresistance curves for an antiferromagnetically coupled multilayer system. *J. Magn. Magn. Mater.*, 94:302, 1991.

[13] N. Wiese. *Coupling phenomena and scalability of CoFeB/Ru/CoFeB sandwiches*. PhD thesis, Fakultät für Physik der Universität Bielefeld, 2006.

[14] T. Dimopoulos. *Transport polarisé en spin dans les jontions tunnel magnétiques: Le role des interfaces métal/oxyde dans le processus tunnel*. PhD thesis, Université Louis Pasteur de Strasbourg, 2002.

[15] L. Néel. *Ann. Phys. 2*, 61, 1967.

[16] J.R.E. Fontana K.-S. Moon and S.S.P. Parkin. Exchange-biased magnetic tunnel junctions: Dependence of offset field on junction width. *Applied Physics Letters*, 74:3690, 1999.

[17] J.C. Slonczewski. Current-driven excitation of magnetic multilayers. *J. Magn. Magn. Mater.*, L1:159, 1996.

[18] L. Berger. Emission of spin waves by a magnetic multilayer traversed by a current. *Phys. Rev. B*, 54:9353, 1996.

[19] J. Bass W.C. Chiang M. Seck V. Tsoi P. Wyder M. Tsoi, A.G.M. Jansen. Excitation of a magnetic multilayer by an electric current. *Phys. Rev. Lett.*, 80:4281, 1998.

[20] S. I. Kiselev, J. C. Sankey, I. N. Krivorotov, N. C. Emley, R. J. Schoelkopf, R. A. Buhrman, and D. C. Ralph. Microwave oscillations of a nanomagnet driven by a spin-polarized current. *Nature*, 425(6956):380–383, September 2003.

[21] D.C. Ralph and M.D. Stiles. Spin transfer torques. *Journal of Magnetism and Magnetic Materials*, 320(7):1190 – 1216, 2008.

[22] J. Xiao. *Spin-transfer torque in magnetic nanostructures*. PhD thesis, School of Physics Georgia Institute of Technology, 2006.

[23] T. Devolder J.-V. Kim. Theory of the power spectrum of spin-torque nanocontact vortex oscillators. *cond-mat.mtrl-sci*, arXiv:1007.3859v1, 2010.

[24] J.Z. Sun. Spin angular momentum transfer in current-perpendicular nanomagnetic junctions. *IBM Journal of Research and Development*, Vol. 50(No. 1), January 2006.

[25] J. C. Sankey, Y.-T. Cui, J. Z. Sun, J. C. Slonczewski, R. A. Buhrman, and D. C. Ralph. Measurement of the spin-transfer-torque vector in magnetic tunnel junctions. *Nat Phys*, 4(1):67–71, January 2008.

[26] A. Dussaux, B. Georges, J. Grollier, V. Cros, A.V. Khvalkovskiy, A. Fukushima, M. Konoto, H. Kubota, K. Yakushiji, S. Yuasa, K.A. Zvezdin, K. Ando, and A. Fert. Large microwave generation from current-driven magnetic vortex oscillators in magnetic tunnel junctions. *Nat Commun*, 1:8–, April 2010.

[27] J.Z. Sun and D.C. Ralph. Magnetoresistance and spin-transfer torque in magnetic tunnel junctions. *Journal of Magnetism and Magnetic Materials*, 320(7):1227 – 1237, 2008.

[28] S. Mangin, D. Ravelosona, J. A. Katine, M. J. Carey, B. D. Terris, and Eric E. Fullerton. Current-induced magnetization reversal in nanopillars with perpendicular anisotropy. *Nat Mater*, 5(3):210–215, March 2006.

[29] D. Houssameddine, U. Ebels, B. Delaet, B. Rodmacq, I. Firastrau, F. Ponthenier, M. Brunet, C. Thirion, J.-P. Michel, L. Prejbeanu-Buda, M.-C. Cyrille, O. Redon, and B. Dieny. Spin-torque oscillator using a perpendicular polarizer and a planar free layer. *Nat Mater*, 6(6):447–453, Jun 2007.

[30] L. Berger. *J. Appl. Phys.*, 93:7693, 2003.

[31] S. Kaka, M. R. Pufall, W. H. Rippard, T. J. Silva, S. E. Russek, and J. A. Katine. Mutual phase-locking of microwave spin torque nano-oscillators. *Nature*, 437(7057):389–392, September 2005.

[32] A. Ruotolo, V. Cros, B. Georges, A. Dussaux, J. Grollier, C. Deranlot, R. Guillemet, K. Bouzehouane, S. Fusil, and A. Fert. Phase-locking of magnetic vortices mediated by antivortices. *Nat Nano*, 4(8):528–532, August 2009.

[33] M. Tsoi G.S.D. Beach and J.L. Erskine. Current-induced domain wall motion. *Journal of Magnetism and Magnetic Materials*, 320(7):1272 – 1281, 2008.

[34] T. Shinjo, T. Okuno, R. Hassdorf, K. Shigeto, and T. Ono. Magnetic vortex core observation in circular dots of permalloy. *Science*, 289(5481):930–932, 2000.

[35] A. Wachowiak, J. Wiebe, M. Bode, O. Pietzsch, M. Morgenstern, and R. Wiesendanger. Direct observation of internal spin structure of magnetic vortex cores. *Science*, 298(5593):577–580, 2002.

[36] V. S. Pribiag, I. N. Krivorotov, G. D. Fuchs, P. M. Braganca, O. Ozatay, J. C. Sankey, D. C. Ralph, and R. A. Buhrman. Magnetic vortex oscillator driven by d.c. spin-polarized current. *Nat Phys*, 3(7):498–503, July 2007.

[37] Q. Mistral, M. van Kampen, G. Hrkac, J.-V. Kim, T. Devolder, P. Crozat, C. Chappert, L. Lagae, and T. Schrefl. Current-driven vortex oscillations in metallic nanocontacts. *Phys. Rev. Lett.*, 100:257201, Jun 2008.

[38] B. A. Ivanov and C. E. Zaspel. Excitation of spin dynamics by spin-polarized current in vortex state magnetic disks. *Phys. Rev. Lett.*, 99:247208, December 2007.

[39] J. M. Gonzalez K. Y. Guslienko, G. R. Aranda. Spin torque and critical currents for magnetic vortex nano-oscillator in nanopillars. *cond-mat.other*, arXiv:0912.5521v1, 2009.

[40] A.V. Khvalkovskiy, J. Grollier, A. Dussaux, K.A. Zvezdin, and V. Cros. Vortex oscillations induced by spin-polarized current in a magnetic nanopillar: Analytical versus micromagnetic calculations. *Phys. Rev. B*, 80:140401, October 2009.

[41] D. V. Berkov and N. L. Gorn. Spin-torque driven magnetization dynamics in a nanocontact setup for low external fields: Numerical simulation study. *Phys. Rev. B*, 80:064409, August 2009.

[42] Miltat J. Stiles M. D. Spin transfer-torques and daynamics. *Spin Dyn Confined Magn Struct III*, 101:225–308, 2006.

[43] Imec. *http://www.imec.be/tunamos/public/results_files/image008.jpg*.

[44] P. Crozat C. Chappert M. Manfrini M. van Kampen W. Van Roy L. Lagae G. Hrkac T. Devolder, J.-V. Kim and T. Schrefl. Time-resolved zero field vortex oscillations in point contacts. *App. Phys. Lett.*, 95(1):012507, 2009.

[45] M. Manfrini, T. Devolder, Joo-Von Kim, P. Crozat, N. Zerounian, C. Chappert, W. Van Roy, L. Lagae, G. Hrkac, and T. Schrefl. Agility of vortex-based nanocontact spin torque oscillators. *APL*, 95(19):192507, 2009.

[46] M. van Kampen, L. Lagae, G. Hrkac, T. Schrefl, J.-V. Kim, T. Devolder, and C. Chappert. Current-driven vortex oscillations in metallic nanocontacts: zero-field oscillations and training effects. *Journal of Physics D: Applied Physics*, 42(24):245001, 2009.

[47] M. Eggeling, T. Dimopoulos, T. Uhrmann, O. Bethge, R. Heer, V. Hoink, and H. Bruckl. Low spin current-driven dynamic excitations and metastability in spin-valve nanocontacts with unpinned artificial antiferromagnet. *Applied Physics Letters*, 98(4):042504 –042504–3, January 2011.

[48] W. Van Roy. Spinswitch workshop spin momentum transfer cracow. In *SPIN TRANSFER TORQUE POINT CONTACTS AND NANOPILLARS*, IMEC, Kapeldreef 75, B-3001 Leuven, Belgium, 2008.

[49] T.J. Silva and W.H. Rippard. Developments in nano-oscillators based upon spin-transfer point-contact devices. *Journal of Magnetism and Magnetic Materials*, 320(7):1260 – 1271, 2008.

[50] S. A. Wolf, A. Y. Chtchelkanova, and D. M. Treger. Time-resolved measurement of spin-transfer-driven ferromagnetic resonance and spin torque in magnetic tunnel junctions. *IBM Journal of Research and Development*, 7(1):101 –110, January 2006.

[51] J. C. Sankey, P. M. Braganca, A. G. F. Garcia, I. N. Krivorotov, R. A. Buhrman, and D. C. Ralph. Spin-transfer-driven ferromagnetic resonance of individual nanomagnets. *Phys. Rev. Lett.*, 96(22):227601, Jun 2006.

[52] J.A. Katine and Eric E. Fullerton. Device implications of spin-transfer torques. *Journal of Magnetism and Magnetic Materials*, 320(7):1217 – 1226, 2008.

[53] B.A. Wilson J.A. Katine S. Maat P.M. Braganca, B.A. Gurney and J.R. Childress. Nanoscale magnetic field detection using a spin torque oscillator. *Nanotechnology*, 21(23):235202, 2010.

[54] M. Kammerer, M. Weigand, M. Curcic, M. Noske, M. Sproll, A. Vansteenkiste, B. Van Waeyenberge, H. Stoll, G. Woltersdorf, CH. Back, and G. Schuetz. Magnetic vortex core reversal by excitation of spin waves. *Nat Commun*, 2:279–279, April 2011.

[55] B. Van Waeyenberge, A. Puzic, H. Stoll, K. W. Chou, T. Tyliszczak, R. Hertel, M. Fahnle, H. Bruckl, K. Rott, G. Reiss, I. Neudecker, D. Weiss, C. H. Back, and G. Schutz. Magnetic vortex core reversal by excitation with short bursts of an alternating field. *Nature*, 444(7118):461–464, November 2006.

3 Fabrication and characterization techniques

In this chapter the most important experimental techniques are summarized, introducing different thin film deposition, lithography, etching and characterization techniques. Subsequently, two sections about the developed nano fabrication process and the custom built measurement setup follow.

3.1 Deposition techniques

The fabricated devices comprise of thin films with thicknesses between 250 and 0.8 nanometers, which are deposited by a combination of physical magnetron sputtering and plasma enhanced chemical vapor deposition (PECVD). The following two sections present the used process parameters for both employed systems.

3.1.1 Sputter deposition

In this work a special customized Leyboldt UNIVEX cluster sputter machine with two deposition chambers and 11 target positions is utilized (Fig. 20). The system incorporates six 4" and two 3" DC magnetron sources, as well as two 4" HF magnetron sources. The distance between the targets and the sample holder is approximately 10 cm. The holder position below the target is ether hold statically or is set into a dynamic oscillating motion to increase the homogeneity of the deposition over the sample area. Table 2 contains the process parameters used for the

Figure 20: Leyboldt UNIVEX cluster sputter machine with two deposition chambers.

spin-valve multilayer deposition in this thesis. Detailed descriptions of the sputtering process can be found in [1, $^{Hilleringmann;99}$],[2, $^{Wehner;83}$] and [3, $^{Maissel;83}$].

Sputter target positions	11 magnetron (9 DC and 2 HF)
Standard base pressure	$1 \cdot 10^{-7}$ mbar
Sputter gas	Ar
Gas inlet pressure	(DC) 2 μbar, (HF) 5 μbar
Gas flow rates	6 sccm
Source power	(DC) 20 W, (HF) 150 W
Source Voltage	200-300 V
Sample holder temperature	Cooled to room temperature
Used materials	(dynamic (D) or static (S) sputter rates [nm/min])
- Magnetic alloys (DC)	$Co_{70}Fe_{30}$ (D 1.2), $Co_{40}Fe_{40}B_{20}$ (D 1.1),
	$Ni_{80}Fe_{20}$ (D 1.8), $Ir_{83}Mn_{17}$ (D 2.9)
- Metals (DC)	Cu (D 3.4), Ru (D 1.4), Ta (D 1.7),
	Au (S 22.5)
- Insulator (HF)	MgO (D 0.5)

Table 2: List of sputter parameters used for this work.

3.1.2 Plasma enhanced chemical vapor deposition

Interesting for this work is the plasma enhanced chemical vapor deposition (PECVD) of SiN_4 as insulating material, often used in manufacturing of integrated circuits [1, $^{Hilleringmann;99}$]. Such a film shows about 10^6 to 10^{15} $\Omega \cdot cm$ and a dielectric strength of 1 to 5 MV/cm [4, $^{Sze;07}$]. The deposition is carried out in an Oxford Instruments Plasmalab 100 PECVD machine, operated under cleanroom conditions (table 3).

Precursor gases	SiH_4 (silane) , NH_3 (ammoniac)
Flow rates	700 sccm , 18 sccm
Process temperature	300 °C
Process base pressure	1 torr
RF power	10 W
Deposited material	SiN_4
Deposition rate	20 nm/min

Table 3: Used process parameters for a PECVD process.

3.2 Lithography techniques

For the high resolution fabrication of point contacts with radii between 130 and 40 nm electron beam lithography is employed, while for the μm patterning of the structures optical lithography is utilized. In the following the conducted fabrication procedures are summarized for both techniques.

3.2.1 Optical lithography

A Suess Micro Tec MJB4 mask aligner is employed to transfer geometrical patterns via ultraviolet (uv)-light lithography into a photo sensitive resist, which is further used as etch mask (Fig. 21). This way lateral feature sizes of 1 micrometer are easily fabricated [1, *Hilleringmann;99*].
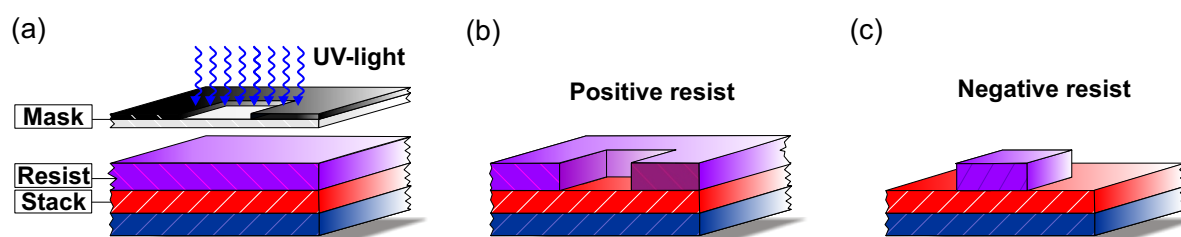
Figure 21: (a) Optical photo lithography with photo sensitive resist. (b) For a positive resist the exposed patterns become soluble in a developing solvent. (c) The opposite effect is achieved with a negative resist, where the exposed areas engrave as mask pattern in the resist after the development (adapted from [1, *Hilleringmann;99*]).

The first fabrication step is the contamination free preparation of the sample surface. In most cases it is sufficient to clean the sample in an ultra-sonicated acetone bath and subsequently in an isopropanol bath for 5 minutes each. Additional 5 minutes on a 120 °C hotplate ensures the complete evaporation of the cleaning solvents. The cleaned sample is then, depending on the desired film properties, spin coated in several consecutive steps with photosensitive resists, e.g. with an adhesion promoter and subsequently with positive photo resist (compare table 4).

Typical spin coating parameters are 4000 rpm for 20 seconds, causing a several 100 nm thick resist layer. A soft bake at 110 °C for 60 seconds drives out the soluble parts of the resist and increases its structural stability. In the following, the mask needs to be aligned to the sample surface. Micrometer drives allow the relative positioning of sample and mask in the view field of the mask aligner microscope. In the next step the resist is exposed to uv-light for typically 10 seconds to achieve the desired morphological reaction. The resist is developed by dipping the sample into a developing solution for about 30 seconds, removing undesired parts of the mask pattern. Finally, the process results are evaluated via optical microscopy. The utilized process parameters are listed in table 4.

Positive resist			Negative resist		
- Adhesion resist	HDMS*		- Adhesion resist	HDMS*	
- Spin coating	4000 rpm, 20 sec		- Spin coating	3000 rpm, 35 sec	
- Positive resist	AZ MIR701*		- Hotplate	170 °C, 5 min	
- Spin coating	4000 rpm, 30 sec		- Negative resist	Az5214*	
- Soft bake	110 °C, 60 sec		- Spin coating	8000 rpm, 35 sec	
			- Hotplate	120° C , 60 sec	
Exposure			Exposure		
- Time	10 sec		- Time	5 sec	
			- Post exposure bake	120 °C , 60 sec	
			- Flood exposure	7 sec	
Developer	MIF 726*, 30 sec		Developer	MIF 726*, 30 sec	

Table 4: *List of used uv-lithography procedure steps. *The commercially available resists and solutions can be found in Ref. [5].*

3.2.2 Electron beam lithography

Very small feature sizes below 100 nm are fabricated with the electron beam of a Zeiss Supra 40 electron microscope together with a Raith ELPHY Quantum writing unit. The typical fabrication process is done as follows. In a first step the sample surface is cleaned to remove any soluble contamination. In the next step an electron sensitive resist like PMMA[3] is spin coated on top of the wafer stack at typically 4000 rpm for about 30 seconds, forming an approximately 500 nm thick resist layer. A subsequently baking step at 170 °C causes the polymer molecules to form chains and therefore increases its structural stability. The e-beam writing procedure starts with the sample loading to the high vacuum chamber of the SEM device. After a working pressure of about 10^{-6} mbar is reached, the electron beam needs to be focused and aligned to the sample surface. The positioning procedure is carried out by computer controlled, micrometer step drives. Then a predesigned pattern writing procedure is executed, exposing the resist with a predefined beam dose in the targeted regions. The final step is the development of the structures by dipping the sample for about 90 seconds into a developer to remove the soluble parts of the resist. The development is stopped in an additional neutralizing bath. The used process parameters are summarized in table 5.

---

[3]polymethylmethacrylat

E-beam resist	PMMA 950K AR-P679.04*
Spin coating parameter	4000 rpm, 30 sec
Hotplate	170 °C, 30 min
E-beam gun voltage	10 kV
Beam current	240 pA
Aperture	30 μm
Dot dose	0,5 fAs
Developing procedure	e-beam developer AR600-56*, 90 sec
	e-beam stopper AR 600-60*, 90 sec

Table 5: *Used process parameters for electron beam lithography. *The commercially available resist and the solutions can be found in Ref. [5].*

3.3 Etching techniques

Two different etching techniques are employed in the nano-fabrication process[4] of this work to physically and chemically remove material parts from the deposited stack, which have been patterned in the lithography process steps. Chemical reactive ion etching (RIE) is utilized to open holes into an insulating SiN_4 layer and physical ion beam etching (IBE) together with secondary ion mass spectroscopy is employed to access the bottom contact of the devices.

3.3.1 Reactive ion etching

For the fabrication of nanocontacts the samples are etched with pure SF_6 in an Oxford Instruments Plasmalab 100 ICP-RIE machine, operated under cleanroom conditions (Tab. 6).

Process gas	SF_6
Flow rate	25 sccm
Process pressure	15 mtorr
HF-power	25 W
Temperature	40°C
Etching rate	80 nm/min

Table 6: Process parameters of the reactive ion etching procedure used in this work.

---

[4]section 3.5

3.3.2 Ion beam etching

The bottom contacts of the deposited multilayers are opened by an Ion Sys 500 ion beam milling system, which is adapted to a HidenAnalytical HAL 301 secondary ion mass spectrometer, custom designed by Roth&Raud. In this machine accelerated Ar ions knock out (sputter) atoms from the multilayer surface. With the mass spectroscopy device, which is diverging and detecting the eject ionic gas compounds, it is possible to stop the etching process when a targeted layer of the multilayer has been reached. The etching rate and profile is tuned by adjusting the acceleration grid voltages, as well as by the rotation and tilt of the sample holder. The utilized process parameters are listed in table 7.

Process gas	Ar
Process pressure	$1 \cdot 10^{-7}$ mbar
Power	330 W
Focusing grid voltage	500 V
Angle of incidence	$60°$
Rotation speed	3 rpm
Typical etching rate	10-50 nm/min

Table 7: Used process parameters for the ion beam etching procedure.

3.4 Characterization techniques

The fabricated nano structures are characterized by means of atomic force and scanning electron microscopy, the fundamental principles of which are presented in the following sections.

3.4.1 Atomic force microscope

The atomic force microscope (AFM) measurements are carried out in this thesis with an instrument from "Molecular Imaging (Pico Plus)". In the measurements a several nanometer sharp tip (PPP-NCHR-50 from "Nanosensors"'), the so called cantilever tip, scans a targeted region of the sample surface (Fig. 22(a)). Depending on the distance between tip and surface a Van der Waals force (Fig. 22(b)) acts on the cantilever and causes a characteristic bending. The latter is detected by an optical system, where a laser beam reflection from the cantilever is measured with a split photodiode detector, which compares the vertical as well as the horizontal deflection output.

The measurements are performed in the tapping mode of the instrument, while the scanning software "AFM PicoView 1.6" is utilized. The tapping mode is characterized by an externally generated oscillation of the cantilever near its resonant frequency. During each oscillation swing of 20-100 nm amplitude, the tip "taps" on the sample surface. The interaction forces between
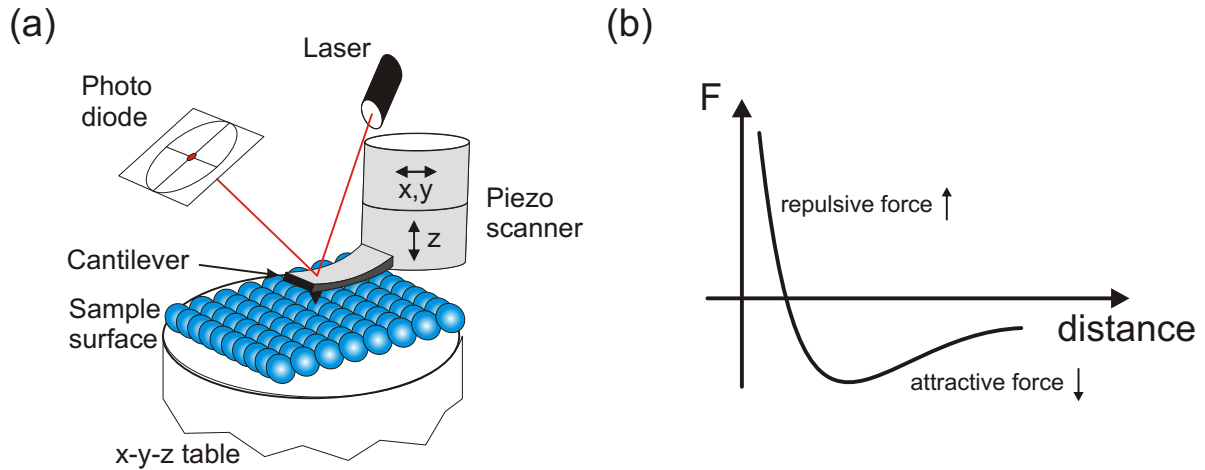
Figure 22: (a) Basic components of an atomic force microscope with feedback loop. (b) Surface potential versus distance between tip and surface.

tip and surface are detected as amplitude and phase changes of this resonant frequency setpoint. The amplitude changes are used as feedback signal to maintain a constant distance between tip and surface. The therefore needed tip height correction is then used as the topography defining variable in a computer controlled imaging process.

3.4.2 Scanning electron microscope

Besides the AFM measurements the fabricated structures are mainly characterized in a Zeiss Supra 40 scanning electron microscope (SEM), in which a highly focused electron beam is manipulated by an electromagnetic lens system. The beam is rastered over the sample surface, causing a deflected radiation, which can be monitored by a set of detectors.

In the SEM system an electron source (e-gun) generates electrons in a high vacuum chamber which become accelerated towards a ring shaped anode. The voltage at the e-gun cathode can be tuned from 5 kV up to several tens of kV, adjusting the kinetic energy of the electrons. The electrons trajectories are influenced by a set of magnetic and electrostatic fields, focusing a beam on a desired sample spot. In contrast to optical lenses the focal length of these electromagnetical lenses is adjustable.

The sample is mounted on a computer controlled, three dimensional x-y-z positioning table, which also allows rotation and tilting of the sample. Several detectors can be chosen for the imaging process to detection either secondary electrons, backscattered electrons or transmitted electrons. The detected signal amplitude in dependence on the e-beam spot position is visualized as gray intensity in a two dimensional image, which gets refreshed at an adjustable frame rate. This way it is possible to achieve magnifications of up to 6 orders of magnitude from about 10 to 500000 times (Fig. 24(a)).

3.5 Nanofabrication

The samples investigated in this thesis contain nano-contacts fabricated on top of the sputter-deposited spin-valve multilayers (Fig. 23(a)-(i)). A Si wafer with 50 nm thermal oxide was used as substrate. Several types of spin-valves were fabricated, containing different free layer materials and thicknesses as well as differently pinned polarizers (see chapter 4.1). The point contacts were defined by e-beam lithography (Fig. 23(b)) and subsequently etched with reactive ion etching into a 70 nm thick SiN_4 insulating layer (Fig. 23(c)), which is deposited by PECVD on top of the spin-valve. Circular contacts with a radius ranging from 40 to 130 nm ($\pm$10 nm)
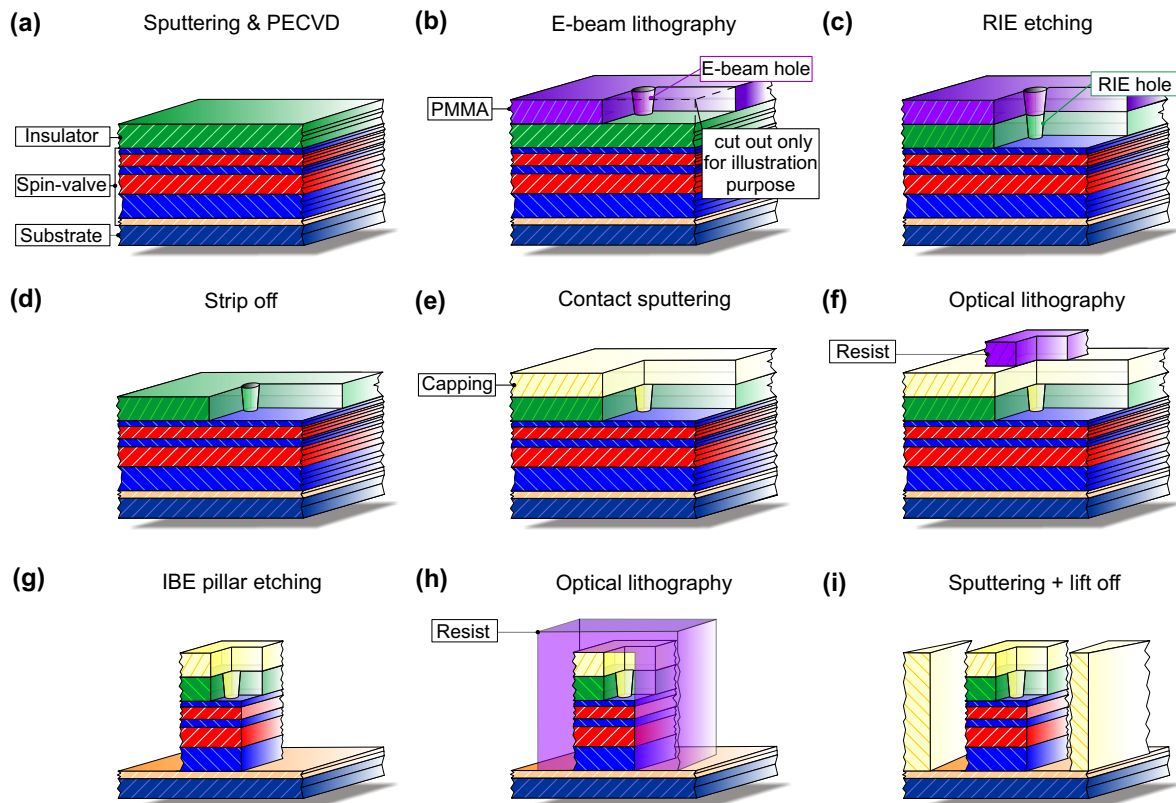
Figure 23: Fabrication process steps for spin-valve nanocontact and contact pillars.

were defined. The radius values have been extracted from SEM and AFM images (Fig. 24). In the following, Ta(10)/Au(200) top electrodes were sputter deposited (Fig. 23(e)), where the Ta serves as adhesion layer. Contacts to the bottom Ru layer were opened with uv-lithography (Fig. 23(f)) and ion beam etching, defining spin-valve mesas of 100×100 μm in lateral size (Fig. 23(g)). Finally, Ta(10)/Au(250) pads were build via uv-lithography (Fig. 23(h)) and sputter-deposition (Fig. 23(f)) to access the bottom contact for electrical measurements.
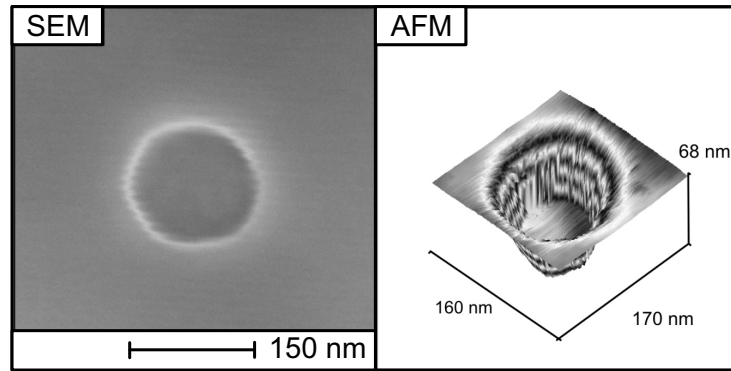
Figure 24: Scanning electron and atomic force microscopy images of a typical nanocontact with a diameter of 150 nm.

3.6 Experimental measurement setup

A single device is connected from the top with a custom designed radio frequency (RF), ground-source-ground tip[5], fronted by special non-magnetic Cu/Be contact springs with a pitch of 200 μm (Fig. 25(b)). Figure 26(a) shows the developed measurement setup. The device is placed on an aluminum chuck in the center of a coil arrangement, composed of a stator coil ring and a
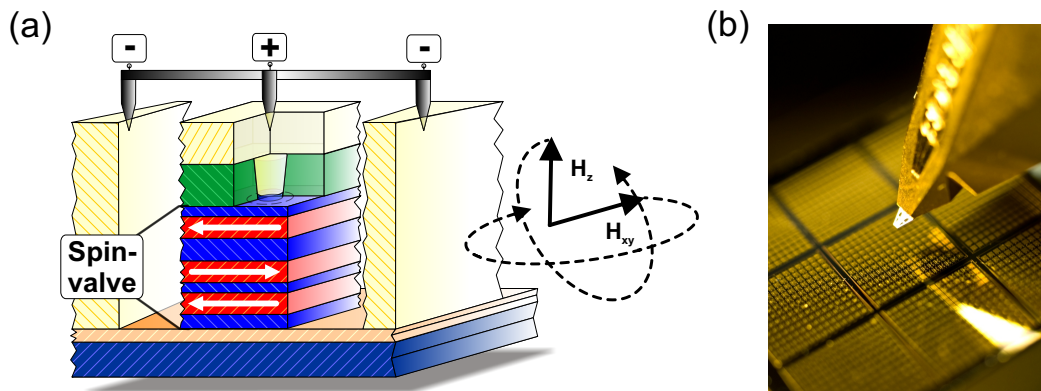
Figure 25: (a) Device connected via RF-probe. Magnetic in- and out-of-plane fields can be applied in arbitrary direction. (b) Photograph of the RF-tip fronted by nonmagnetic contact springs.

Helmholtz coil pair. The RF-tip and 4 single tips for 4-point measurement purpose, are attached to custom designed arms[6], which are mounted to 5 independently adjustable x-y-z micrometer drives. An optical microscope allows a direct view on top of the sample surface (Fig. 26(a),(b)).

---

[5]Süss Z rf-probe with custom design
[6]further details on the setup design and construction are given in appendix 3.6
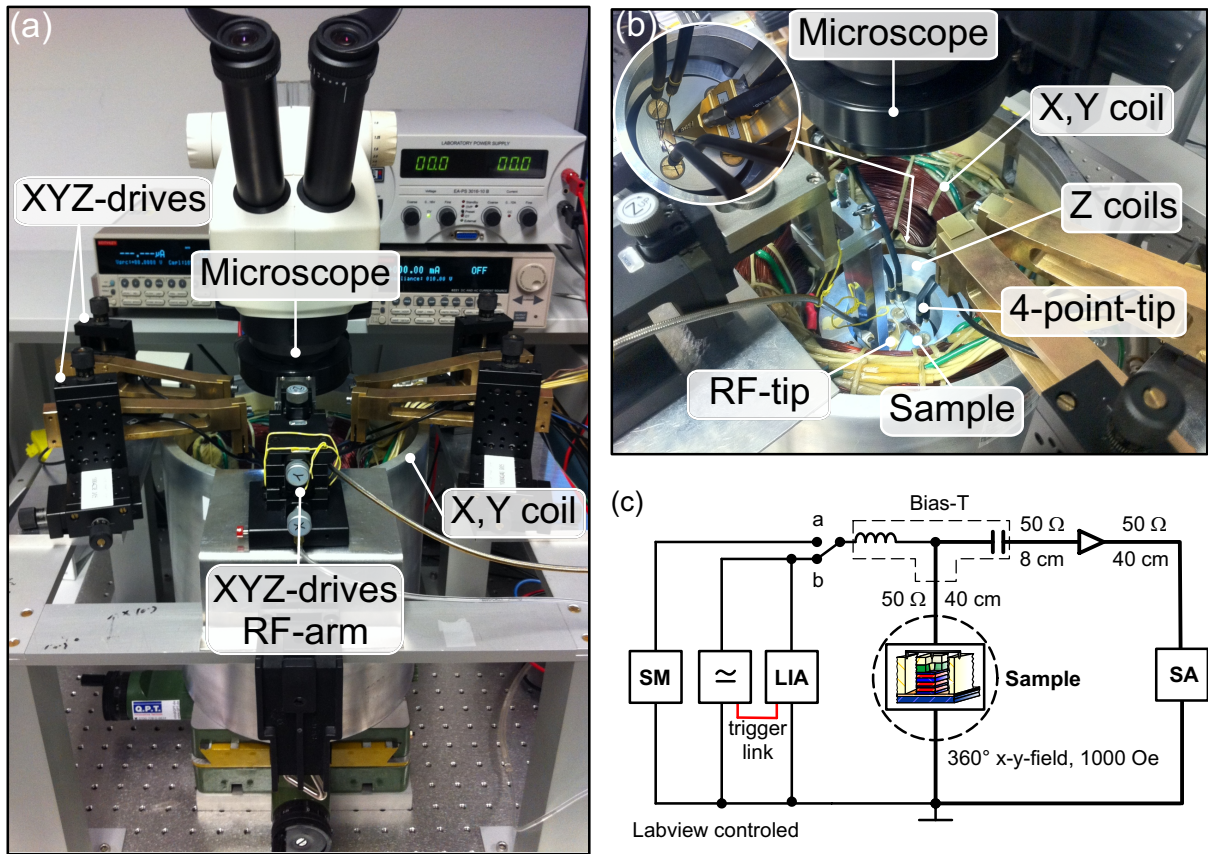
Figure 26: (a),(b) Photographs of the measurement setup. (c) Measurement circuit with source meter (SM) in switch position "a" and ac/dc source/lock-in amplifier (LIA) in position "b", bias-T, 50 Ω rf-cable, and spectrum analyzer (SA).

The electrical circuit, included a sourcemeter[7], ac/dc current source[8], lockin amplifier[9] and spectrum analyzer[10], which input is preamplified by 27 dB. A bias-T allowed, depending on the switch position (a or b in Fig. 26(c)), the measurement of current-voltage (I-V) or differential resistance-current (dV/dI-I) together with the power spectral density-frequency (PSD-f) characteristics. The ac/dc current source is trigger linked to the lock-in amplifier allowing the dV/dI measurement[11]. Two programmable power supplies[12] are used to drive currents of up to 8 A to the coil arrangements, generating 360° rotatable in-plane magnetic fields, of up to 1000 Oe and out-of-plane fields H_z, of up to 500 Oe. Negative dc polarity corresponds to the electron flow direction from the top of the device central pillar to the bottom contact.

---

[7]Keithley 2400 source-meter
[8]Keithley 6221 dc and ac current source
[9]Singnal recovery 7265 DSP lock-in amplifier
[10]Tektronix 494 AP programmable spectrum analyzer
[11]measurement scheme is illustrated in appendix 9.1
[12]Kepco Power Supply BOP 50-20 MG
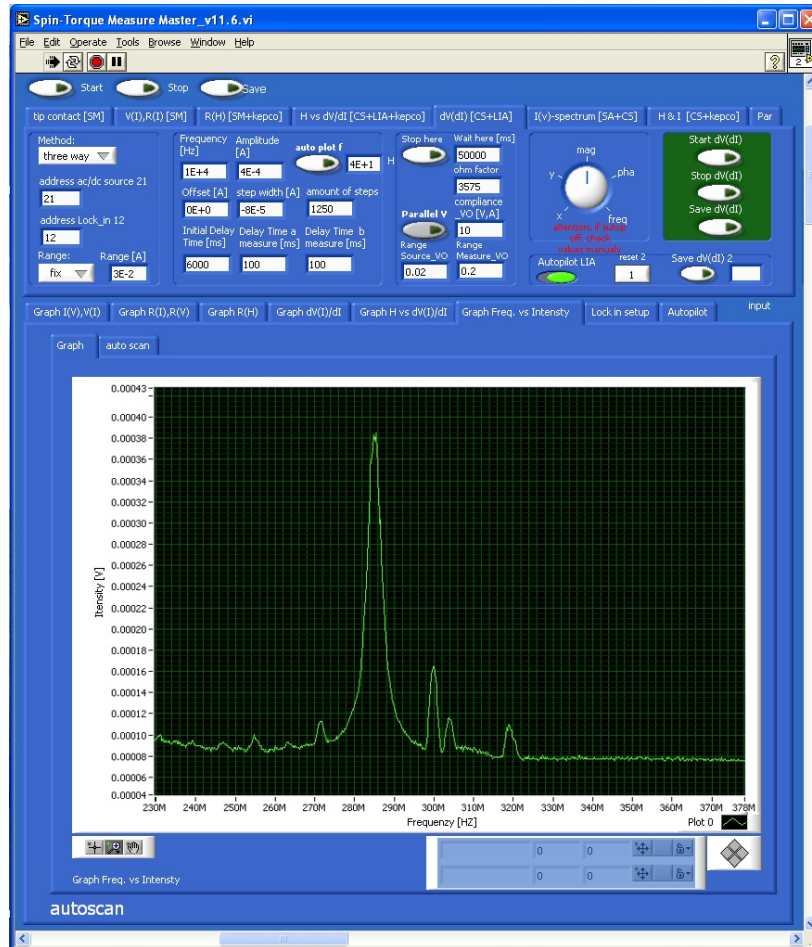
Figure 27: Custom designed Labview program for all source and measurement units.

Source Current		Measurement	
- Direct current (dc)	-60 to +60 ±0,001 mA	- Resistance	5-50 ±0,002-0,01 Ω
- Alternating current (ac)	50-250 ±0,1 μA	- dV/dI*	5-50 ±0,002 Ω
- Frequency (trigger)	10 kHz ±1 Hz, sinus	- Frequency	0,05-18 GHz >±1 kHz
Magnetic field		- PSD**	0,1-500 ±0,05 nV^2/Hz
- In-plane	1-1000 ±1 Oe		
- Angle (in-plane)	1-360 ±1 °		
- Out-of-plane	1-500 ±1 Oe		

Table 8: Used parameter room (*differential resistance, **power spectral density).

The described source and measurement units are connected via GPIB-bus to a computer[13] unit and are controlled by a software program custom designed in the Labview code[14] (Fig. 27). The latter enables the measurement of the key variables for the parameter room shown in table 8. Additionally, a fully automized measurement option was designed, allowing customized subprograms to subsequently schedule desired measurement tasks in the parameter room.

References

[1] U. Hilleringmann. *Silizium-Halbleitertechnologie*. Teubner Studienbuecher. Teubner, 1999.

[2] G. Anderson G. Wehner. *Handbook of Thin Film Technology, chapter The Nature of Physical Sputtering*. McGraw Hill, 1983.

[3] L. Maissel. *Handbook of Thin Film Technology, chapter Application of Sputtering to the Depostion of Films*. McGraw Hill, 1983.

[4] S.M. Sze and K.K. Ng. *Physics of semiconductor devices*. Wiley-Interscience publication. Wiley-Interscience, 2007.

[5] http://www.microresist.de.

---

[13]Windows XP Microsoft Corporation 1985-2001 operated
[14]Labview 8.1 National Instruments 2003

4 HF excitations and switching in spin-valve nanocontacts

4.1 Mulilayer stack design and magnetotransport properties

In the following, the multilayer design and the magnetotransport properties of spin-valve nanocontacts are presented and the measurement background of the electric signals are discussed.

4.1.1 Spin-valve nanocontacts with natural and artificial antiferromagnet

Two main types of spin-valve stacks were investigated in this thesis. In the first type, the polarizer consists of a polycrystalline $Co_{70}Fe_{30}(3.5)$ layer[15] that is exchange biased by a $Ir_{17}Mn_{83}(15)$ AF layer, while in the second type, the polarizer consists of a $Co_{70}Fe_{30}(2.2)/Ru(0.76)/Co_{70}Fe_{30}(3)$
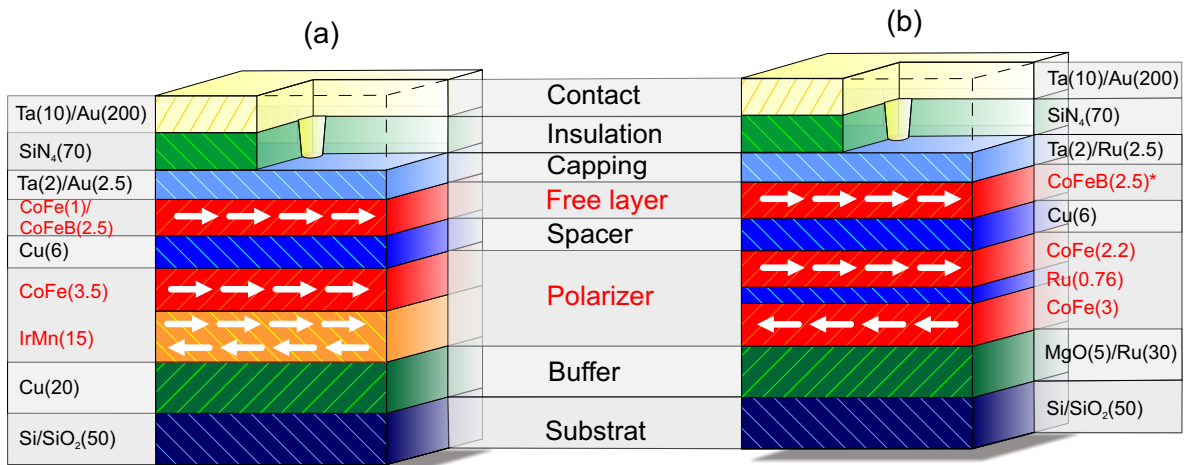
Figure 28: Sketch of the multilayer stack with $Ir_{17}Mn_{83}(15)$ exchange biased polarizer and $Co_{70}Fe_{30}(1)/Co_{40}Fe_{40}B_{20}(2.5)$ free layer (a) and sketch of the stack with an artificial antiferromagnet and a $Co_{40}Fe_{40}B_{20}(2.5)$ (* or $Co_{70}Fe_{30}(1)/Co_{40}Fe_{40}B_{20}(2.5)$) free layer (b).

AAF trilayer. For the free layer, either an amorphous $Co_{40}Fe_{40}B_{20}(2.5)$ layer or a polycrystalline $Co_{70}Fe_{30}(1)/Co_{40}Fe_{40}B_{20}(2.5)$ composite layer is employed. The corresponding multilayer structures, as shown in figure 28, comprise four building blocks: buffer, spin-valve, capping and nanocontact, the purpose of each is discussed in the following.

The buffer is deposited on a Si wafer substrate with 50 nm thermal oxide and is optimized for low series resistance and to provide a smooth basis for the subsequent growth of the magnetic spin-valve. In particular the buffer defines the roughness and texture of the subsequently deposited layers, which influence the rigidity of the magnetic components, for example in terms

---

[15]The subscripts stand for material compositions in atomic percent and the layer thickness denoted in parentheses, in nm.

of anistopies or orange peel coupling (chapter 2.3). The buffer serves after the patterning procedure as bottom contact for the current perpendicular-to-plane flow through the spin-valve. The magnetic properties of the spin-valve are optimized, so that, in the first case (Fig. 28(a)) a large exchange bias of the bottom hard electrode is realized, and, additionally, a minimum magnetic coupling between polarizer and free layer is achieved. In the other case (Fig. 28(b)) where the polarizer is formed by the asymmetric AAF, the Ru spacer layer thickness is tuned for a large exchange AF coupling of the two unequally thick ferromagnetic layers.

The purpose of the capping is to prevent the free layer from oxidation and to serve as low resistive interface for the subsequent connection to the nanocontact. The final block is the insulating layer, incorporating the nanocontact covered by a metalization layer for the rf-tip
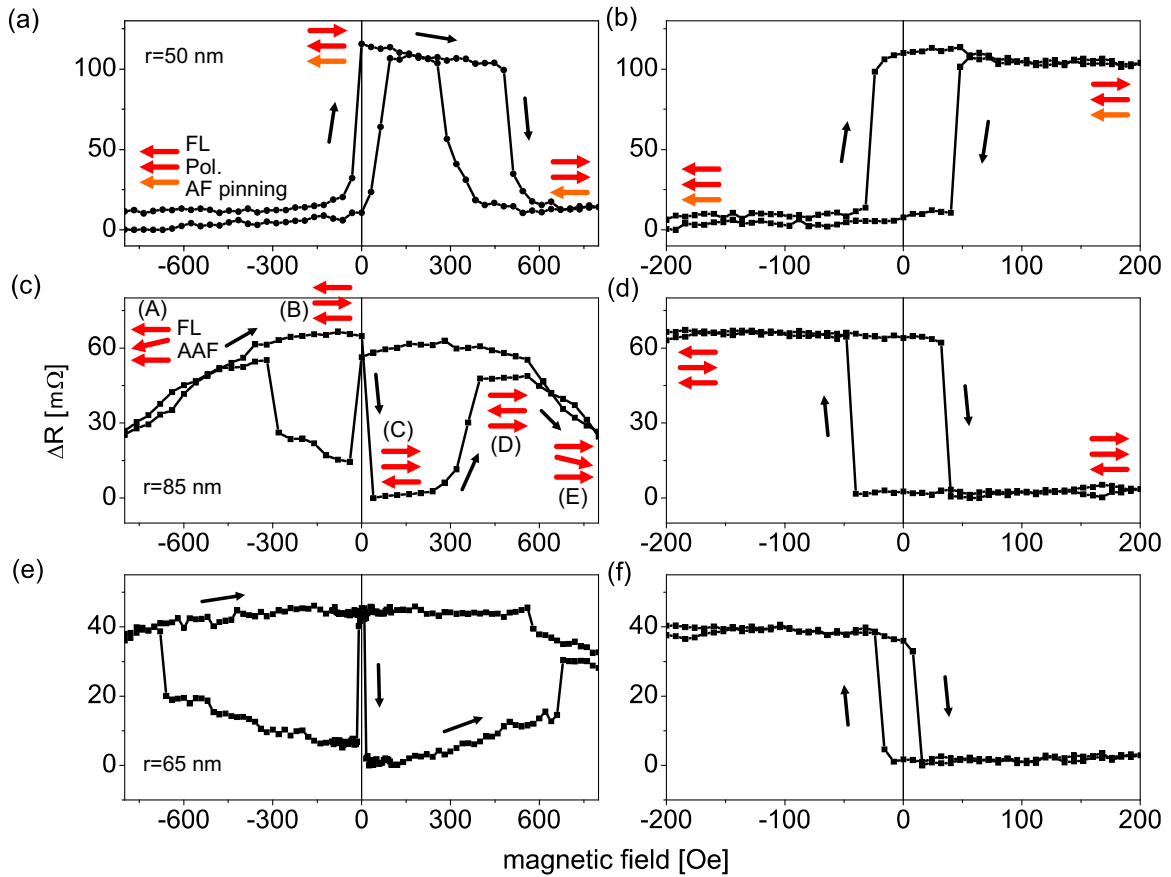
Figure 29: (a) Measured magnetic major loop for the exchange biased stack ($r = 50\ nm$) and (b) the corresponding minor loop. (c) Major loop for the stack with AAF and CoFe/CoFeB free layer ($r = 85\ nm$), as well as the corresponding minor loop (d). (e) Major loop for the AAF stack with *CoFeB* free layer ($r = 65\ nm$) and corresponding minor loop (f). The difference of the AAF plateau is a result of the different contact sizes.

contact pads (see also Fig. 25), which was optimized for large thermal stability and strong adhesion to the capping layer.

The devices investigated in this thesis have nanocontact radii, r, ranging from 40 to 130 nm. These values have been extracted from scanning electron microscopy and atomic force microscopy images, like the one presented in Fig. 24. The total device resistance, R_t ranges for both stack types from typically 10 Ω to 30 Ω and is given by the sum of the electrode resistance, R_{el}, and the nanocontact resistance, R_{nc}. The typical average electrode resistance is $R_{el} \approx 9$ Ω.

Characteristic easy-axis magnetization switching loops of the device types presented in figure 28 are measured for cpp nanocontacts at low current ($I \cong 1$ mA). Their magneto resistance Δr in dependence on the magnetic field is depicted in figure 29. The corresponding minor loops show a clear switching between parallel and antiparallel states for all devices and realized radii, where the Δr values range between 40 and 110 $m\Omega$. The magnetic major loop of the exchange biased[16] stack shows the typical GMR double layer switching of the soft magnetic free layer and hard magnetic polarizer presented in chapter 2.1. The switching field is approximately 40 Oe and a small ferromagnetic-type bias is observed due to the orange-peel coupling between the free layer and polarizer.

For the multilayer type incorporating the asymmetric AAF and a FM free layer the curve of the major loop presents the switching expected for the three layer system, which can be understood in a model that considers the rotation of each layer magnetization as single domain state (step (A) to (E) in Fig. 29(c)). First, starting for all three layers from an almost saturated state in negative field direction (A), the top AAF layer rotates to an antiparallel state (B), due to the AAF coupling (see chapter 2.3). For small positive fields the free layer switches parallel to the top AAF layer (C), abruptly decreasing the stacks GMR. For larger positive fields the net magnetic moment of the AAF gradually rotates parallel to the applied field direction (D) and finally all three layer approach saturation in positive field direction (E). The switching occurs in the opposite sequence for the reversed field sweep.

The switching field of the $CoFeB$ stack is with a value of 15 Oe, about 2 to 3 times smaller than the one of the $CoFe/CoFeB$ free layer. Clear parallel and antiparallel resistive states are obtained as the switching field of the AAF's net magnetic moment exceeds largely the one of the free layer.

4.1.2 Joule heating and Seebeck currents in spin-valve nanocontacts

All electric transport measurements for nanocontacts at room temperature are accompanied by heating effects, caused by the spatially confined electron current flow, which is leading to large current densities of up to 10^{12} A/m^2. Figure 30(a) shows a sketch of the device. In the applied measurement design, negative current polarity defines an electron current flow from the top to the bottom contact. In Figure 30(b) two dV/dI measurement at zero magnetic field are

---

[16]The sample was annealed at a temperature of 300 °C in a magnetic field of 250 Oe for 15 minutes.
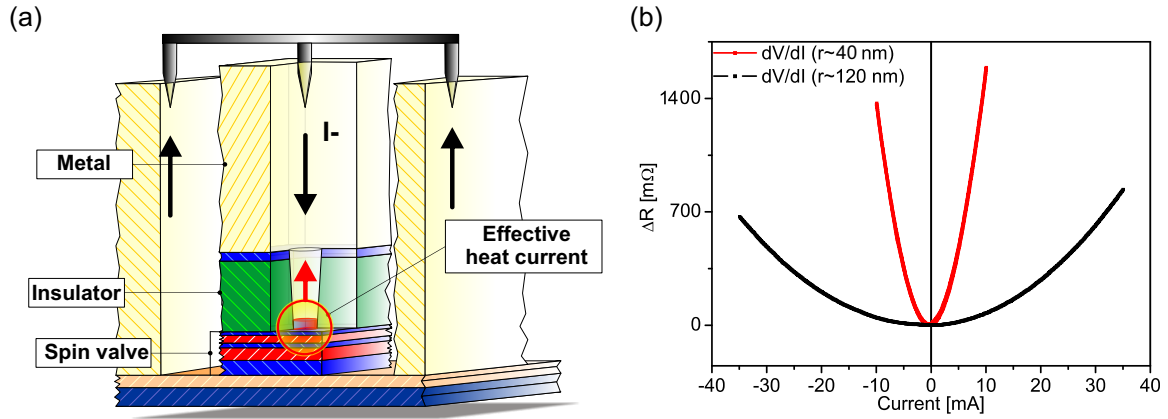
Figure 30: (a) The current flow through the nanocontact causes an effective heat current. (b) Typical $dV/dI - I$ curves measured for nanocontacts with radii of $40\ nm$ and $120\ nm$.

presented for nanocontacts with a radius of $40\ nm$ and $120\ nm$. They show a quadratic increase of the resistance for increasing currents, which is attributed to Joule heating, for which the rate of heat dissipation in a resistive conductor is found to be proportional to the square of the current through it and to its resistance [1, $^{Magie;11}$]. The Joule heating contribution increases antiproportionally to the square of the nanocontact radius and depends on the stack material.

The asymmetric resistance increase observed for the two current polarities can be accurately fitted under the assumption of a constant current shift, I_{eff}, in the parabolic Joule heating equation in the form of:

$$R = a(I - I_{eff})^2 + c\,, \tag{4.22}$$

where a and c are constant fitting parameters. We attribute this asymmetry to an effective Seebeck current, which is commonly generated in conducting materials exposed to a temperature gradient due to the thermal diffusion of the conducting electrons [2, $^{Uchida;Nat;08}$]. The different materials in the vicinity of the nanocontact have largely different thermal conductivities, which lead to a significant heat current, if, large current densities are applied through the nanocontact.

4.1.3 Degradation effects in spin-valve nanocontacts

The measured devices typically sustain current densities of 4 to $9 \times 10^{12}\ A/m^2$ before abrupt degeneration features appear in the $dV/dI - I$ curve. After a certain application time of a critical current density, the elements change its parabolic dV/dI behavior similar to the one presented in figure 31(a). We attribute this behavior to a degenerated nanocontact. After the degeneration has taken palace the resistance increases several Ω. This suggests that the metallic connection is declined, possibly due to the detachment of the nanocontact or due to interdiffusion effects of materials close to the contact channel. In figure 31(b) an intermediate case between this effect and the joule heating characteristic is depicted. In addition to this two contributions, a small

hysteretic resistance change is present in the current loop (see sweep through the points A,B,C,A in figure 31(b)), which we attribute to changes in the magnetization profile of the spin-valve.

A typical $dV/dI - I$ measurement of a properly working and not degraded nanocontact is presented in figure 32, clearly showing a hysteretic type of resistance change for negative current polarity. The ΔR of this hysteric contribution is in the order of the one presented in Fig. 29(f) and approximately one order of magnitude smaller than the joule heating effect. These current-induced magnetic switching effects are similar to STT measurements reported in the literature [3, *Devolder;APL;09*], [4, *Kiselev;Nat;03*] and are the subject of investigation in the following sections.
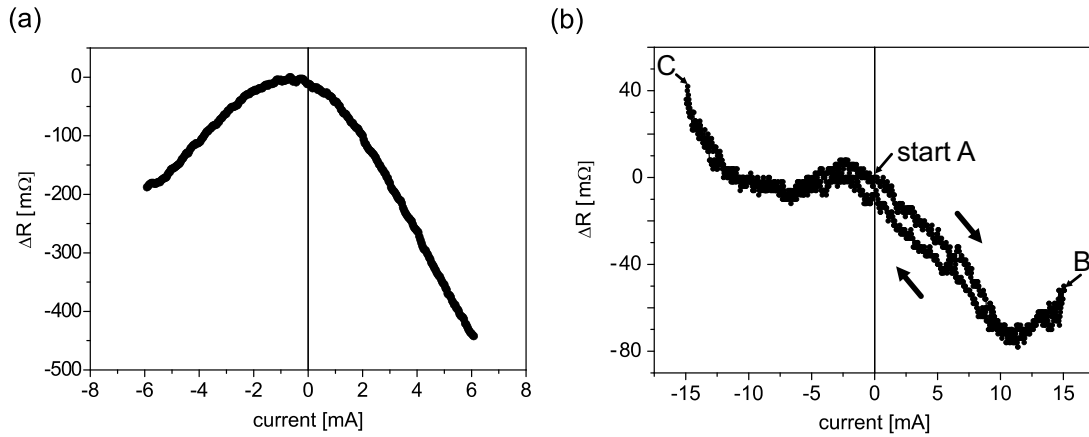
Figure 31: (a) Curve for an "shot" element. (b) Superposition of "shot" curve, joule heating and switching. The current is subsequently swept through the points A, B, C, A.
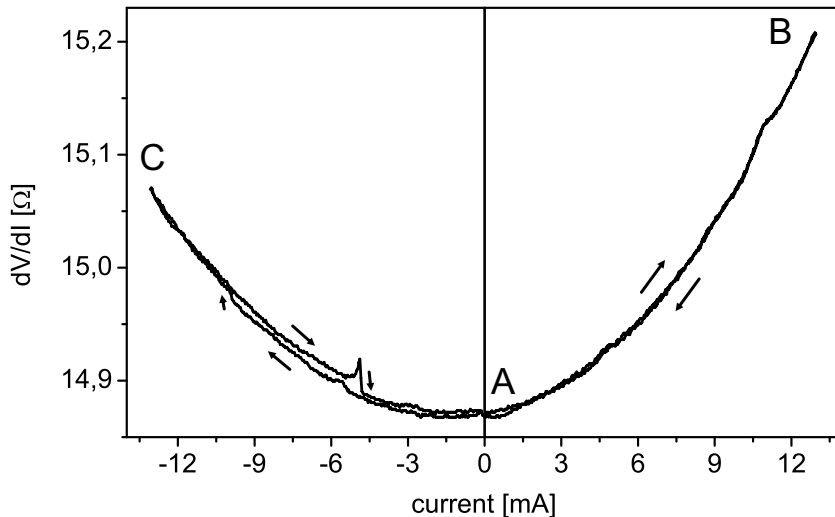
Figure 32: Typical $dV/dI - I$ measurement shows hysteretic switching features for both current polarities. The current is swept subsequently through the points A, B, C, A.

4.1.4 Conclusion of section 4.1

Two basic types of multilayer structures are investigated in this work: one incorporating a spin-valve with exchange biased polarizer and one with an artificial antiferromagnet. Additionally, different types of free layers materials and thicknesses are investigated and the electronic and magnetic performance of the multilayers building blocks (buffer, spin-valve, capping and nanocontact) is optimized. Nanocontacts with radii ranging between 40 and 130 nm direct the current flow of up to 45 mA perpendicular through the structure. The multilayer resistance in dependence on the external magnetic field shows clear switching of the spin-valve free layer for switching fields of 15 Oe for $CoFeB(2.5)$ and of 40 Oe for $CoFe(1)/CoFeB(2.5)$. The current perpendicular to plane magnetoresistance varies between 40 and 110 $m\Omega$. All transport measurements are accompanied by Joule heating effects and Seebek currents, leading to an asymmetric parabolic curve in the $dV/dI - I$ measurements. Below a critical current density of about 4 to $9 \times 10^{12} \ A/m^2$ the resistance response to the current can be swept in a reversible manner.

4.2 Current induced vortex oscillations and switching

In the following the relation between the measured current induced $dV/dI - I$ features and the for the first time reported observation of sub-GHz excitations in GMR spin-valve nanocontacts, employing an AAF as polarizer and CoFeB(2.5) as free layer, are presented. Subsequently, the dependence of these excitations on the nanocontact radius and on the free layer moment is investigated. At the end of this section these results are compared to a macrospin model as well as to numerical micro-magnetic simulations of the system, which incorporate the Oersted field and spin-transfer torque contributions.

4.2.1 Oscillation characteristics and dV/dI features

A typical dV/dI measurement for a spin-valve[17] incorporating an AAF and CoFeB(2.5) as free layer with a nanocontact radius of 90 nm is shown in figure 33(b). The measurement is recorded at zero magnetic field ($H = 0$) after applying a reset field of -800 Oe in easy-axis direction. This reset field is always applied before a new measurement is performed. At the specific state ($H = 0$), the free layers moment is not completely antiparallel to the thin AAF layer, as suggested by the reduced remanence in the minor loop of figure 33(a). From the raw dV/dI data (Fig.
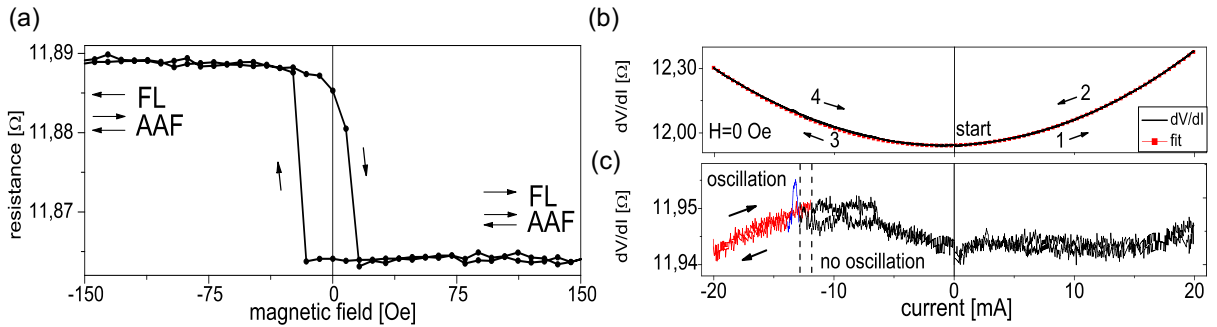
Figure 33: (a) Easy-axis switching loop at low current ($I \approx 1$ mA). (b) dV/dI-I loop measured at H=0 Oe. (c) dV/dI-I loop after subtraction of the parabolic background. The dashed lines mark where HF dynamics are observed.

33(b)), an asymmetric parabolic curvature was subtracted to account for the Joule heating of the contact, resulting in the curve presented in figure 33(c). This curve shows features, which can be attributed to the combination of spin-transfer torque between the AAF and the free layer and the influence of the Oersted field. For negative current polarity, the same sequence of dV/dI features is systematically observed independent of the contact size. The resistance jump for increasing current at the value of $I_{cr} = -13$ mA (Fig. 33(c)) marks the onset of excitation dynamics like they are presented in figure 34, after which the dV/dI starts to decrease to a lower resistive state for increasing $|I|$. The corresponding magnetoresistance (MR) changes are always

---

[17]the stack sequence is presented in chapter 4.1.1

a fraction of the total MR value, which shows that these features represent transitions between nonuniformly magnetized states. The dV/dI curves show no systematic features for positive current polarity. The spectra present a quasi-linear correlation between frequency and current. This is in qualitative agreement with model for vortex excitation in nanocontacts, like it is presented in equation 2.20 [5, [Kim;CM;10]] and for nanopillars in equation 2.18 [6, [Dussaux;NatC;10]] in chapter 2.5. This result is as well in qualitative agreement with the numerical simulations
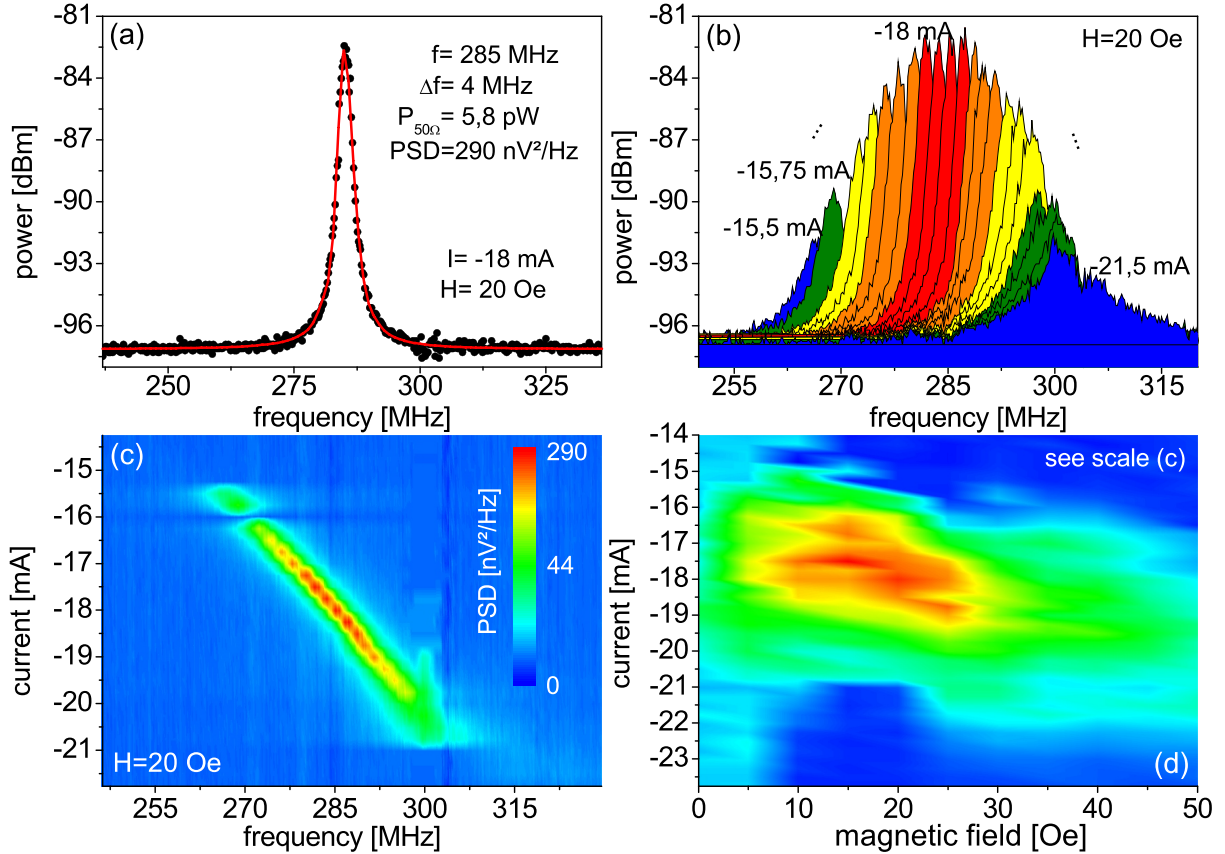
Figure 34: (a) Excitation spectrum measured at minus 18 mA and 20 Oe easy-axis field, fitted with a Lorentzian curve. (b) Power (at 50 Ω and resolution band width $RBW = 1MHz$) for increasing excitation currents. (c) PSD map versus frequency and current for $H = 20\ Oe$. (d) Maximum emitted PSD vs easy-axis magnetic field and current.

of Khvalkovskiy for nano-sized pillars [7, [Khvalkovskiy;APL;10]], where the frequency depends on the free layer magnetization, its thickness, and the contact size. The rate of frequency increase is 6.8 MHz/mA in the present case. For currents, $|I| > |I_{cr}|$ the power increases, reaches its maximum, and then gradually decreases until the oscillation completely breaks down for $|I| > 20$ mA (Fig. 34(b)). The maximum values of the individual power spectra in figure 34(b) form a Gaussian envelop. The breakdown of the excitation for large currents is attributed to spatially incoherent oscillations of the magnetization in the ferromagnetic mesa due to the extensively

large spin-torque.

High frequency (HF) response of the nanocontacts is measured only for negative current, in accordance to other experimental findings [3, $^{Devolder;APL;09}$],[8, $^{Devolder;APL;10}$],[9, $^{Otxoa;PSB;11}$] and theoretical predictions [5, $^{Kim;CM;10}$],[10, $^{Khvalkovskiy;APL;09}$]. Like it is presented in chapter 2.5, for the vortex precession in spin-valve nanocontacts the model of Kim et al. predicts physical solutions only for one current polarity, which corresponds to the case where the electrons flow outward from the nanocontact. The CIP part of this current flow below the nanocontact is expected to counterbalances the Gilbert damping and therefore prevents the vortex spiraling into the contact center.

The obtained sub-GHz spectra, as the one shown in figure 34, are consistent with the excitation of nonuniform vortex-like states created by the Oersted field, H_{Oe} and spin-transfer torque associated with the current flow through the nanocontact, as it is theoretically introduced in chapter 2.5 and investigated in the micro-magnetic simulations in section 4.2.5. The simulations show that at $H = 0$ a highly nonuniform magnetic state is developed in the free layer underneath the nanocontact even for low currents ($I = 2\ mA$), gradually transforming into a vortex-like state for increasing currents ($I = 15\ mA$). The AAF presents significantly larger rigidity against the Oersted field, although it gradually adopts a nonuniform magnetization profile for large currents. It has been demonstrated that, in the absence of a perpendicular field, such a nonuniformity in the polarizing layers magnetization, in this case the AAF, is crucial for the excitation of vortex dynamics [10, $^{Khvalkovskiy;APL;09}$]. In comparison to the measurements presented in figure 33(b) the excitation onset is at $-13\ mA$ ($H_{app} = 0$), which corresponds to a critical current density (j_{cr}) of $5 \times 10^{11}\ A/m^2$ and is marked by the blue peak in the $dV/dI - I$ curve in figure 33. Based on the simulation results we assume that at the corresponding critical current ($I_{cr} = -13\ mA$) two requirements are fulfilled: (a) the AAFs magnetization has acquired the necessary nonuniformity and (b) the spin current is high enough to initiate vortex dynamic excitation.

The dynamic excitation can be further restored in a practically reversible manner by decreasing $|I|$ until it finally collapses at nearly the same current value it was initiated. We note here that in [11, $^{Rippard;PRL;04}$], [12, $^{Pufall;PRB;07}$], [13, $^{Mistral;PRL;08}$], [14, $^{Ruotolo;NatN;09}$], [3, $^{Devolder;APL;09}$] and [9, $^{Otxoa;PSB;11}$] the presence of excitation is hysteretic with the current, i.e. the vortex has to be nucleated at a high current and then it persists for decreasing current much below the nucleation threshold. In our case, the nucleation current is particularly low and almost coincides with the current where the excitation collapses (Fig. 35). As a result, an excitation spectrum is determined by the current amplitude and is practically independent of whether the current is increasing or decreasing, in accordance with the predictions of Ref. [15, $^{Berkov;PRB;09}$]. Further, the excitation is located within a current window, where the $dV/dI(I)$ curve is not hysteretic. This almost hysteresis free oscillation profile can be important in terms of applications, since the whole frequency regime is directly accessible with the current. This means that in the other devices for the establishment of frequencies below the nucleation frequency first the nucleation current needs to be applied, which is then reduced to access lower frequencies.
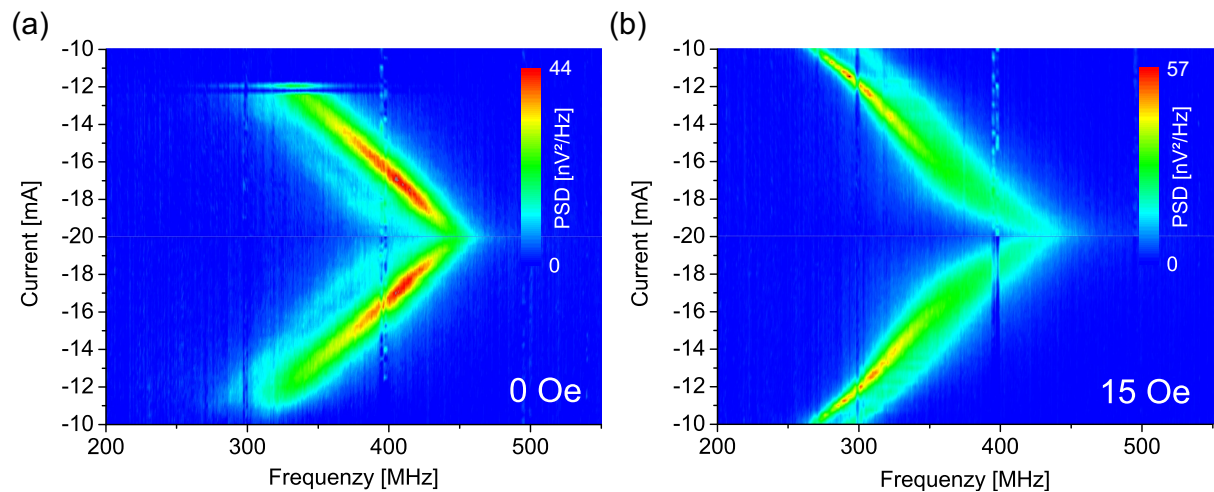
Figure 35: Power spectrum map versus frequency and current for magnetic fields of 0 Oe (a) and 15 Oe (b). The current is ramped up from -10 to -20 mA and back to -10 mA to demonstrate the almost hysteresis free oscillation profile.

At the point where the excitation breaks down for decreasing $|I|$ we do not observe any feature at the dV/dI curve that would suggest an abrupt change in the magnetic state of the system. We can therefore assume that the reason for the break down is the reduced spin-torque transfer due to the current decrease. The annihilation of the static nonuniform magnetic state is strongly suggested by the dV/dI drop at about -6.5 mA (Fig. 33(c)). When the current is reduced to zero the initial magnetic state below the nanocontact seems to be restored. If the current is increased again, the oscillation takes place again.

Furthermore, the obtained critical current density (j_{cr}) for the onset of oscillation at zero magnetic field is 6 to 17 times smaller than the values reported in the literature [12, [Pufall;PRB;07]],[3, [Devolder;APL;09]],[16, [Kuepferling;PRB;10]] for nanocontacts with $CoFe$ or $NiFe$ free layers. Such a reduction implies a larger spin torque transfer, which can be associated with a higher current spin polarization. An enhancement of the spin polarization might arise from the presence of Ru layers above and below the free layer, as it has been reported in the literature [17, [Jiang;PRL;04]]. In this report the presence of a Ru cap layer of 0.45 nm on top of an exchange biased spin-valve pillar with a thin CoFe(2.5) free layer is shown to effectively decrease the critical current density to induce the switching of its free layer. The authors argue that Ru impurity in Co is shown to scatter majority spins more strongly and leads to large spin imbalance and spin scattering at a Co/Ru interface. They assume that the Ru cap serves as a strong majority spin scatterer in their system. We believe that a similar effect is present in our multilayer, which causes a larger spin torque transfer.

4.2.2 Oscillation dependence on the nanocontact size

The focus of our analysis is now on the oscillation dependence on the nanocontact radius. Figure 36 presents characteristic power spectra for nanocontact radii between 40 nm and 100 nm, at zero applied field. The oscillation spectra show the evolution of current, frequency and power
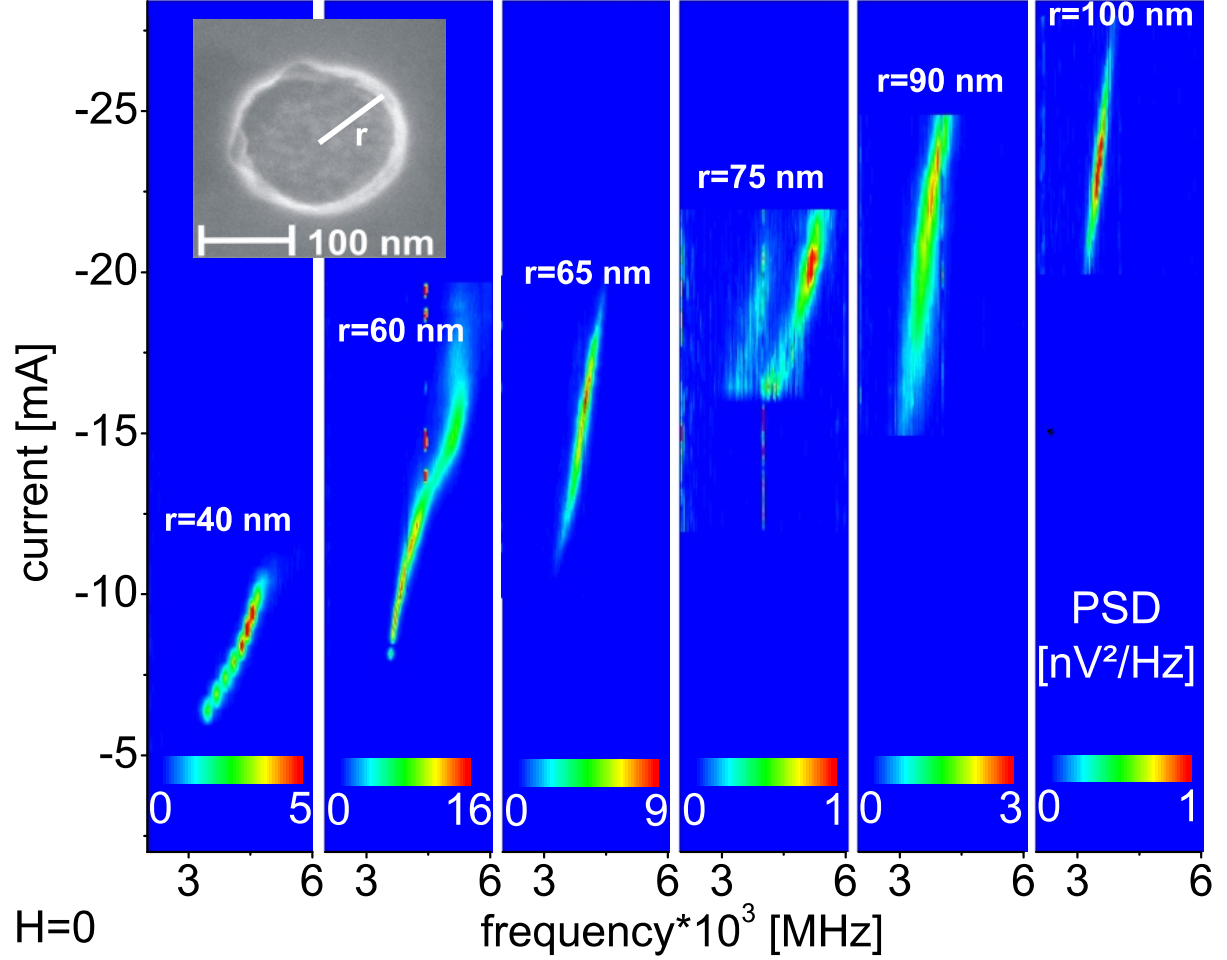
Figure 36: PSD plots versus current and frequency for 40 nm, 60 nm, 65 nm, 75 nm, 90 nm and 100 nm contact radius at zero magnetic field (a) to (f). The inset shows an SEM image of a $r = 75$ nm contact.

spectra density for increasing nanocontact radius. For some nanocontacts two spectral peaks can be clearly distinguished that are not harmonically correlated (Fig. 36 $r = 75$ nm). This particularity of our system, found for easy- and hard-axis, in-plane fields is discussed in detail in chapter 4.3.3.

Only for nanocontacts smaller than $r < 100$ nm excitation could be observed in the spectra. This result is in agreement with Ref. [18, [Ralph;JMMM;08]] where, for nanocontact radii above 100 nm, the Oersted field contribution is expected to be the dominant force component, prohibiting

any spin-transfer torque driven oscillation. A detail investigation of the influence of the Oersted field on the spin-valve is presented in the simulations of section 4.2.5.

Figure 37 summarizes the main results at zero applied field. In figure 36(a) the excitation onset current, I_0, is found to scale linearly with r^2, i.e. the dynamics are initiated at a constant current density of $j_0 = 6.5 \times 10^{11} \ A/m^2$, as extracted from the linear fit of I_0 versus r^2.
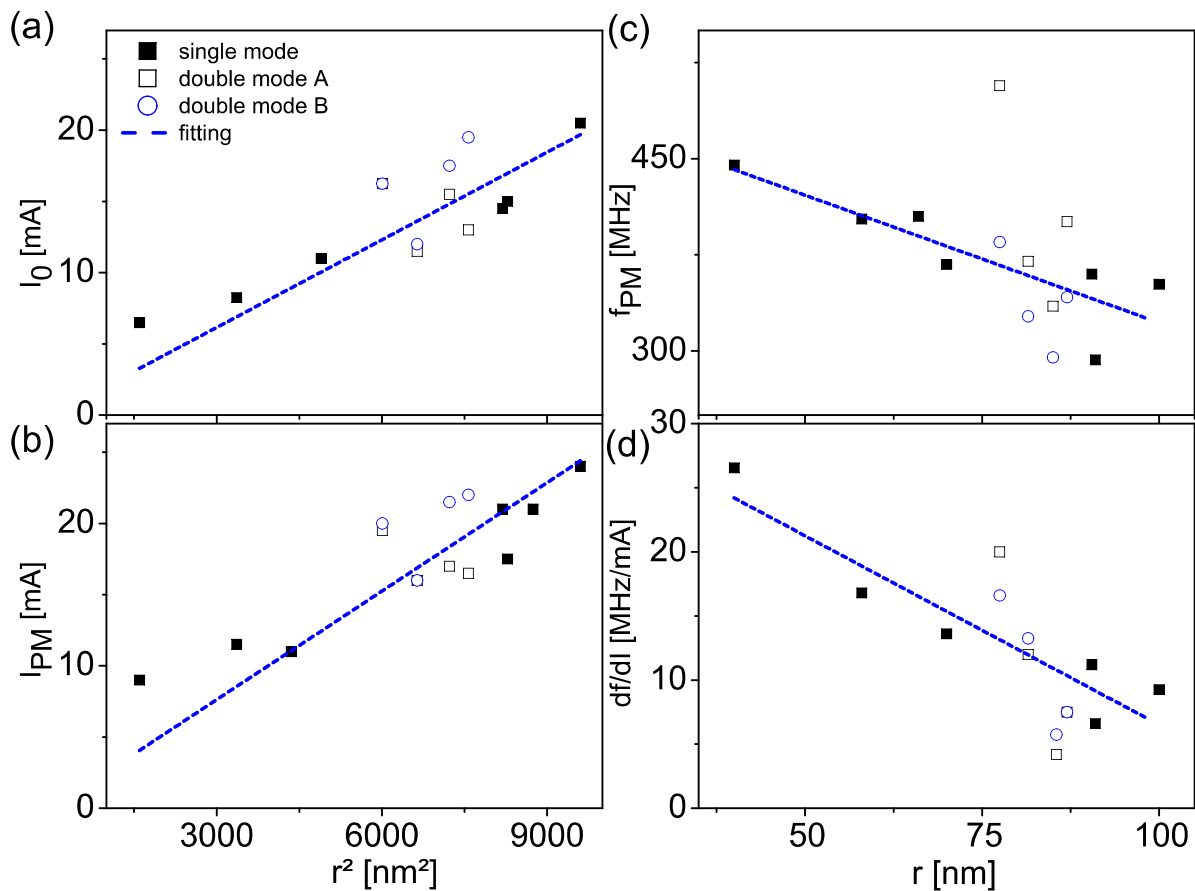
Figure 37: (a) Excitation onset current, (b) current at maximum power, (c) frequency at maximum power and (d) inclination df/dI versus point contact radius.

Open symbols in the graphs correspond to excitation modes appearing in pair, as the one in figure 37(d). Not only I_0 but also the current corresponding to the maximum excitation power, I_{PM}, shows a quasi-linear dependence on r^2 (Fig. 37(b)), i.e. to achieve maximum power, a defined current density is required, in this case $j_{PM} = 8 \times 10^{11} \ A/m^2$, irrespective of the nanocontact size. On the other hand, the maximum power is not emanated at the same frequency, f_{PM}, for all nanocontacts. Indeed, f_{PM} decreases with the nanocontact radius, as shown in figure 37(c). Also the slope, df/dI, decreases with r (Fig. 37(d)). This measurement result disagrees with the theoretical model of Ref. [19, $^{Kim;PRL;08}$], which is presented in chapter 2.5, where df/dI is predicted to be independent of the nanocontact radius and should be a material-dependent

parameter (compare equation 2.20). The authors argue that their model represents a simple model with no adjustable parameters and that it is not precise on a quantitative level in regard with experimental findings. Like we will see in section 4.3.2, the basic assumption of a rigid vortex core precession is a rough approximation for our systems with relatively large nanocontact radii, which fits best to the model for large excitation currents. The degree of uniformity of the vortex-"like" magnetization plays an important role for the dynamics and is not included in the model of Kim. Further, their assumption of a uniform radial current flow in the film plane is rarely valid for real devices and is certainly influenced by the current flow defining geometries, like for example the nanocontact radius.

4.2.3 The influence of the free layer magnetic moment

As it is shown in section 4.2.1 the oscillations are initiated at certain current density values, marked by abrupt changes in the dV/dI-I measurements. In the following, these spin-transfer torque induced magnetization changes are the subject of investigation for different free layer materials as well as for stacks incorporating an AAF and for exchange biased stacks. Further, the influence of the free layer moment on the existence of oscillations is discussed.

We begin the investigation with the spin-valves[18] incorporating an AAF as polarizer and either a $CoFeB(2.5)$ or $CoFe(1)/CoFeB(2.5)$ free layer. Figure 38(a) shows the minor loops for both systems, which only differ by 1 nm of $CoFe$ in the free layer. In figure 38(b) and (c) two typical dV/dI versus I curves are presented for the devices with nanocontact radii of 85 nm and 65 nm. Negative current corresponds to electrons flowing from the free towards the
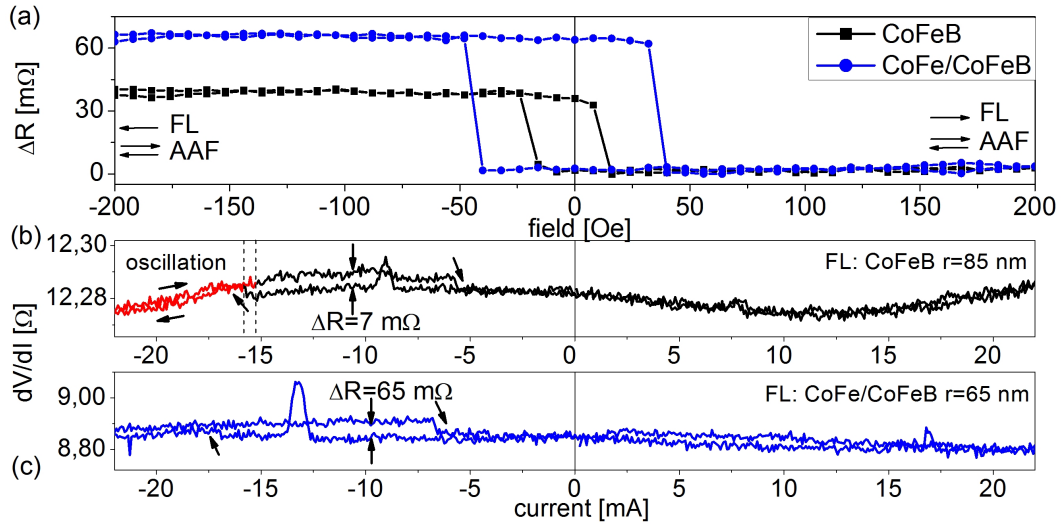
Figure 38: dV/dII loops after subtraction of the parabolic background for both FL. Dashed lines mark the beginning and end of the excitation.

---

[18]the detailed stack sequence of which is given in chapter 4.1

fixed magnetic layer. The typical parabolic Joule heating contribution (compare Fig. 32) has been subtracted from the raw data. Both measurements show, for negative current polarity, a similar sequence of resistance features, but of different amplitude. The first feature in the sequence is a jump in the resistance for increasing current at $-16\ mA$ in Fig. 38(b), after which the dV/dI starts to decrease and which also marks the onset of dynamics, then, a drop to a lower resistive state for decreasing currents. The dynamic resistance change is $\Delta_{dyn} = 7$ $m\Omega$ for the $CoFeB(2.5)$ nanocontact, i.e. only 20 % of the total GMR. On the other hand, the resistance change for the $CoFe(1)/CoFeB(2.5)$ nanocontact corresponds to the full GMR amplitude, possibly caused by the stronger spin-torque generated in this stack. This means that the current induces an inhomogeneous magnetization state in the $CoFeB(2.5)$ nanocontact, whereas the magnetization of the $CoFe(1)/CoFeB(2.5)$ free layer under the nanocontact has switched completely to a uniform state.

Excitation spectra in the sub-GHz regime, as the ones shown in figure 34 and attributed to vortex dynamics could only be measured for the $CoFeB(2.5)$ stack and only for negative current polarity, where the free layer magnetization is excited by spin-polarized electrons reflected from the fixed magnetic layer. For the $CoFe(1)/CoFeB(2.5)$ nanocontacts (40 to 130 nm radius), where a complete magnetization switching is assumed to have taken place, no excitation could be observed for frequencies between $0.1\ GHz$ and $18\ GHz$, for $|I|$ up to $45\ mA$ and applied fields up to the free layer switching field. The interplay between the generated spin-transfer torque and the Oersted field induced magnetization profile (chapter 2.5) in the more rigid $CoFe(1)/CoFeB(2.5)$ free layer is not supporting oscillations in this parameter regime. This shows that prerequirements for magnetic excitations are the establishment of a non-uniform magnetic state in the free layer, together with a matching spin-transfer torque contribution, which is fulfilled only in the case of the $CoFeB(2.5)$ nanocontact with the AAF polarizer and for contact radii below 100 nm. In accordance with this conclusion, no oscillations could be measured for stacks[19] incorporating an exchange biased polarizer and a high magnetic moment $CoFe(1)/\ CoFe(2.5)$ free layer. This kind of stacks show dV/dI switching features, which can be approximated by a current induced macrospin switching model, as it is presented in the next section.

---

[19]The stack sequence is shown in chapter 4.1.1

4.2.4 Macrospin model for current induced switching effects

In accordance with the conclusion of chapter 4.2.3, no oscillations could be measured for the stack[20] incorporating an exchange biased polarizer and a high magnetic moment $CoFe(1)/$ $CoFe(2.5)$ free layer. Here, we show that the dV/dI switching features for this and a similar system with even higher magnetic moment free layer can be explained by a current induced switching model.

Figure 39 shows the magnetic switching loops for a nanocontact with a radius of 50 nm and a multilayer of the following structure (nm): $Cu(25)/Mn_{83}Ir_{17}(15)/Co_{70}Fe_{30}(5)/Cu(7)/$ $Co_{70}Fe_{30}(2)/Ni_{80}Fe_{20}(5)/Ta(2)/Au(3)$. The magneto resistance in the current perpendicular-to-plane geometry is measured approximately 25 $m\Omega$. The switching of the free layer magneti-
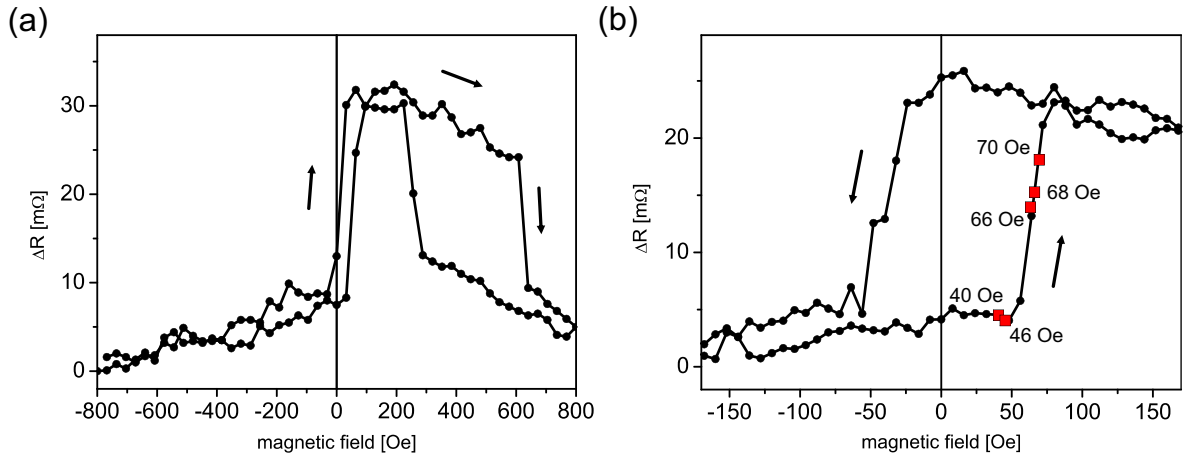
Figure 39: (a) Major loop of an exchange biased stack with $Co_{70}Fe_{30}(2)/Ni_{80}Fe_{20}(5)$ free layer and (b) corresponding minor loop.

zation takes place between 50 and 75 Oe as it can be deduced from the magnetic minor loop in figure 39(b). Starting from specific switching states in this field window (indicated in the figure by red squares) current sweeps of positive and negative polarity are performed. The corresponding dV/dI versus current measurements in figure 40(a) show pronounced, hysteretic peaks and dips[21], the relative amplitude and position of which are changing as a function of the specifically applied in plane magnetic fields. These changes are appearing for both current polarities can be explained with a model that takes into account the spin-transfer torque and the Oersted field generated by the current flow through the nanocontact, as well as the interlayer exchange and magnetostatic coupling interacting in the detection layer.

---

[20]The stack sequence is shown in chapter 4.1.1

[21]These peaks and dips in the resistance are caused by the *ac* modulation of the dV/dI measurement and correspond to rounded steps in the corresponding *dc* measurement [20, [Katine;PRL;00]],[21, [Tsoi;PRL;00]], while the effective resistance change above and below the feature is regardless of the measurement mode the same.
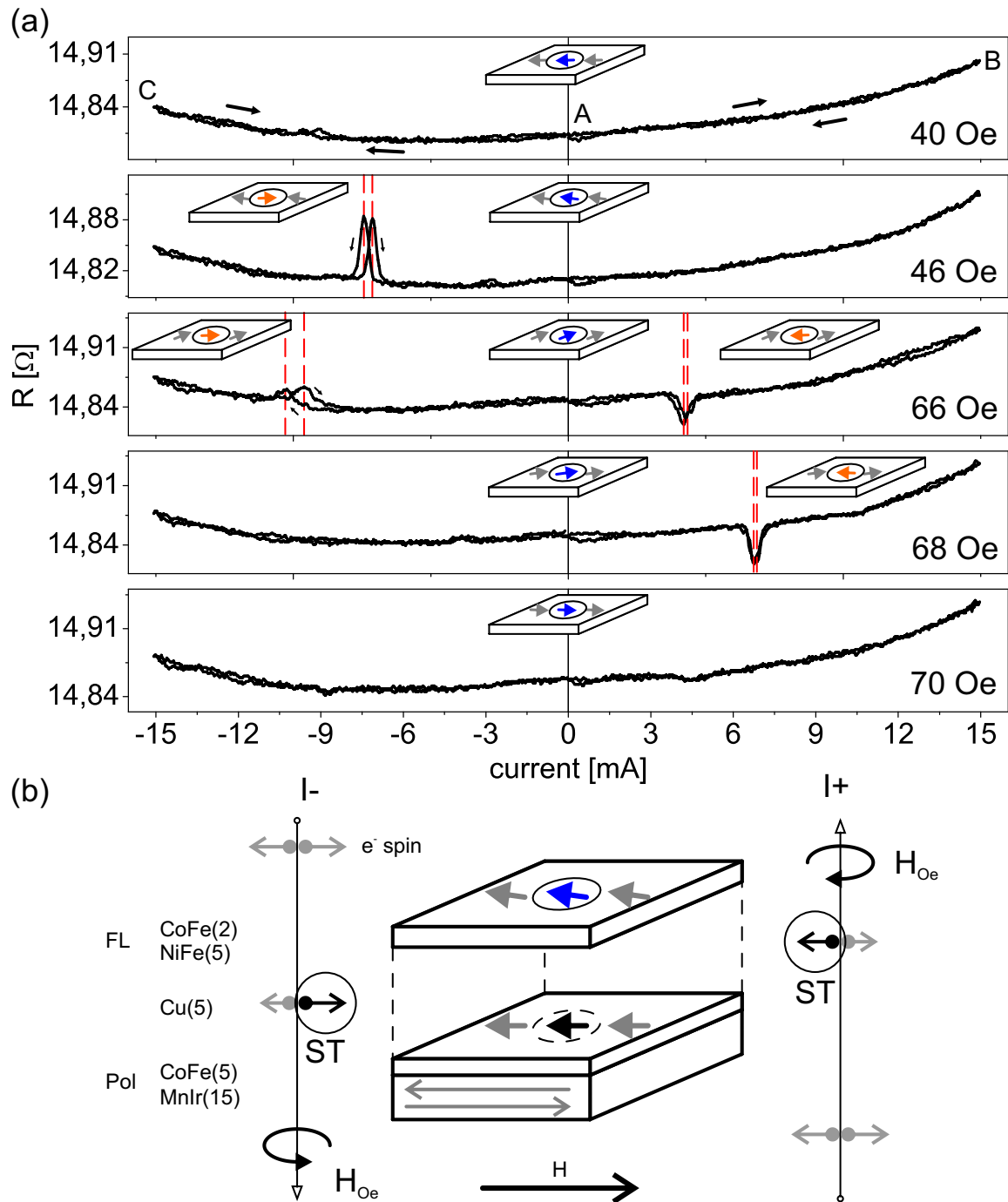
Figure 40: (a) dV/dI versus current measurements at different easy-axis fields ($r \cong 50$ nm). The current is swept subsequently to the following extrema values: $0, 15, -15, 0$ mA. The small arrows indicate the domain orientations of the free layer. (b) Model for the influence of magnetic field, spin-torque and magnetization of the FL and polarizer.

Figure 40(b) shows a simple model of the magnetic spin-valve components. The free layer (FL) and exchange biased polarizer (Pol) magnetization in reach of the current flow are assumed to consist of single domain states (encircled central blue and black arrows in Fig. 40(b)). In a real sample these domains are surrounded by the rest of the total layer magnetization, which is in the model - for the sake of simplicity - assumed to be given by two domains to the sides of the central one (gray arrows in the layers in Fig. 40(b)). The large arrows to the sides of the layers indicate the electron current flow direction together with its two degrees of freedom for the electron spin and the direction of the Oersted field, H_{Oe}. For negative current polarity a from the polarizer back scattered spin current reenters the free layer (compare chapter 2.4.1).

For a critical field and current value the combination of current generated Oersted field and spin current is large enough to manipulate the free layer domain in reach of the current flow and reorients the domain against its surrounding free layer magnetization (compare blue and orange arrows in Fig. 40(a) for 46 Oe).
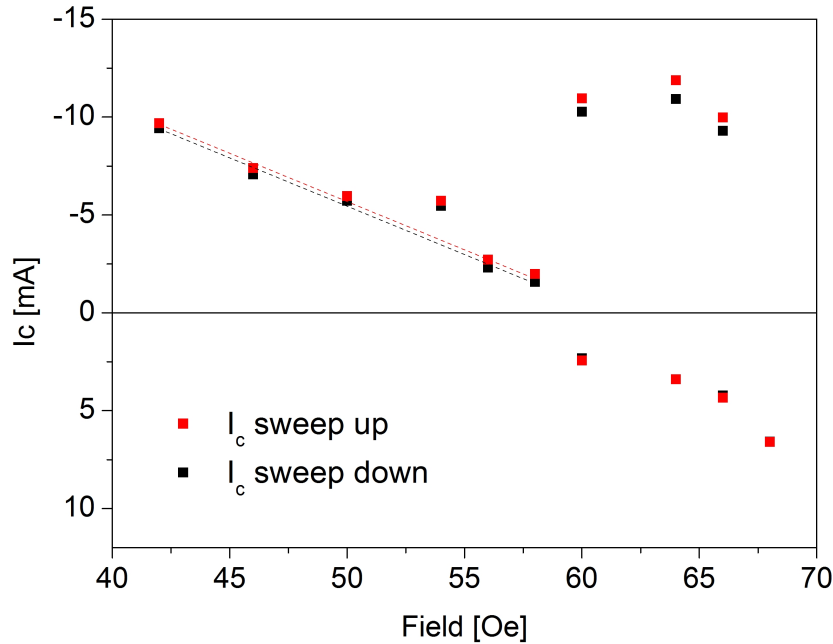
Figure 41: Critical switching current in dependence on the magnetic field.

The reorientation changes the resistance of the GMR stack (peak or dip) depending either a more parallel or antiparallel alignment of free layer and polarizer is realized. The domain switches back into its energetically favored parallel alignment with the surrounding magnetization, when the current is decreased again below the critical switching current value. The features in figure 40(a) show a clear transition from positive to negative resistance changes for increasing magnetic field values. Only in the vicinity of the switching field the effect is strong enough to induce a detectable GMR change, as it can be deduced from figure 41 (42 to 68 Oe), depicting the critical current switching values in dependence on the in-plane field.

The same transition of features in the vicinity of the coercive field is reproduced for several elements of the same structure, as well as for large nanocontacts ($r > 100\ nm$) incorporating the AAF polarizer and the $CoFe(1)/CoFeB(2.5)$ free layer, as shown in figure 42.
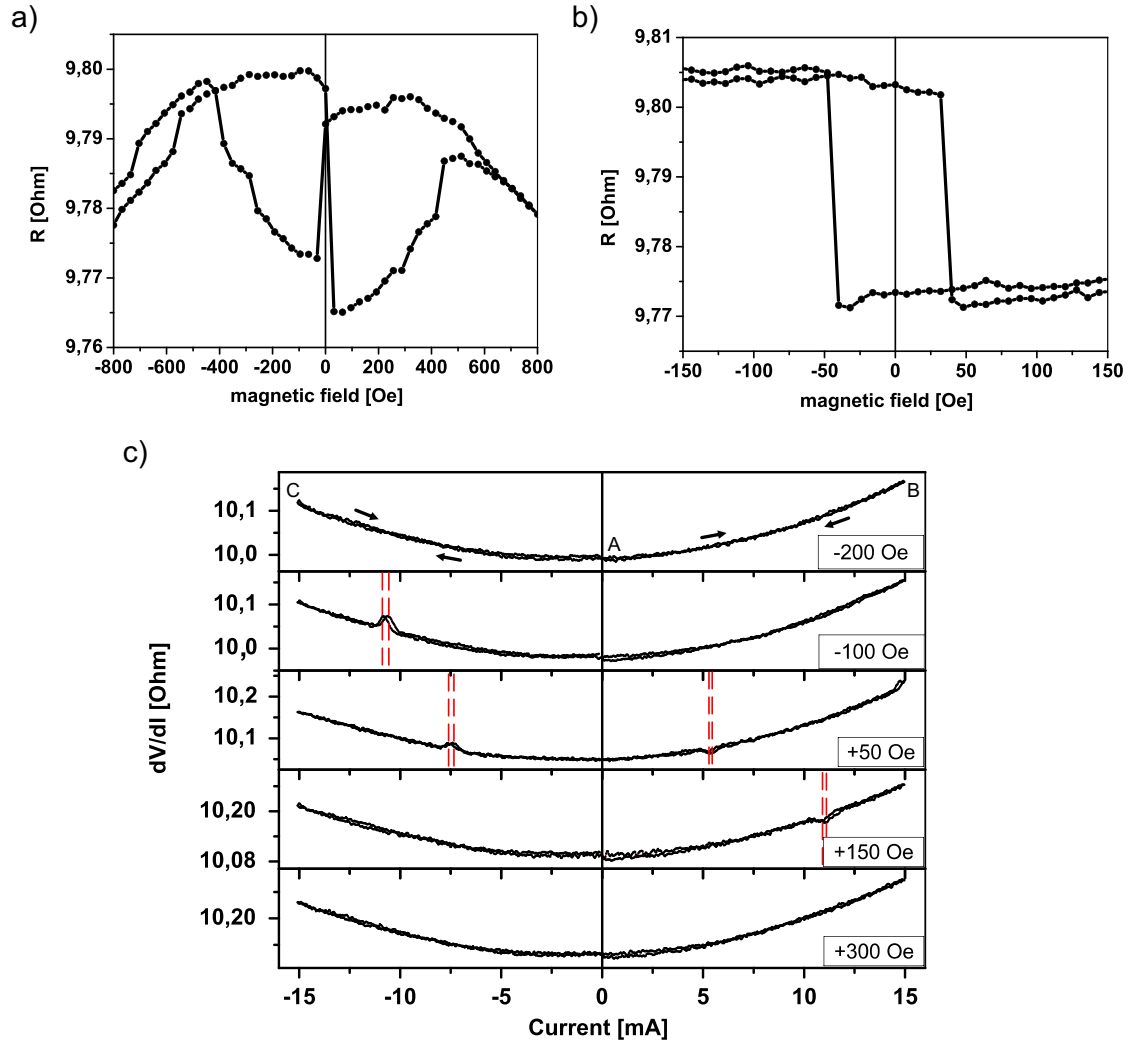
Figure 42: Magnetic major (a) and minor (b) switching loops for an element with artificial antiferromagnet (r=110 nm). (c) Measurement of the transition of switching feature for increasing magnetic fields. The current is subsequently swept through the points A,B,C,A.

In the presented cases of free layers with a relatively high magnetic moment and therefore strong magnetostatic coupling, the simple macrospin model is in good agreement with the presented measurement results. However, the model is a simple approximation of the real device. The oscillations are only found for the $CoFeB(2.5)$ free layer with a relative low magnetic moment, where the hysteresis of the switching features ($dV/dI - I$) is much larger and the

magnetization under the nanocontact is not switched completely. For this case we show in the next section that the Oersted field influence produced by the current flow through the nanocontact is likely to generate a vortex-like magnetization profile, which becomes manipulated by the spin-torque effect for nanocontact sizes below 100 nm.

4.2.5 Micro magnetic simulations of the spin-torque and Oersted field in spin-valve nanocontacts

OOMMF [22, $^{Donahue;99}$] simulations give a micromagnetic insight into the spin-transfer torque and Oersted field influences generated by the perpendicular current flow through the nanocontacted spin-valve multilayer. The OxsSpinXfer evolver[22] in the used code solves the Landau-Lifshitz-Gilbert equation in addition with a spin momentum term, the expression of which is basically given in equation 2.13.

In a first approach, disregarding any spin-torque contribution, simulations are performed for a circular mesa of 1 μm radius with a $r = 100\,nm$ nanocontact. The multilayer stack is simulated according to the model depicted in figure 43, in which the same layer thicknesses are considered as they are presented in figure 28(b). We note here, that the mesa radius is only 1 % of the size
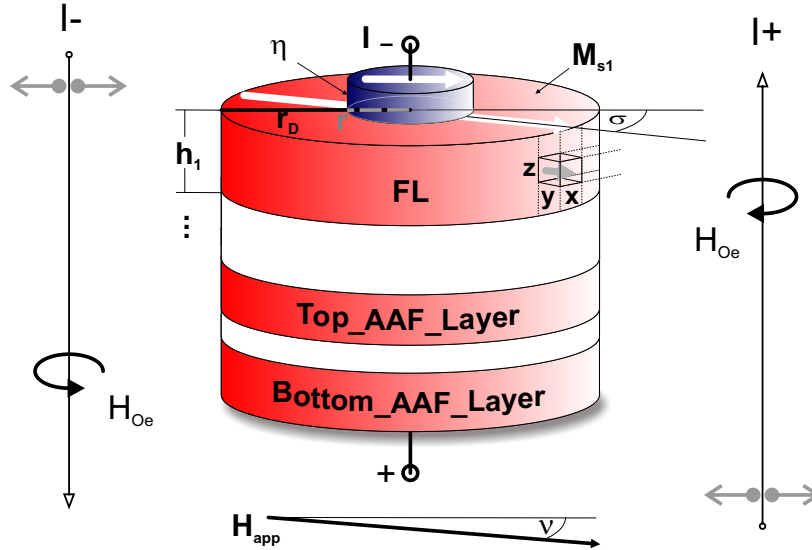
Figure 43: Sketch of the main simulation model parameter used in the OOMMF code: current I, Oersted field H_{Oe}, disc radius r_D, nanocontact radius r, spin polarization η in angle σ to the saturation magnetization M_s, external magnetic field H_{app} (angle ν) and layer thickness h_i for the free layer (FL) and the top and bottom AAF layers.

of our device and was chosen in respect to the computational performance limitation. In this case the disc borders are expected to have a strong influence on the magnetization dynamics

---

[22]OOMMF User's Guide, release 1.2a3, 2008

in contrast to the case of an spin-valve multilayer with more extended magnetic films, as it is discussed in chapter 2.3 and in chapter 2.5. No difference in the qualtitaive behavior is found for increased disc size of 2 μm in simulations that are performed speperatly for the FL and AAF. On the other hand, in the literature a nummerical simulation for the spin-valve nanocontact is only reported for the case where a strong perpendicular magnetic field is present [13, $^{Mistral;PRL;08}$]. In this simulation the perpedicular field creates the vortex state in the free layer before the STT and Oersted field contributions are considered. In our device no perpendicular field is needed to excite the dynamics. The analytical (chapter 2.5) and nummerical treatment of this geometry case is still subject to ongoing research activity. For these reasons the following simulations can only serve as qualitative hint of the Oersted field and STT influence on our spin-valve system. However, some of the basic responces can be deduced from this model approximation.

In our model saturation magnetizations of 1000 and 1950 kA/m and damping constants of 0.006 and 0.01 is assumed for the $CoFeB$ and $CoFe$ layers, respectively. The exchange constant
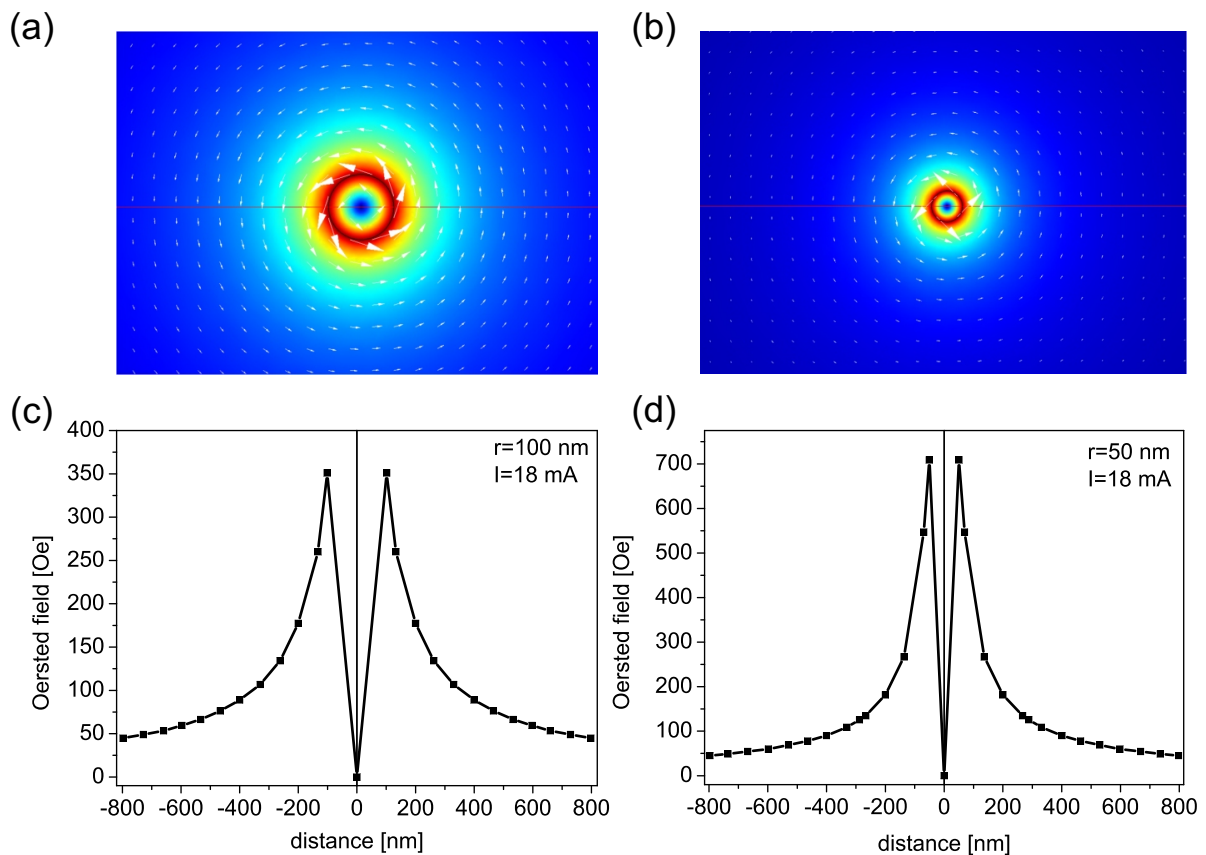
Figure 44: Color plots of the simulated Oersted field produced by a current flow of 18 mA through a $r = 100\ nm$ (a) and $r = 50\ nm$ (b) nanocontact and the corresponding distance versus field strength plots for a horizontal line through the simulation center (c) and (d).

is taken, 3×10^{11} J/m, for both alloys and the antiferromagnetic exchange coupling equal to -0.0015 J/m^2. A cell size of $5 \times 5 \times 1$ nm^3 is used. An Oersted field profile, like it is depicted in figure 44, is generated by the current flow through the nanocontact region. For current densities between 6.4×10^{10} A/m^2 and 3×10^{12} A/m^2 the maximum field strength is simulated[23] to vary between 40 and 900 Oe in the area close to the nanocontact and is decaying proportional to $1/r_c$ like it is expected by the Biot-Savart-Law for an ideal conductor [23, [Nolting;97]]:

$$|B| = \frac{\mu_0 I}{2\pi r_c} \, , \tag{4.23}$$

where $|B|$ is the magnitude of the magnetic field vector, μ_0 is vacuum permeability, I is the current and r_c is the distance to the conductor.

The simulation is started from relaxed magnetization states for free layer and AAF in the assumed disc geometry (Fig. 45), which are calculated for $I = 0$ mA by an energy minimizing solver, considering the magnetic moment interactions in the layers and the coupling of the AAF.
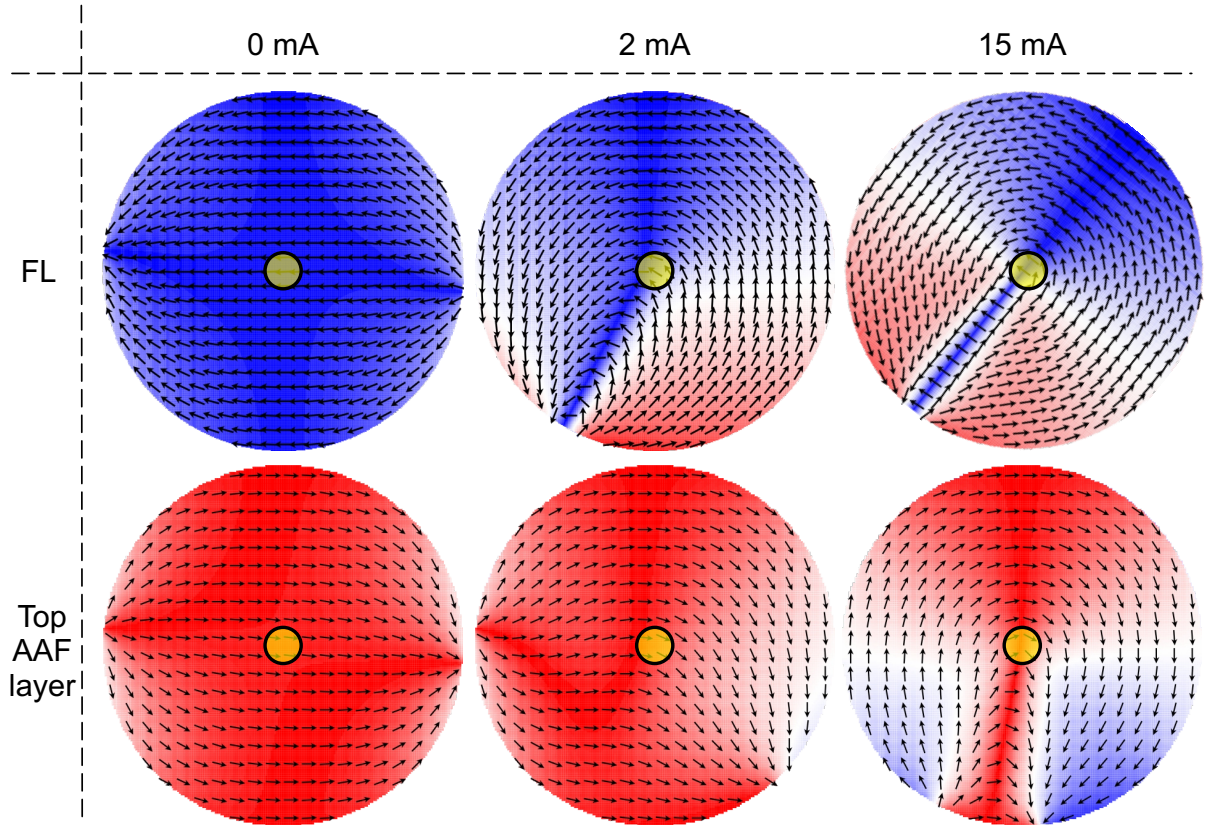
Figure 45: Simulation of the Oersted field contribution on the magnetization profile of a free layer and AAF disc ($r = 1$ μm) caused by an electron flow of 2 mA (6.4×10^{10} A/m^2) and 15 mA (4.8×10^{11} A/m^2) through a $r = 100$ nm contact (yellow circle).

---

[23]Comsol Femlab Multiphysics

In the following only the top AAF layer is presented, since the bottom AAF layer shows almost the same magnetization profile, but mirrored, due to the AAF coupling.

The results in figure 45 show at zero external magnetic field that a highly nonuniform magnetic state is developed in the free layer underneath the nanocontact even for low currents ($I = 2\ mA$, $J = 6.4 \times 10^{10}\ A/m^2$), gradually transforming into a vortex-like state for increasing currents ($I = 15\ mA$, $4.8 \times 10^{11}\ A/m^2$). The generated Oersted exceeds largely the switching field of the free layer, as it is shown in table 9. The AAF presents significantly larger rigidity against

$J\ [A/m^2]$	$H_{Oe}^{max}\ [Oe]$	$H_S^{FL}\ [Oe]$
6.4×10^{10}	40	15
4.8×10^{11}	295	15
5.7×10^{11}	350	15

Table 9: Comparison of free layer switching field, H_S^{FL} to the maximum Oersted field, H_{Oe}^{max} generated at different current densities, J.

the Oersted field, although it gradually adopts a nonuniform magnetization profile for large currents. It has been demonstrated in numerical simulations for a nano-sized pillar geometry[24] [10, *Khvalkovskiy;APL;09*] that, in the absence of a perpendicular field, such a nonuniformity in the polarizing layers magnetization (in this case the AAF) is crucial for the excitation of vortex dynamics.
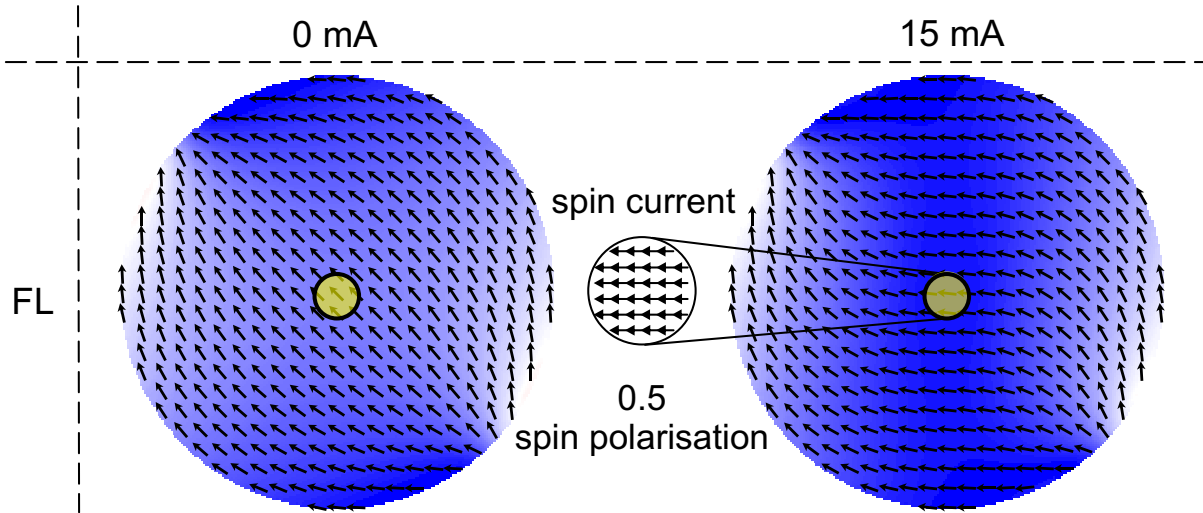
Figure 46: Simulation of the spin transfer torque contribution on the magnetization profile of a free layer disc ($r = 1\ \mu m$) caused by an electron flow of $15\ mA$ with a spin polarization of 0.5 through a $r = 100\ nm$ contact (yellow circle).

---

[24]with a vortex state as initial magnetization distribution in the free layer

In a second approach, considering only the influence of the spin current flow through the nanocontact, simulations are preformed for an assumed spin polarization of 0.5 and a fixed angle spin current (Fig. 46). Only for the low magnetic moment free layer at relativly high current values a significant change in the magnetization profile is observed, orienting the moments towards the applied spin-current direction.

For simulations combining the Oersted field and the spin-torque influence on the magnetization of the layers at the same time no steady precision is observed. This is not surprising since, like it is mentioned in the beginning, the model layer radius of 1 μm is only 1 % of the real device size and our simulations are calculated without a perpendicular field. Further, as it is shown in chapter 2.5, the theoretical model of Kim et al. [5, $^{Kim;CM;10}$] assumes that CIP spin-torques are the origin of the vortex oscillations, which are not considered in our CPP spin-current simulation. The correct numerical and analytical modeling of this system is still subject of on going research activities and is not completely understood yet.

However, our basic simulations can shine some light on the mechanism necessary for a precession of the vortex-like magnetization state under the nanocontact. The measurement results of the previous sections show that the oscillations are nucleated at a critical current density of approximately 5×10^{11} A/m^2. At this current density the simulations suggest that two requirements for the existence of oscillation are fulfilled: (a) the polarizer magnetization (AAF) has acquired the necessary nonuniformity reported by Khvalkovskiy and (b) the spin current is high enough to significantly influence the free layer magnetization.

4.2.6 Conclusion of section 4.2

Spin-torque driven vortex-like oscillations in spin-valve nanocontacts with radii of 40 to 100 nm are measured for current flows of -6 to -25 mA from a $CoFeB(2.5)$ free layer to the unpinned AAF polarizer. The frequency of the Lorentzian like oscillation peaks range from approximately $200-600$ MHz at zero magnetic field. The layer needs to present a certain nonuniformity in its magnetization profile at zero magnetic field, as it is suggested by the reduced remanence measurements in the minor magnetic switching loop of the elements. Oscillation characteristics, like excitation onset and regime, can be correlated to the appearance of resistance features in the dV/dI measurements. The observed changes for the CoFeB free layer are always smaller than the measured total magneto resistance changes and therefore associated with non-uniform magnetization changes in free layer close to the nanocontact. The oscillation persists up to a certain break down current, where the vortex-like magnetization dynamics are believed to lose stability. The oscillation frequency is depending almost linear on the current, as it is expected by a modified Thiele model describing the motion of a rigid vortex-core around a symmetry center. The presented oscillation profiles show a unique nearly reversible frequency dependence on the current, together with an exceptionally low critical nucleation current density. This special properties may prove to be of technological interests. This phenomena can be attributed to the unpinned AAF polarizer and the incorporation of several Ru layers in the stack, which have been reported to enhance the spin-torque effect as well in similar structures.

The influence of the nanocontact size on the excitation characteristics is systematically investigated for contact radii between 40 to 130 nm. Only for radii smaller than 100 nm the balance between Oersted field and spin-transfer torque is of such a kind that oscillations are measurable at zero magnetic field. The power spectral density in dependence on the frequency and current is measured as function of the nanocontact radius, presenting single and multiple oscillation modes. In this investigation the excitation onset current is found to be proportional to r^2, leading to the conclusion that dynamics are initiated at constant current density. The same proportionality to r^2 is found for the currents at the maximum power spectra density. The oscillation frequency presents a decreasing tendency with the radius, as well as the measured df/dI slope. The latter is in contrast to the recent theoretical predictions of Kim et al., where a radius independent df/dI is expected. A possible reason for this difference between experiment and theory is the rigid vortex approximation in the model of Kim et al., which neglects the degree of non-uniformity of the vortex-like magnetization profile in real devices with relatively large nanocontact radius.

For devices incorporating an AAF two different types of free layer materials, namely $CoFe(1)/CoFeB(2.5)$ and $CoFeB(2.5)$, are investigated. Their electron transport measurements show a similar series of current induced hysteretic switching features for nanocontact radii smaller than 100 nm, but of different amplitude. From the corresponding GMR loops can be derived that for the higher magnetic moment free layer a complete switching of the magnetization in reach of the current flow has taken place, while for the lower moment free layer only a part is switched

to an inhomogeneous micro magnetic state. For certain current density values only the lower moment free layer shows sub-GHz excitation in the frequency spectra measurements, leading to the conclusion that the prerequirement for excitation is the establishment of a non-uniform (vortex-like) magnetic state in the free layer, which gets excited if a certain spin-transfer torque contribution is present.

For large nanocontacts and multilayers incorporating a higher magnetic moment free layer, like CoFe(2)/NiFe(4), dV/dI-I measurements show pronounced hysteretic peaks and dips, the relative amplitude and position of these are changing as a function of the in-plane magnetic field. These features appearing for both current polarities can be explained with a macro domain model that takes into account the Oersted field, spin transfer torque, as well as the interlayer exchange and magnetostatic coupling interacting in the detection layer. In this model the combination of Oersted field and spin-torque contribution reorients a domain in reach of the current flow against the magnetostatic coupling of the free layer in direction of the spin current and changes this way the magneto resistance of the spin-valve. For the CoFeB(2.5) free layers with a lower magnetic moment the magnetization under the nanocontact is not switched completely. In this case a more rigorous model needs to take into account the micro magnetic structure of the system.

The influence of the Oersted field and spin-transfer torque on the micromagnetic magne- tization dynamics are simulated in a three dimensional OOMMF model, resembling the stack layers with discs of 1 μm radius. The Oersted field around the nanocontact is assumed to be created by the perpendicular current flow, which can reach a maximum field strength of up to 900 Oe close to the nanocontact and than decays anti-proportional with the radius. The simu- lation results show that the free layer and AAF adopted the circular Oersted field profile in a vortex-like manner, but the AAF presents a much larger rigidity against this change. Such a nonuniformity in the polarizer is reported in the literature to be important for the existence of vortex dynamics. On the other hand the spin-torque effect is shown for a fix angle spin-current to orient the magnetization of the free layer close to the nanocontact in direction of the spin current. The comparison between measurements and simulation suggests that two requirements need to be fulfilled for the existence of oscillation: (a) the AAF's magnetization has acquired the necessary polarizer nonuniformity reported by Khvalkovskiy et al. and (b) the spin current is high enough to significantly influence the free layer magnetization.

4.3 The influence of external magnetic fields and metastability

In this section the oscillation spectra dependence on externally applied magnetic fields is investigated. First, the field influence on the excitation power and linewidth is discussed. Afterwards, the dependence of the oscillation frequency on the field is analyzed with regard to magnetic field sensing application in the nano scale. Finally, the last section discusses the existence of multi-mode spectra and their sub-mode structure in dependence on the applied magnetic field.

4.3.1 Power and linewidth dependence on the external magnetic field

The observed excitations take place in an in-plane field regime close to the free layer switching field. Outside this regime (typically maximum ± 100 Oe) no dynamic excitation is measured. The maximum power spectra density value of the devices at zero field is in the order of several nV^2/Hz and can increase up to 290 nV^2/Hz close to the switching field of the elements. As an example, in figure 47(a) and (b) the easy-axis loops of nanocontacts with radii of 85 nm
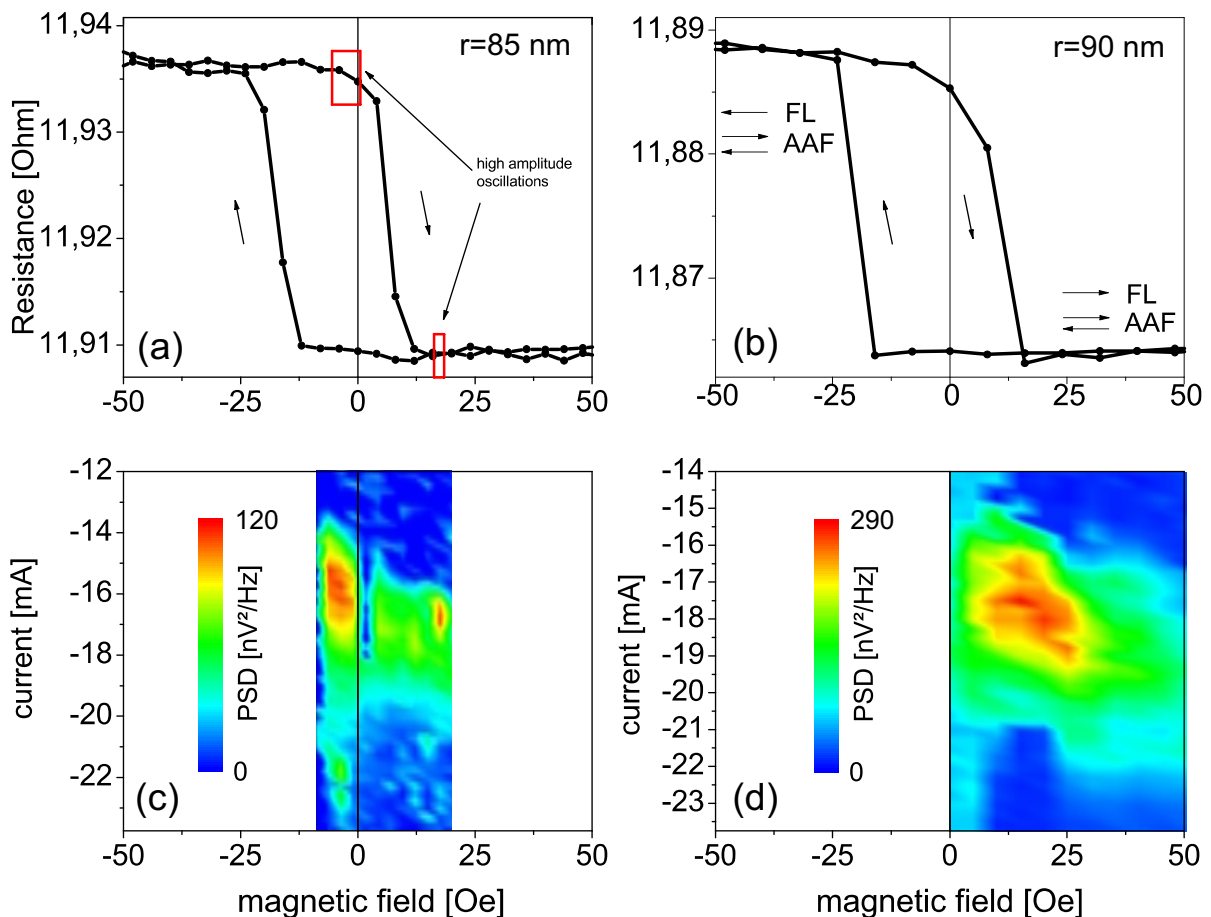
Figure 47: Easy-axis minor loops (a) and (b) in comparison to power plots for current and magnetic field (c) and (d).

and 90 nm together with the respective excitation power-density spectra in the current-field space are presented. The oscillation PSD as a function of the current and field shows different excitation regimes for these similar sized nanocontacts with similar minor switching loops. The latter indicate that already small differences in the magnetization profile, which we attributed to fabrication related defects in the device structure, cause these differences. However, the maximum PSD is always located close to the switching field of the element.

A similar dependence on the magnetization profile is found in a direct comparison between easy- and hard-axis loops of a nanocontact with a radius of 75 nm presented together with the respective excitation power-density spectra in the current-field space (Figure 48).
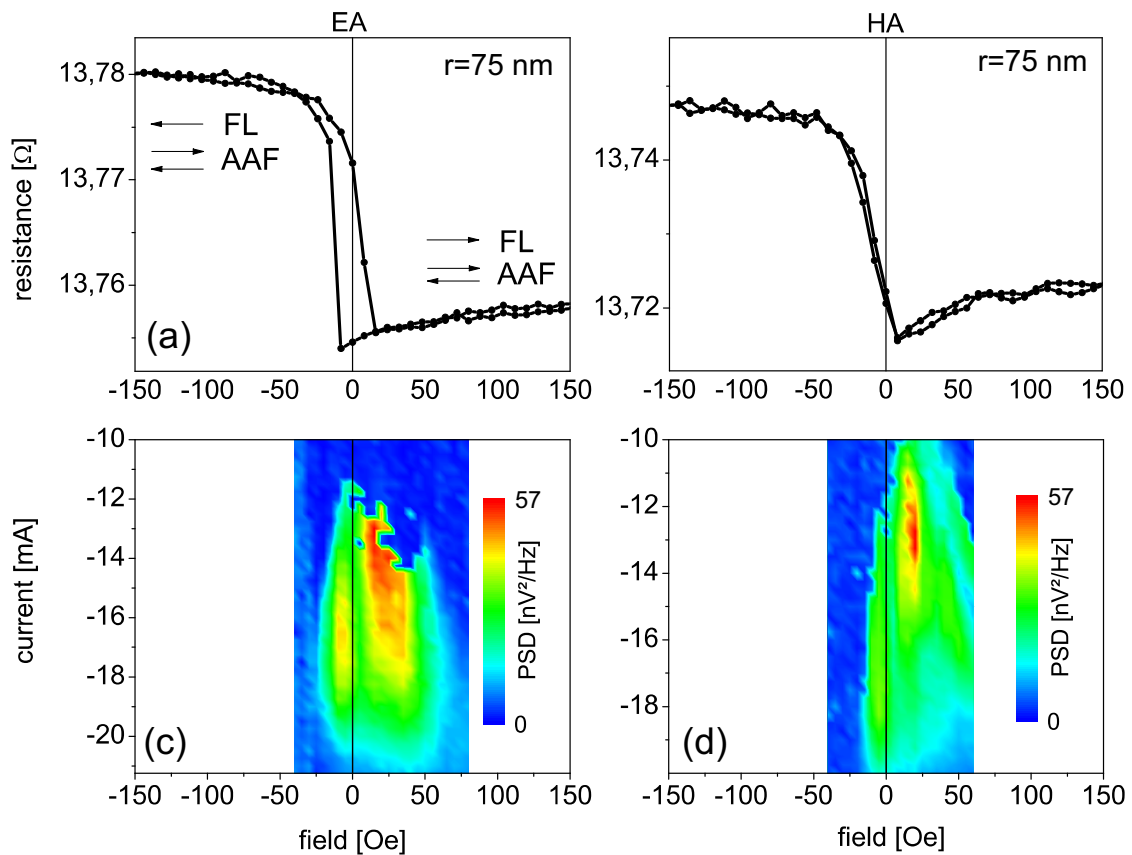
Figure 48: Easy- (a) and hard-axis (b) minor loop of the same element in comparison to PSD plots in dependence on current and magnetic field (c) and (d).

These differences can be deduced in more detail from spectrum measurements, depicted in figure 49 showing PSD maps versus frequency and current as a function of the magnetic field applied along the easy- and hard-axis directions. The detailed investigation of the oscillation frequency dependence on these fields is the focus of the following section 4.3.2.
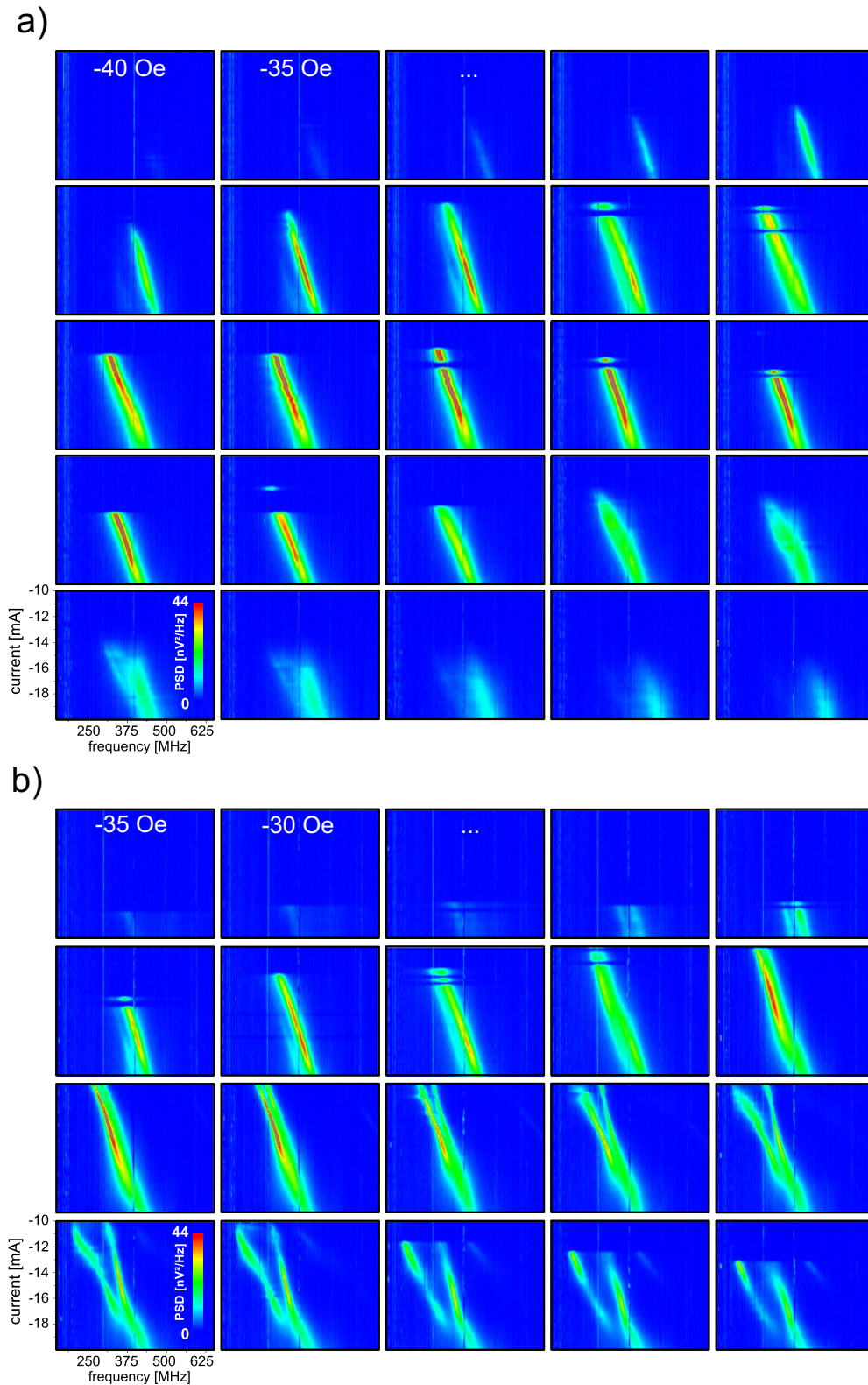
Figure 49: PSD maps vs f and I for different H along easy- (a) and hard-axis directions (b).

The measured oscillation peaks show a Lorentzian line shape, which is expected by the theoretical model of Kim et al. for vortex oscillations in spin-valve nanocontacts, as it is shown in chapter 2.5. The corresponding linewidth of the oscillation peaks ranges between 4 MHz and 48 MHz for our devices. In contrast to the critical oscillation onset current density (j_{cr}) that is almost constant for all measured devices, the linewidth varies from device to device in such a manner that the integral power below the peak remains virtually unchanged. This indicates that the Oersted field necessary to produce the vortex state is largely defined, but the vortex dynamic response fluctuations, determining the linewidth, depend on device-specific properties such as fabrication-related defects, like magnetic defects in the FM spin-valve layers [24, [Pribiag;NatP;07]].

The smallest linewidth is found at P_{max} in the vicinity of the switching field, where it can present a significant narrowing by a factor of up to 5 (Fig. 50), while here as well the integral power below the peak remains constant within small variations. Indeed, larger oscillation amplitudes are generally correlated with decreased linewidth as the dynamics become less sensitive to thermal fluctuations in frequency and amplitude [19, [Kim;PRL;08]],[25, [Thadani;PRB;08]].

The ratio between the center oscillation frequency f_0 and the linewidth Δf is defining the quality factor of the oscillator, which ranges for our system between the values of 10 and 100. These relatively high quality factors together with the ultra compact size of the oscillator and its unique nonhysteretic oscillation characteristic is very interesting in terms of an application as nano-sized oscillation source, as it is discussed in chapter 2.6.
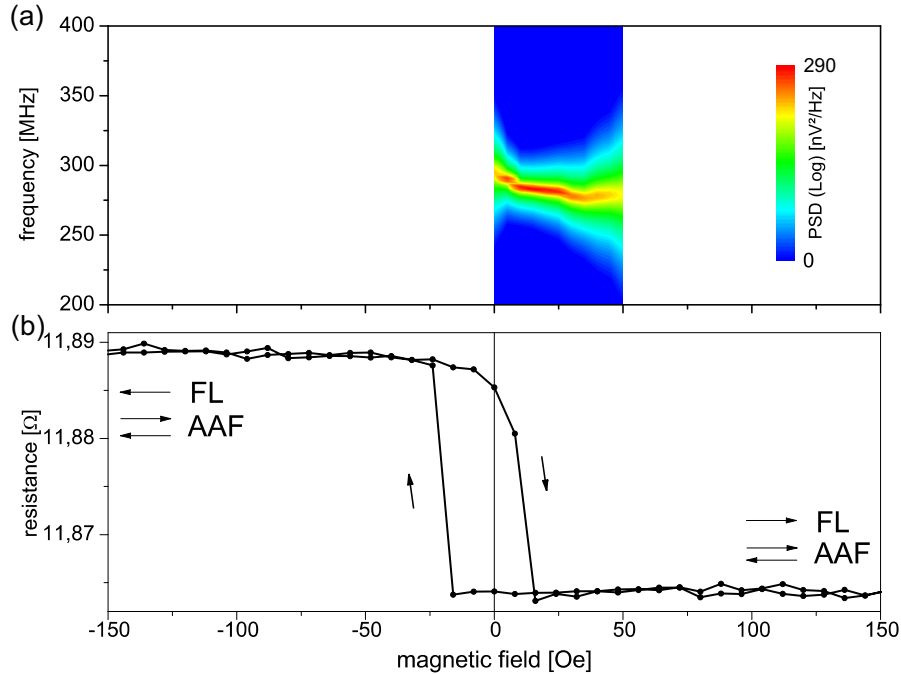
Figure 50: Linewidth narrowing at switching field (a) in comparison to the minor loop (b).

4.3.2 Frequency dependence on in-plane easy- and hard-axis magnetic fields

In the following the differences between magnetic fields applied along the easy- and hard-axis direction on the precession frequency are investigated for relatively large nanocontact radii ranging between 70 and 90 ($\pm$ 10) nm. In general, like it is presented in the previous sections, the characteristics of the frequency response depends on the generated magnetic configuration under the nanocontact. This, in turn, results from the combined effect of the magnetic field applied either in easy- or hard-axis direction, as well as from the current-generated Oersted field. Taking also into account the relative large nanocontact radii, a multitude of possible magnetic configurations can arise with distinctive frequency versus field responses.
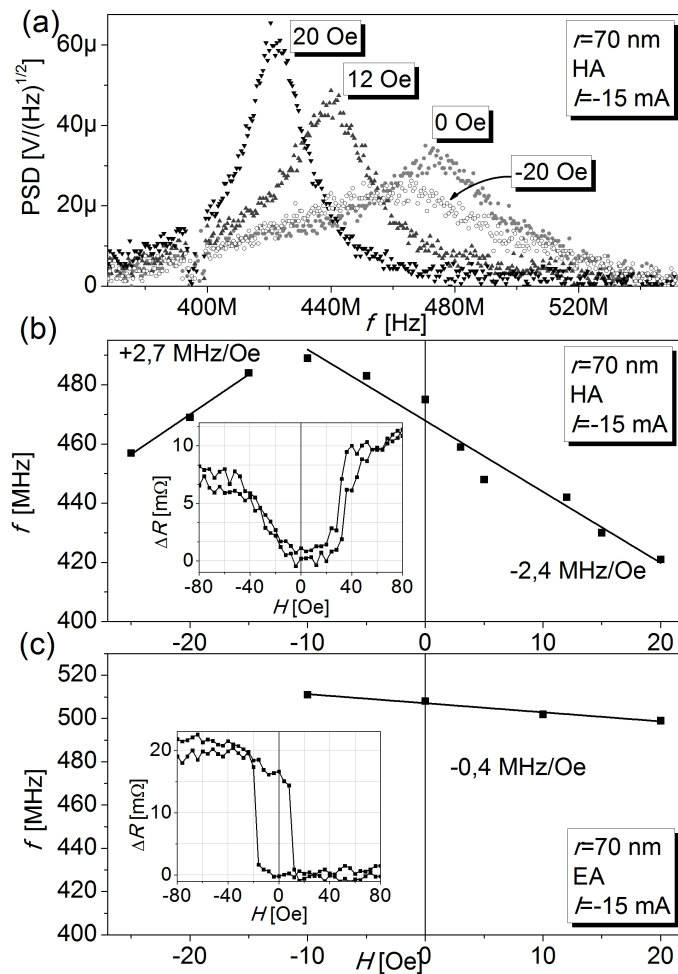
Figure 51: (a) Frequency versus power spectral density (PSD) measurements for different magnetic field values in hard-axis directions for an elements with a nanocontact radius of 70 nm. Frequency dependence on magnetic fields in hard- (a) and easy- (b) axis directions. The insets show the corresponding hard and easy-axis minor loops, measured for small currents ($I \approx 1mA$).

The vortex precession frequency is determined by the balance of energy components as they appear in the modified Thiele equation, as it is shown in chapter 2.5. According to the rigid vortex model based on the Thiele equation, the spin-transfer-torque force counteracts the damping of the system and sets the amplitude of the orbit for a fixed and uniform polarizer. On the other hand, the gyrotropic force counteracts the restoring force (set by the Oersted field) and their balance determines the frequency of motion. In the relatively large nanocontacts studied here, various non-uniform magnetic states can arise [15, $^{Berkov;PRB;09}$], which may differ considerably from the ideal vortex state assumed in the model of Thiele. The applied magnetic field along the easy- or hard-axis direction is adding to the complexity of the system, competing with the Oersted field influence, which tends to stabilize the vortex state.

Figure 51(a) depicts excitation spectra measured for specific magnetic field values along the free layers hard-axis. The frequency versus field dependence is shown in Figure 51(b). A non-monotonic $f(H)$ behavior is observed with the frequency presenting a maximum for $H = -10$
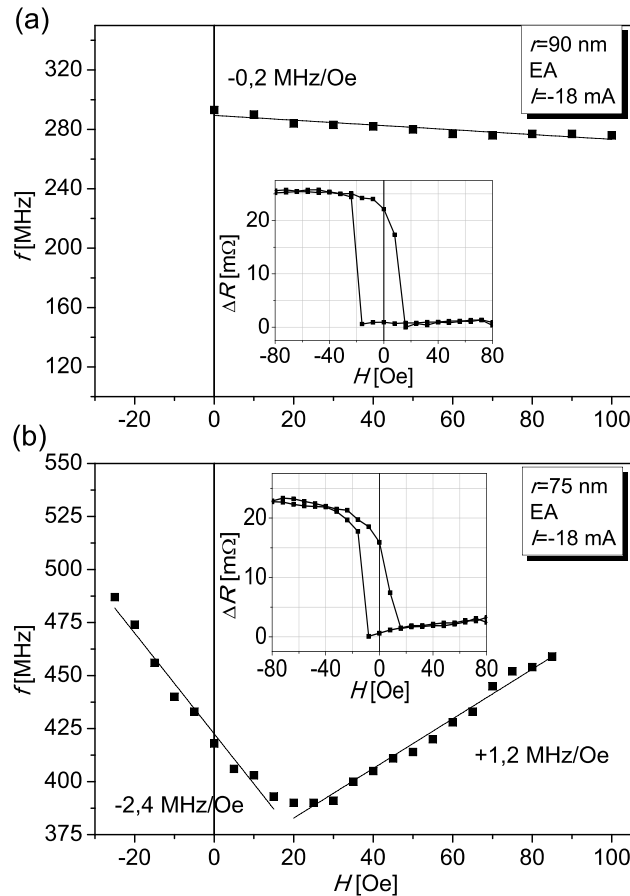
Figure 52: Frequency dependence on magnetic fields applied along the easy-axis direction for an element with a radius of 90 nm (a) and 75 nm (b). The insets show the corresponding easy-axis minor loops, measured for small currents ($I \approx 1 \; mA$).

Oe and decreasing almost linearly with the field, with slopes of ≈ 2.5 MHz/Oe. For easy-axis fields $f(H)$ continuously decreases within the window from -10 to $+20$ *Oe*, with a smaller slope than for hard-axis fields. Similar trends, relevant to magnetic field sensing, are also observed in Ref. [3, *Devolder;APL;09*] and are about 5 times smaller than the ones extracted for nanopillar geometries [26, *Braganca;NT;10*].

Although the majority of nanocontacts present the aforementioned $f(H)$ dependence, the slope of frequency decrease, can vary considerably, as can be seen in Figure 52(a) for a r=90 nm nanocontact. Interestingly, there are cases, like the one in Fig. 52(b), where the $f(H)$ dependence is reversed, i.e. the frequency presents a pronounced minimum instead of a maximum. Moreover, the field window where the excitation persists can vary considerably, even for nanocontacts of similar size (compare Fig. 51(c) with 52(b)). If the different observed trends stem from the competing action of the external magnetic field and the Oersted field, then we should expect that the increase of current should smoothen out the external magnetic field influence on the
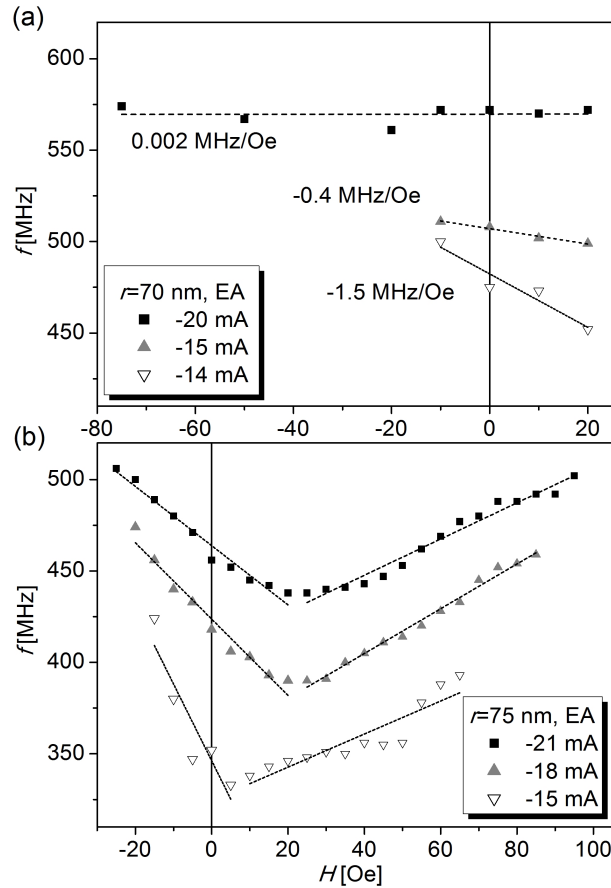
Figure 53: Frequency dependence on the magnetic field applied along the easy-axis direction for different currents, (a) $r = 70$ *nm* and (b) $r = 75$ *nm*.

precession frequency, since the Oersted field is significantly increased (compare table 9 in section

4.2.5), stabilizing the vortex state against the external field influence.

Figure 53 demonstrates the effect of increasing current on the $f(H)$ dependence for a 70 and 75 nm nanocontact and easy-axis magnetic fields. The trend is particularly obvious for the 70 nm nanocontact. The $f(H)$ slope gradually decreases with increasing current until finally the frequency is almost constant over the field. The increase of frequency with the current is predicted from the modified Thiele model, as shown in equation 2.20. Additionally, the magnetic field window where precession takes place is significantly enhanced with increasing current. This is anticipated since the stabilization of the vortex state beneath the nanocontact with increasing Oersted field will lead to a decreased interaction with the external field. For the 75 nm nanocontact the previous observations are applied, although the trend of decreasing $f(H)$ slope with increasing I can only be safely deduced for decreasing fields (left arm relative to the minimum).

These STO devices could possibly be used as nano-sized alternative to conventional MR sensors. The latter can achieve today a signal-to-noise ratio (SNR) in the range of 27-33 dB. The sensor SNR is determined by the amount of frequency modulation one can expect from the sensed magnetic field (the base-to-peak signal power) and the mean-squared fluctuation in the frequency (the noise power) [26, [Braganca;NT;10]]. Braganca et al. estimate the STO SNR by approximating the spectral line of the oscillator as a Gaussian, with its full width at half maximum (FWHM). In their assumption the SNR then becomes

$$SNR \approx 10 \, Log_{10}[2 \, ln(2)(\frac{\Delta f}{FWHM})^2] \, , \tag{4.24}$$

so that a 30 dB SNR requires a Δf to linewidth ratio of 26:1, while 40 dB requires a larger ratio of 84:1. We assume for our devices a frequency shift, Δf, in the order of 100 MHz as response to small, in-plane magnetic fields, a maximum linewidth in the order of 5 MHz would have to be achieved to reach SNR of 27 dB. A significant improvement of our STO device oscillation quality, which can lead to SNR values in the order of 10 dB, is therefore necessary to reach beyond the limit of conventional MR sensors.

4.3.3 Multi-mode-vortex oscillations and metastability

Another important phenomenon is the observation of multiple oscillation modes for nanocontact radii between 75 nm and 85 nm. The relative amplitude and position of these modes in the current and frequency space changes with the application of small, in-plane magnetic fields.
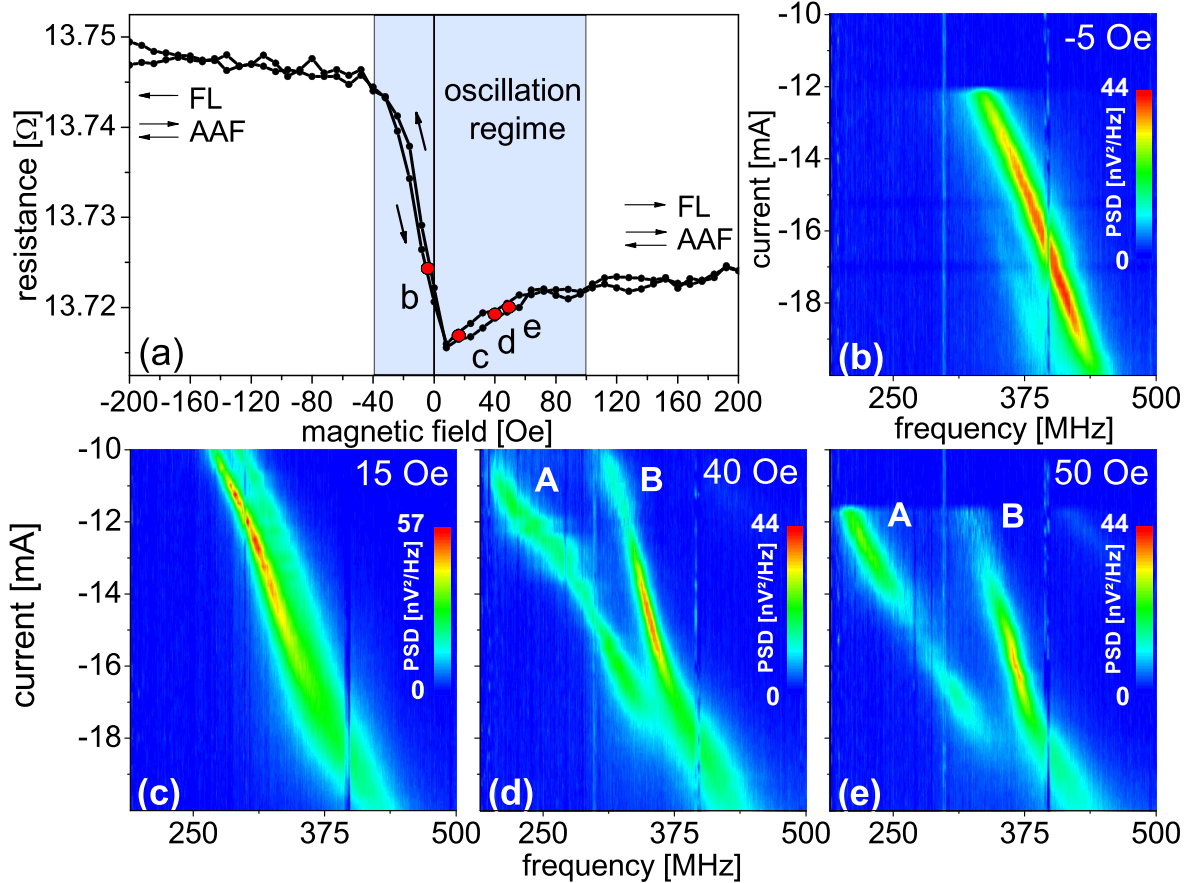
Figure 54: (a) Hard-axis switching loop at low current (r=90 nm). (b) Power spectrum map vs frequency and current for (b) 5, (c) 15, (d) 40, and (e) 50 Oe fields.

Such mode metastability could be demonstrated for hard- and easy-axis, in-plane fields in the vicinity of the switching field of the elements. As an example, in figure 54 power density spectra of a nanocontact with a radius of 75 nm for fields within the hard-axis free layer switching are presented.

For certain field values only one high frequency peak can be distinguished (Figs. 54(b) and (c)). This progressively separates to a double peak for low current (Fig. 54(d)). Eventually for larger magnetic fields, two completely separated peaks are obtained, which are not harmonically correlated named A and B in figure 54(d) and (e). Both peaks increase their frequency with the current, but at different rates. Very different is also their dependence on the magnetic field. While the frequency of B remains almost unaffected, excitation A varies its frequency rapidly
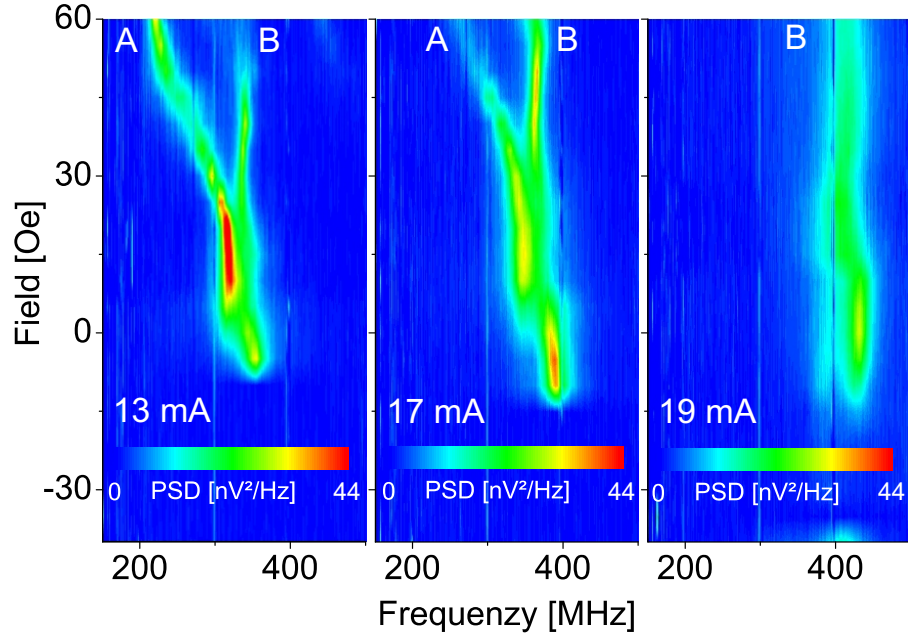
Figure 55: PSD plots in dependence on frequency and field for 13, 17 and 19 mA of current.

(Fig. 55).

For another element with a nominal nanocontact radius of 75 nm similar effects are obtained with H at low currents and for magnetic fields along the easy-axis direction (Fig. 56). At a magnetic field value of -20 Oe and 0 Oe, two modes are clearly distinguished. These merged into one at a field of $+20$ Oe. The existence of multiple localized modes has been predicted by Berkov and Gorn [15, $Berkov;PRB;09$] as a demonstration of the strongly inhomogeneous and
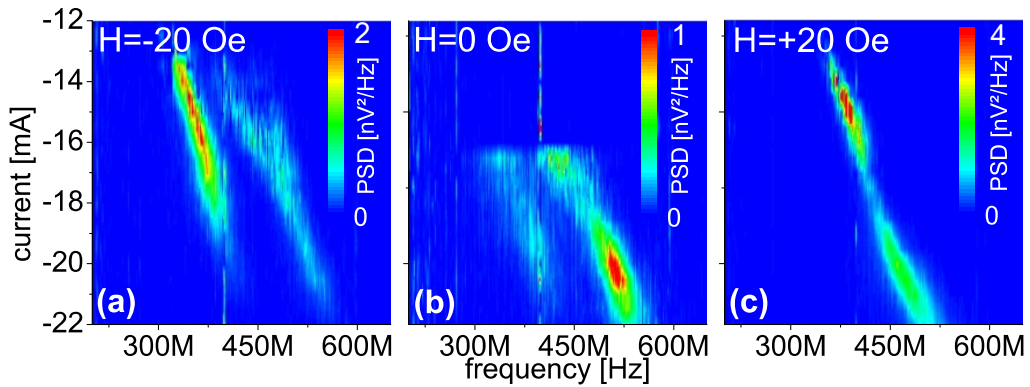
Figure 56: PSD plots versus current and frequency for (a) -20, (b) 0 and (c) +20 Oe.

spatially extended magnetic configurations in these relatively large nanocontacts. The different behaviors of the two peak spectra with regard to current and field suggest that the systems hop between two metastable dynamic states, with different degrees of magnetic nonuniformity.

Excitation B in figure 54(e) can be attributed to a vortex structure, i.e., the one with the highest nonuniformity. This is suggested by its weak dependence on the magnetic field (Fig. 55) and its dominance for increased current densities where the Oersted field is more pronounced.

Figure 57(a) shows a sketch which is meant to illustrate this metastability model for the existence of two modes. There the oscillation can be generated by two different vortex-like magnetization profiles with different degree of uniformity, which precess on two different main precession trajectories around the nanocontact. The system can hop between both main trajectories. Additionally, it is possible that beside the hopping for a certain period of time a superposition of both profiles simultaneously oscillates in the system. The individual peak linewidth is assumed to be generated by a wobbling of vortex core around its main trajectories at room temperature. This agrees with other results in the literature [24, $^{Pribiag;NatP;07}$],[16, $^{Kuepferling;APL;10}$]. The
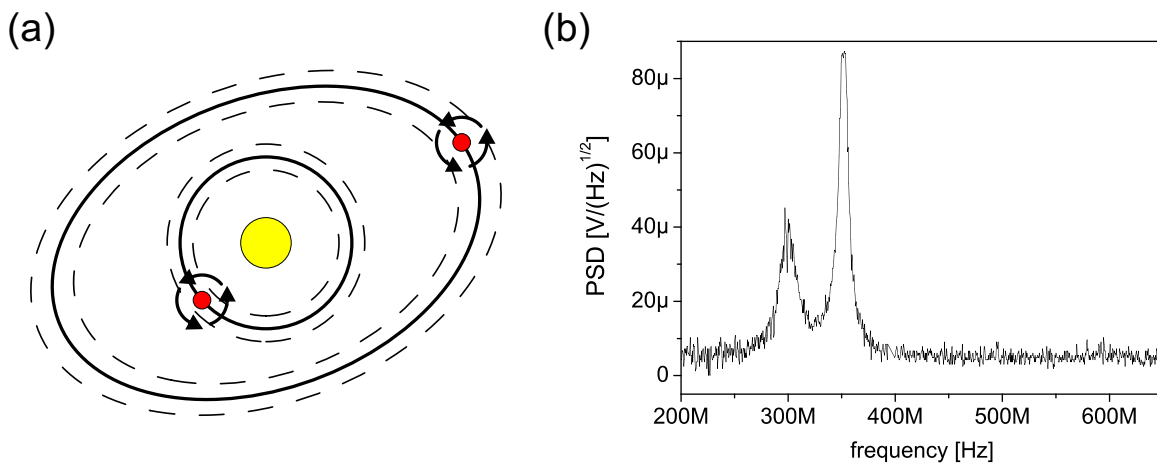
Figure 57: (a) Model of two metastable main mode trajectories around the nanocontact center. (b) Double peak frequency spectrum.

results of Pribiag et al. suggest that for the presence of defects in the free layer, the vortex can undergo jumps/wobbles between slightly different, metastable trajectories, corresponding to transitions between local minima of the confining potential, which leads to the observed linewidth broadening.

For certain current and field values a splitting of the oscillation peak into a sub-peak structure is observed for several elements with relatively low oscillation quality factors between 15 and 20. As an example, figure 58 presents such a splitting of one oscillation peak for a double peak spectrum. The measurements are derived from a nanocontact with a nominal radius of 75 nm. The splitting is observed at zero magnetic field and for currents close to the onset of the oscillation regime 58(b). In the present case the higher frequency mode shows the fine structure, while the other mode is measured without it. For increasing currents the splitting disappears and the linewidth of the oscillation peak decreases, as it can be seen in figure 58(b) for the higher

frequency mode.
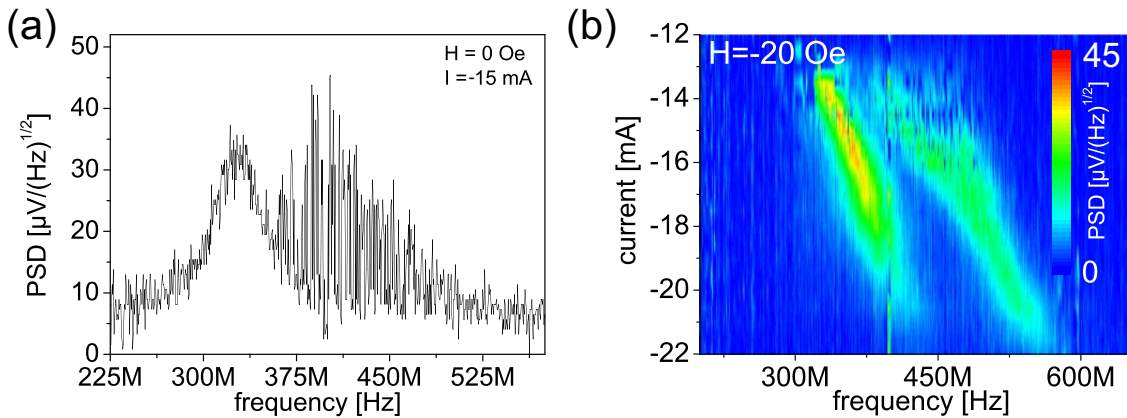
Figure 58: (a) Double peak frequency spectrum shows substructure for one peak at -20 Oe and (b) corresponding power plot in dependence on current and frequency.

A comparable sub-structure is measured for elements with a single peak spectrum (Fig. 59(a)). Subsequently, the same spectrum regime is measured in the "maximum-hold-modus" of the spectrum analyzer. In this modus for each frequency sweep only the maximum measured PSD values are stored. This means that in a subsequently following sweep cycle only those PSD values are stored which exceed the ones of the previous sweep cycle. This way it is possible to trace fluctuating oscillation signals over a certain period of time. Figure 59(b) shows a 60 second "maximum-hold" measurement for a frequency sweep cycle of 1 second. The individual sub-mode structure peaks have summed up to closed Lorentzian peak curvature.

This observation can as well be understood by the metastability model proposed in the previous section, if the time average oscillation measurement is assumed as composed of a certain amount of single vortex-core trajectories. The measured linewidth than results as the sum of each individual core trajectory, which becomes modified by thermal influences during the measurement period. For a period of 100 ms the vortex-like magnetization profile can precess for example up to 30×10^6 around the nanocontact. Since the substructure is caused close to the onset of oscillation regime it can be assumed that the system hops between an "on" and "off" oscillation state. For a certain period of time only some specific trajectories are measured as single peaks in the average spectrum, which have randomly wobbled within the normal linewidth distribution.
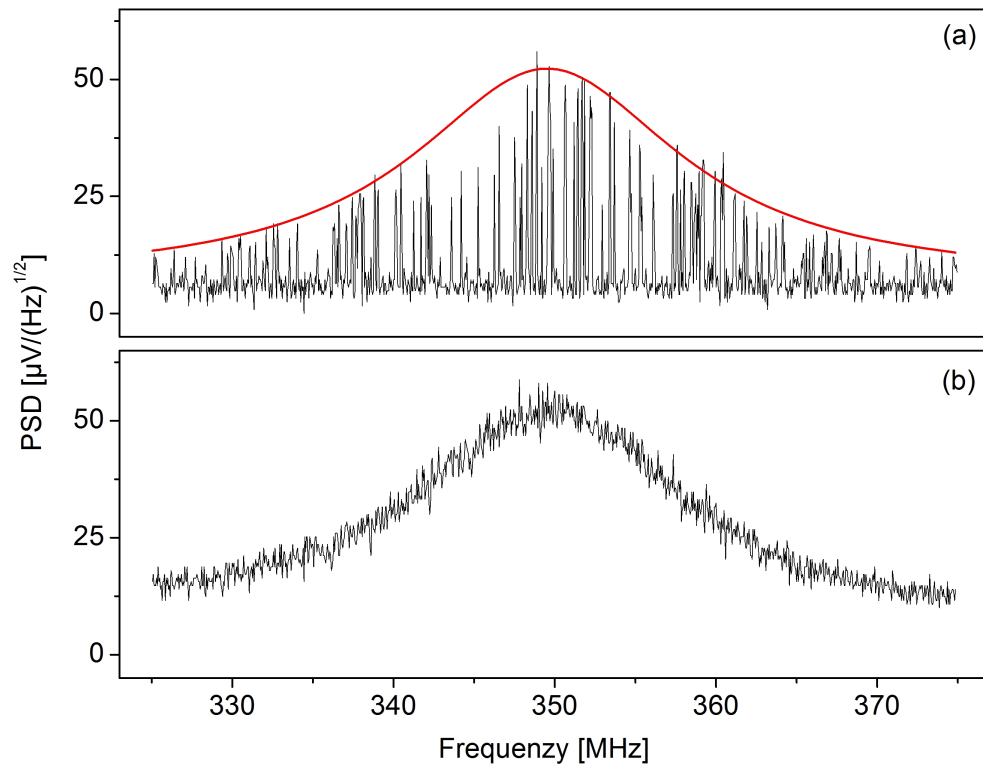
Figure 59: (a) Frequency peak shows submode structure. (b) After a certain integration time in the "maximum-hold-mode" the submode structure disappears and a Lorentzian curve is fitted (Quality factor $Q \approx 17$).

4.3.4 Conclusion of section 4.3

The observed vortex-like oscillation only takes place for a magnetic field window close to the free layer switching and the maximum power spectral density is measured right at the switching field. At this field the magnetization profile provides optimum conditions for a strong periodic GMR change. For in-plane hard-axis fields the maximum power density regime narrows and sifts to higher positive field values. The oscillation linewidth ranges between 4 and 48 MHz, presenting the most narrow linewidth close to maximum power density, while the integral power below the peak remains constant within small variations. As it is shown in the literature, larger oscillation amplitudes are generally correlated with decreased linewidth as the dynamics become less sensitive to thermal fluctuations in frequency and amplitude. On the other hand, for different elements the integral power density below an individual peak stays the same and indicates that the Oersted field necessary to produce the vortex state is largely defined, but the vortex dynamic response fluctuations, determining the linewidth, depend on device-specific properties such as fabrication-related defects. The oscillation dynamics present quality factors ranging between 10 and 100. A result which can be, together with the ultra compact size of the devices and its non-hysteretic excitation characteristic, of technological interest.

The oscillation frequency dependence on external in-plane magnetic fields applied along the easy- and hard-axis direction presents positive and negative slopes with values varying between -2.4 and $+2.7$ MHz/Oe. The vortex precession frequency is shown to be determined by the balance of energy components as they appear in the modified Thiele equation. In the relatively large nanocontacts studied here, various non-uniform magnetic states can arise, which may differ considerably from the ideal vortex state assumed in the model of Thiele. The applied magnetic field along the easy- or hard-axis direction is adding to the complexity of the system, competing with the Oersted field influence, which tends to stabilize the vortex state. The more vortex-like the magnetization profile of a mode becomes with increasing Oersted field, the less pronounced is the external field dependence, since the Oersted field contribution is much stronger than the external field. Devices operated at low currents close to the nucleation of the excitation provide the highest sensitivity to magnetic fields and are therefore best suited for potential magnetic field sensor applications. However, a significant improvement of the device oscillation quality is necessary to provide a good alternative for conventional MR sensors.

Metastable multi-mode-vortex oscillations are observed for nanocontact radii between 75 and 85 nm, for hard-axis and easy-axis fields. These multi-modes dynamics can be manipulated by currents as well as magnetic fields in the vicinity of the elements free layer switching field and cause a splitting from one mode to two not harmonically correlated modes. These modes are associated by magnetization profiles with different degree of nonuniformity and are predicted in the literature for a strongly inhomogeneous and spatially extended magnetic configurations in relatively large nanocontacts. These can be associated with more or less vortex-like magnetization profiles, the distinction of which is possible by their magnetic field versus frequency dependence. In a possible scenario these modes can be illustrated as metastable vortex-core precession trajectories around the nanocontact. The system can hop between these, by a certain potential energy barrier separated, trajectories. The individual peak linewidth is influenced by the thermally activated wobbling of the vortex-core around the basic mode trajectory. This wobbling is assumed to lead as well to the measured splitting of certain modes into a sub-structure, which is observed close to the onset of oscillation regime at zero magnetic field.

References

[1] W.F. Magie. *Principles of physics, designed for use as a textbookk of general physics.* 1911.

[2] K. Uchida, S. Takahashi, K. Harii, J. Ieda, W. Koshibae, K. Ando, S. Maekawa, and E. Saitoh. Observation of the spin seebeck effect. *Nature*, 455(7214):778–781, October 2008.

[3] P. Crozat C. Chappert M. Manfrini M. van Kampen W. Van Roy L. Lagae G. Hrkac T. Devolder, J.-V. Kim and T. Schrefl. Time-resolved zero field vortex oscillations in point contacts. *App. Phys. Lett.*, 95(1):012507, 2009.

[4] S. I. Kiselev, J. C. Sankey, I. N. Krivorotov, N. C. Emley, R. J. Schoelkopf, R. A. Buhrman, and D. C. Ralph. Microwave oscillations of a nanomagnet driven by a spin-polarized current. *Nature*, 425(6956):380–383, September 2003.

[5] T. Devolder J.-V. Kim. Theory of the power spectrum of spin-torque nanocontact vortex oscillators. *cond-mat.mtrl-sci*, arXiv:1007.3859v1, 2010.

[6] A. Dussaux, B. Georges, J. Grollier, V. Cros, A.V. Khvalkovskiy, A. Fukushima, M. Konoto, H. Kubota, K. Yakushiji, S. Yuasa, K.A. Zvezdin, K. Ando, and A. Fert. Large microwave generation from current-driven magnetic vortex oscillators in magnetic tunnel junctions. *Nat Commun*, 1:8–, April 2010.

[7] A. V. Khvalkovskiy, J. Grollier, N. Locatelli, Ya. V. Gorbunov, K. A. Zvezdin, and V. Cros. Nonuniformity of a planar polarizer for spin-transfer-induced vortex oscillations at zero field. *App. Phys. Lett.*, 96(21):212507, 2010.

[8] M. Manfrini W. van Roy L. Lagae T. Devolder, J.-V. Kim and C. Chappert. Vortex nucleation in spin-torque nanocontact oscillators. *App. Phys. Lett.*, 97(7):072512, 2010.

[9] Manfrini M. Devolder T. Kim J-V. van Roy W. Lagae L. Otxoa, R. M. and C. Chappert. Nanocontact size dependence of the properties of vortex-based spin torque oscillators. *physica status solidi (b)*, 248:16151618, 2011.

[10] A.V. Khvalkovskiy, J. Grollier, A. Dussaux, K.A. Zvezdin, and V. Cros. Vortex oscillations induced by spin-polarized current in a magnetic nanopillar: Analytical versus micromagnetic calculations. *Phys. Rev. B*, 80:140401, October 2009.

[11] W. H. Rippard, M. R. Pufall, S. Kaka, S. E. Russek, and T. J. Silva. Direct-current induced dynamics in $co_{90}fe_{10}/ni_{80}fe_{20}$ point contacts. *Phys. Rev. Lett.*, 92:027201, January 2004.

[12] M. R. Pufall, W. H. Rippard, M. L. Schneider, and S. E. Russek. Low-field current-hysteretic oscillations in spin-transfer nanocontacts. *Phys. Rev. B*, 75:140404, April 2007.

[13] Q. Mistral, M. van Kampen, G. Hrkac, J.-V. Kim, T. Devolder, P. Crozat, C. Chappert, L. Lagae, and T. Schrefl. Current-driven vortex oscillations in metallic nanocontacts. *Phys. Rev. Lett.*, 100:257201, Jun 2008.

[14] A. Ruotolo, V. Cros, B. Georges, A. Dussaux, J. Grollier, C. Deranlot, R. Guillemet, K. Bouzehouane, S. Fusil, and A. Fert. Phase-locking of magnetic vortices mediated by antivortices. *Nat Nano*, 4(8):528–532, August 2009.

[15] D. V. Berkov and N. L. Gorn. Spin-torque driven magnetization dynamics in a nanocontact setup for low external fields: Numerical simulation study. *Phys. Rev. B*, 80:064409, August 2009.

[16] M. Kuepferling, C. Serpico, M. Pufall, W. Rippard, T.M. Wallis, A. Imtiaz, P. Krivosik, M. Pasquale, and P. Kabos. Two modes behavior of vortex oscillations in spin-transfer nanocontacts subject to in-plane magnetic fields. *App. Phys. Lett.*, 96(25):252507, 2010.

[17] Y. Jiang, S. Abe, T. Ochiai, T. Nozaki, A. Hirohata, N. Tezuka, and K. Inomata. Effective reduction of critical current for current-induced magnetization switching by a ru layer insertion in an exchange-biased spin valve. *Phys. Rev. Lett.*, 92:167204, April 2004.

[18] D.C. Ralph and M.D. Stiles. Spin transfer torques. *Journal of Magnetism and Magnetic Materials*, 320(7):1190 – 1216, 2008.

[19] J.-V. Kim, V. Tiberkevich, and A.N. Slavin. Generation linewidth of an auto-oscillator with a nonlinear frequency shift: Spin-torque nano-oscillator. *Phys. Rev. Lett.*, 100:017207, January 2008.

[20] J. A. Katine, F. J. Albert, R. A. Buhrman, E. B. Myers, and D. C. Ralph. Current-driven magnetization reversal and spin-wave excitations in co /cu /co pillars. *Phys. Rev. Lett.*, 84:3149–3152, April 2000.

[21] M. Tsoi, A. G. M. Jansen, J. Bass, W.-C. Chiang, V. Tsoi, and P. Wyder. Generation and detection of phase-coherent current-driven magnons in magnetic multilayers. *Nature*, 406(6791):46–48, July 2000.

[22] M. J. Donahue and D. G. Porter. Interagency report no. nistir 6376, national institute of standards and technology, gaithersburg, md. *OOMMF Users Guide, Version 1.O*, 1999.

[23] W. Nolting. *Grundkurs Theoretische Physik 3: Elektrodynamik*. Vieweg, 1997.

[24] V. S. Pribiag, I. N. Krivorotov, G. D. Fuchs, P. M. Braganca, O. Ozatay, J. C. Sankey, D. C. Ralph, and R. A. Buhrman. Magnetic vortex oscillator driven by d.c. spin-polarized current. *Nat Phys*, 3(7):498–503, July 2007.

[25] K. V. Thadani, G. Finocchio, Z.-P. Li, O. Ozatay, J. C. Sankey, I. N. Krivorotov, Y.-T. Cui, R. A. Buhrman, and D. C. Ralph. Strong linewidth variation for spin-torque nano-oscillators as a function of in-plane magnetic field angle. *Phys. Rev. B*, 78:024409, July 2008.

[26] B.A. Wilson J.A. Katine S. Maat P.M. Braganca, B.A. Gurney and J.R. Childress. Nanoscale magnetic field detection using a spin torque oscillator. *Nanotechnology*, 21(23):235202, 2010.

5 Summary and Outlook

Spintronic devices like the spin-transfer torque (STT) driven nano-oscillator presented in this thesis have a high potential for future applications, for example as nano-sized oscillation source in the fields of mobile telecommunication, information and biomedical-technologies, i.e, as fast and non-volatile computer memory-cell or as magnetic field sensor. In such magnetic spin-valve devices a spin polarized current is generated, which exerts a spin-transfer torque on the magnetic moments of a free magnetic layer. This torque can cause the moments to switch their orientation or to drive them into a harmonic precession. Since the first prediction of the STT technological potential in 1996 and its first experimental demonstrations in the years 1998 and 2003, a tremendous research effort has taken place, turning the field to one of the hot scientific topics of the recent years. Of special interest today is the STT driven stable gyrotropic precession of a magnetic vortex in spin-valve nanopillars and nanocontacts. The latter in general presents an advantageous oscillation quality in comparison to pillar devices. The nanocontact excitations fall into the sub-GHz to low GHz regime even at zero external magnetic field, which is the most relevant frequency range for many applications. Another advantage comes with the possibility of excitation synchronization in an array of nano-contacts initially reported in 2010, which can lead to a significant power increase. On the other hand, the largest drawback of STT oscillator devices is the relatively high spin current density needed to excite the oscillations.

The device concept developed, fabricated and measured in this thesis reduces the required current density 6 to 17 times in comparison to other values reported in the literature to a value of 5 to 7×10^{11} A/m^2. This result is achieved by the special device design of the spin-valve multilayer, in which for the first time an artificial antiferromagnet (AAF) polarizer together with an amorphous CoFeB free layer and several Ru layers was used in a GMR nanocontact geometry. Beside the significant critical current density reduction, the system provides a previously unreported almost non-hysteretic oscillation spectrum with regard to the sourced current. This kind of spectrum can be of high technological interest due to the simplified addressing of a desired oscillation frequency by the current.

The measured voltage oscillations are associated with non-uniform vortex-like magnetization states, which precess under the nanocontact. This precession periodically modulates the alignment of the magnetic moments in the system, leading to a change in the giant magnetoresistance of the multilayer in the 200 to 600 MHz frequency regime. According to the OOMMF simulations presented in this work, the vortex-like symmetry seems to be formed by the circular Oersted field, which is caused by the perpendicular electron current flow through the nanocontact. The simulations and differential resistance measurements further suggest that when a certain non-uniformity in the AAF structure and in the free layer is created, the STT becomes strong enough to initiate the precession dynamics. This interpretation is in agreement with the analytical prediction of a modified Thiele equation, which describes the oscillation of a rigid vortex-core around a symmetry center. In the model the oscillation frequency is given by the

balance between a restoring force (the Oersted field) and the gyration force, together with the STT force acting against the damping force of the system.

For a given device geometry the measurement parameter space is defined by the sourced current and the applied magnetic field. The excitations are generated in a stable frequency regime with a certain power spectral density distribution. Only for one current polarity, i.e. the one for which the electrons flow from the free layer to the polarizer, oscillations are observed. At zero magnetic field, typically the Lorentzian frequency peaks can be tuned almost linearly as function of the source current. The power spectral density distribution forms a Gauss-like envelop over this regime with oscillation quality factors of up to 100. For the nucleation process a certain non-uniformity in the magnetization profile seems to be crucial, which is deduced from the comparison of the minor magnetic field loops of the GMR elements. On the other hand, the oscillations break down when a certain maximum current value is reached. This phenomenon is attributed to the loss of stability in the vortex motion.

The magnetic moment of the spin-valve free layer and the size of the nanocontact are found to be key performance factors of the oscillator and are investigated in detail. Parts of this analysis show that when comparing two almost equal devices, one with a CoFe(1)/CoFeB(2.5) and the other with a CoFeB(2.5) free layer, only the latter one (single layer with lower magnetic moment) exhibits sub-GHz oscillations. For both systems current induced hysteretic STT switching was found in the dV/dI measurements, but of different amplitude. This result leads to the conclusion that in the high magnetic moment case the moments have switched completely. For the lower magnetic moment free layer, the creation of a non-uniform magnetic state (e.g. a vortex state), has taken place under the nanocontact. This non-uniformity together with a matching spin-transfer contribution seems to be necessary requirements for the existence of excitation.

Furthermore, the investigations show that a nanocontact size of 100 nm in radius is the upper limit for oscillations in our system. At this size, the Oersted field contribution is expected to be much larger than the STT force and prohibits the dynamics. The measurement spectra show that the critical oscillation onset scales with the square of the contact radius, showing that the excitation is always initiated at a constant current density. The same type of dependence is found for the current value at maximum PSD, while the according frequency value at this power presents a decreasing tendency with the nanocontact radius. Of special interest is also the decreasing tendency of the df/dI slope with the nanocontact radius. This experimental result is in contrast to the analytical predictions of Kim et al. for these kinds of nanocontact systems, which is still in the development phase.

A special focus of this thesis is also to investigate the dependence of the oscillation frequency on the external magnetic field, which can be applied in various directions with regard to the magnetic components of the spin-valve. This dependence turns the device into an interesting candidate for a nano-sized magnetic field sensing application. Besides the fact that the oscillation dynamics can be nucleated and tuned without the application of any external magnetic field, their existence is limited to in-plane field values of maximal ± 100 *Oe* around the free layer

switching field. The maximum spectral output power density of up to 290 nV^2/Hz is found close to the free layers switching field, and in this regime, the oscillation linewidth narrows down to values of approximately 4 MHz, while the integral power below the peak remains constant within small variations. As it is shown in the literature, larger oscillation amplitudes are generally correlated with decreased linewidth as the dynamics become less sensitive to thermal fluctuations in frequency and amplitude. For external magnetic fields applied along the easy- and hard-axis directions of the elements, df/dH slopes present positive and negative values varying between -2.4 and $+2.7$ MHz/Oe. The vortex precession frequency is shown to be determined by the balance of energy components as they appear in the modified Thiele equation. In the relatively large nanocontacts studied here, various non-uniform magnetic states can arise, which may differ considerably from the ideal vortex state assumed in the model of Thiele. The applied magnetic field along the easy- or hard-axis direction is adding to the complexity of the system and competes with the Oersted field influence, which tends to stabilize the vortex state. Overall the magnetic field investigation shows that devices operated at low currents close to the nucleation of the excitation provide the highest sensitivity to magnetic fields and are therefore best suited for potential magnetic field sensor applications. However, a significant improvement of the device oscillation quality is necessary to provide a good alternative for conventional MR sensors.

For nanocontact radii between 75 and 85 nm multiple spectral modes are obtained, which are not harmonically correlated. They are shown to exist at zero magnetic field as well as for fields along the easy- and hard-axis directions. Such multi modes have been predicted in the literature for relatively large nanocontacts and are expected to be the result of strongly inhomogeneous, spatially extended magnetic configurations. These states are also reported to be metastable over time and can result in a splitting of the oscillation profiles in the average over time spectra measurements. In a possible scenario these spectra can be attributed to metastable precession trajectories of the vortex-like magnetization state, which can hop between energetically closely related states due to thermal activation. This scenario also explains the observation of a submode structure in our system, in which the excitation peaks close to the nucleation current randomly wobble within the Laurentian envelop.

Besides the characterization of the STT-driven excitation, our investigation concerned as well the current induced STT switching features, which are found in the dV/dI versus I measurements of exchange biased as well as AAF systems with relatively high magnetic moment free layer. The amplitude and position of these STT switching features change as function of applied in-plane fields. These features are explained by a macrospin model taking into account the Oersted field, STT, interlayer exchange and magnetostatic coupling effects. In this model, at a critical current density, the combination of Oersted field and STT reorients the free layer domain area close to the nanocontact against the coupling of the moments in the free layer. The measurements are demonstrated to be in excellent agreement to this model.

Perspectives and outlook

The research activities of the recent years clearly prove the potential of STT-driven devices, with their exceptional small size, performance and agility. However, besides a commercially available STT-MRAM, the technological break through is still anticipated to come in this still relatively new research field. This is not surprising since for example the revolution of GMR effect in the information technology took much more than a decade from its early discovery in 1986 to the big market entry in the late 1990s and the Noble Price in 2007. One of the main technological challenges for the STT driven nanocontact or nanopilar oscillators still needed to be solved is the low output power of a single device. Even if a perpendicular magnetic field is applied the power is with several nW approximately three orders of magnitude too low for practical applications. Multiple element synchronization and an improved stack design may offer the solution to overcome this challenge. Especially interesting are TMR stacks providing high spin-transfer efficiencies. This is why we think that a combination of our system together with a TMR stack design - which mainly only defers in the spacer layer material and its thickness - and a multi-nanocontact-array configuration, similar to the one shown in figure 60, would be a promising system.
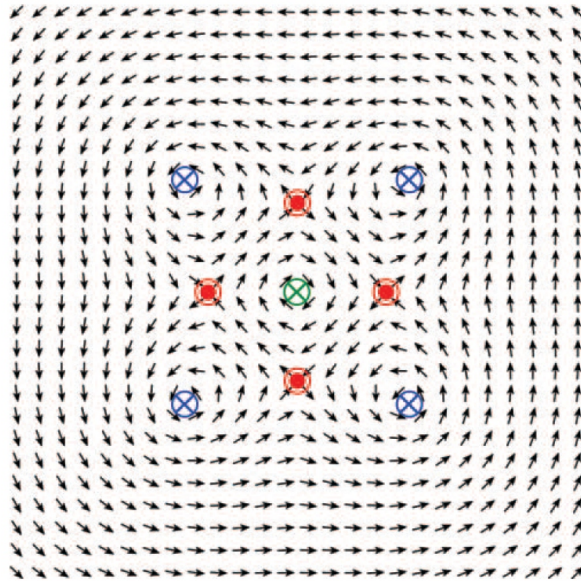
Figure 60: Multi vortex-antivortex lattice ground state in zero field. The Oersted field generated by the current flowing through a matrix of 2×2 nanocontacts nucleates a vortex under each of them (intercontact distance d=500 nm). Because all four vortices (blue) have the same chirality, energy minimization implies nucleation of antivortices (red) on the matrix sides and of a vortex with opposite chirality (green) in the matrix center (taken from [18,$^{Ruotolo;NatN;09}$, Ref. of Chapter 1]).

6 Acknowledgment

I thank all my colleagues from the **Nanosystems team**, specially, **Roman**, **Stefan**, **Leoni**, **Lukas**, **Marcus**, **Thomas M.**, **Reiner**, **Toni** and **Kerstin**, for their help and the great working atmosphere.

Liebe **Margit**, lieber **Volker**, meinen aller herzlichsten Dank für all die liebevolle Unterstützung und Euer Vertrauen in den letzten Jahren.

Liebste **Julia**, Du hast mir die Kraft und Zuversicht gegeben um diese Arbeit fertig zu stellen. Ich danke Dir von ganzem Herzen für all Deine Unterstützung in den letzten Jahren.

Finally, I'd like to express my appreciation for the inspiration of my old college physics teacher **Dr. Uwe Schlichting**. Without his lived passion for the field of experimental physics, I most probably wouldn't have started my study. May he rest in peace.

7 Publications and conference contributions

Journal publications

1) M. Eggeling, T. Dimopoulos, R. Heer and H. Brückl, Magnetic vortex excitation dependence on the magnetic free layer and size of spin-valve nanocontacts, physica status solidi (RRL) - Rapid Research Letters, 5: 435437. doi: 10.1002/pssr.201105374, 2011

2) back-cover RRL focus issue spintronics: M. Eggeling, T. Dimopoulos, R. Heer and H. Brückl, Magnetic vortex excitation dependence on the magnetic free layer and size of spin-valve nanocontacts, physica status solidi (RRL) - Rapid Research Letters physica status solidi (RRL) - Rapid Research Letters, doi: 10.1002/pssr.201190029, 2011

3) M. Eggeling, T. Dimopoulos, T. Uhrmann, O. Bethge, R. Heer, V. Höink and H. Brueckl, Low spin current-driven dynamic excitations and metastability in spin-valve nanocontacts with unpinned artificial antiferromagnet, Applied Physics Letters 98, 042504, 2011, selected for Vir. J. Nan. Sci. & Tech., Volume 23, Issue 5, 2011

4) M. Eggeling, T. Dimopoulos, R. Heer and H. Brückl, The dependence of vortex oscillation frequency on small in-plane magnetic fields in spin-valve nanocontacts, IEEE Transactions on Magnetics, accepted May 18th, 2012

Conference contributions

1) M. Eggeling, T. Dimopoulos, R. Heer and H. Brückl, The dependence of vortex frequency on small in-plane magnetic fields in spin-valve nanocontacts, Intermag, Canada, 2012, (talk)

2) M. Eggeling, T. Dimopoulos, R. Heer and H. Brückl, Dynamic excitation dependence on the magnetic free layer and size of spin-valve nanocontacts, Recent Trends in Nanomagnetism, Spintronics and their Applications (RTNSA), Spain, 2011 (talk)

3) M. Eggeling, T. Dimopoulos, R. Heer and H. Brückl, High frequency excitations in spin-valve nanocontacts, ARGE Sensoric, PhD-Summit, Austria, 2011 (talk)

4) M. Eggeling, T. Dimopoulos, T. Uhrmann, O. Bethge, R. Heer, V. Höink and H. Brückl, Low spin current-driven dynamic excitations and metastability in spin-valve nanocontacts with unpinned artificial antiferromagnet, DPG, Germany, 2011 (talk)

5) M. Eggeling, T. Dimopoulos, R. Heer and H. Brückl, Spin torque domain manipulation in exchange biased spin-valve nanocontacts, Spinswitch Sommer-school, Romania, 2010 (talk)

6) M. Eggeling, T. Dimopoulos, T. Uhrmann, O. Bethge, R. Heer, V. Höink and H. Brückl, High frequency excitation in spin-valve nanocontacts, Nanosens, Austria, 2010 (poster)

7) M. Eggeling, T. Dimopoulos, T. Uhrmann and H. Brückl, Spin torque effects in exchange biased spin-valve nanocontacts, ARGE Sensoric, Austria, 2009 (poster)

8) M. Eggeling, T. Dimopoulos, T. Uhrmann and H. Brückl, Spin torque effects in spinvalve nano-contacts with different free layers, spinswitch workshop "spin momentum transfer", Poland, 2008 (poster)

Co-author publications

1) A. Shoshi, J. Schotter, P. Schroeder, M. Milnera, V. Charwat, P. Ertl, M. Purtscher, M. Eggeling, G. Reiss and H. Brueckl, Magnetoresistive-based real-time cell phagocytosis monitoring, Biosensors and Bioelectronics, accepted April 2012

2) P. Schoeder, J. Schotter, A. Shoshi, M. Eggeling, A. Hütten and H. Brückl, Artificial cilia of magnetically tagged polymer nanowires for biomimetic mechanosensing, Bioinspir. Biomim. 6 046007, doi:10.1088/1748-3182/6/4/046007, 2011

3) N. Kataeva, J. Schotter, A. Shoshi, R. Heer, M. Eggeling, O. Bethge, C. Nöhammer and H. Brückl, Progress using magnetic nanoobjects for biomedical diagnostics, Biomagnetism and magnetic biosystems on molecular recognition processes, AIP Conf. Proc. 1025, pp. 28, ISBN 978-0-7354-0547-9, 2008

4) R. Heer, M. Eggeling, J. Schotter, C. Nöhammer, R. Pichler, M. Mansfeld and H. Brückl, Acceleration of incubation processes in DNA bio chips by magnetic particles, Journal of Magnetism and Magnetic Materials, Volume 311, Page 244-248, 2007

5) H. Brückl, M. Eggeling, R. Heer, C. Nöhammer and J. Schotter, Molecular diagnostics by a Magnetic Lap-on-the-Chip, NSTI, Bosten, 2006 (Proceedings)

Co-author conference contributions

1) Rudolf Heer, Moritz Eggeling, Jörg Schotter, Christa Nöhammer, Rudolf Pichler, Markus Mansfeld and Hubert Brückl, Acceleration of incubation processes in DNA bio chips by magnetic particles, Krems, 2006 (talk)

2) Rudolf Heer, Moritz Eggeling, Jörg Schotter, Christa Nöhammer, Rudolf Pichler, Markus Mansfeld and Hubert Brückl, Acceleration of incubation processes in DNA bio chips by magnetic particles, Stutgard, 2006 (talk)

3) A. Shoshi, J. Schotter, P. Ertl, P. Schroeder, M. Milnera, M. Eggeling, M. Purtscher and H. Brückl, GMR-based real-time cell endocytosis monitoring of magnetic particles, Scientific and Clinical Applications of Magnetic Carriers, Swiss, 2010 (talk)

4) J. Schotter, A. Shoshi, N. Kataeva, O. Bethge, R. Heer, M. Eggeling, H. Brückl, R. Pichler, M. Mansfeld and C. Nöhammer, Magnetic Biochips as Tools for Molecular Diagnostics, Nanosens, 2007 (talk)

5) H. Brückl, M. Eggeling, R. Heer, C. Nöhammer and J. Schotter, Molecular diagnostics by a Magnetic Lap-on-the-Chip, NSTI, Bosten, (Poster)

Patent

1) Rudolf Heer, Moritz Eggeling, Jörg Schotter, Christa Nöhammer, Rudolf Pichler, Markus Mansfeld and Hubert Brückl, Acceleration of incubation processes in DNA bio chips by magnetic particles, Österreichisches Patentamt, # 503.573, European Patent # 2004317, 2007

Award

1) R. Heer, M. Eggeling, J. Schotter, C. Nöhammer, R. Pichler, M. Mansfeld, Hybacc - Hybridisierungsbeschleuniger für Biochips, 2. Platz beim Genius Wettbewerb 2006 - www.riz.at

8 Curriculum vitae

Personal Data

Name	Eike Moritz Eggeling
Address	Breitenseerstr. 49, 1140 Vienna, Austria
Date of birth	25/10/1980
Place of Birth	Warendorf, Germany
Nationality	german

Education

03/2007-03/2012	Ph.D. thesis, Austrian Institute of Technology Vienna, Austria in collaboration with the University of Bielefeld, Germany
06/2006-02/2007	Around the world travel
05/2006-05/2002	Diplom-Physik, University of Bielefeld, Germany
06/2001-05/2002	Zivildienst, Von Bodelschwinghsche Anstallten Bethel Bielefeld, Germany
08/1997-06/2001	Abitur + 4 Semester Diplom-Physik, Oberstufen-Kolleg at the University of Bielefeld, Germany
08/1991-06/1997	Oberschulreife, Gesamtschule, Spenge, Germany
08/1987-06/1991	Grundschule, Melle-Neuenkirchen, Germany

Professional Experience

since 01/2012	Junior scientist at the Austrian Institute of Technology, Vienna, Austria
03/2007-01/2012	Freelancer for Ph.D. thesis at the Austrian Institute of Technology - AIT (Nano-Systems, Hubert Brückl) and the University of Bielefeld (Department of Physics, Günter Reiss): Spin-torque induced high frequency excitations and switching in spin-valve nanocontacts. Advisor: Theodoros Dimopoulos.
05/2005-05/2006	Freelancer for diploma thesis at the Austrian research center Seibersdorf - ARCS (Nano-Systems, Hubert Brückl) and the University of Bielefeld (Department of Physics, Günter Reiss): Mischen von dünnen Flüssigkeitsfilmen durch Manipulation magnetischer Micro- und Nano-Partikel mit magnetischen Feldern. Hybacc, Hybridisierungsbeschleuniger für Biochips. Advisors: Rudolf Heer and Jörg Schotter.

List of Figures

List of Tables

9 Appendix

9.1 Differential resistance measurement

For the low noise dV/dI measurement an fix alternating current, I_{ac} at the frequency ($f_{trigger}$) is superposed to a direct current component, I_{dc}. The current is swept through a predefined current regime. At a given value of I_{dc} the ac component modulates the voltage drop of the measured element (Fig. 61). The Lock-in amplifier is trigger to the frequency, $f_{trigger}$, and only voltage modulations closely around this frequency value are measured. The average value of this oscillating voltage is proportional to the voltage drop at the element. The absolute voltage value can be calibrated by a known resistor reverence measurement.
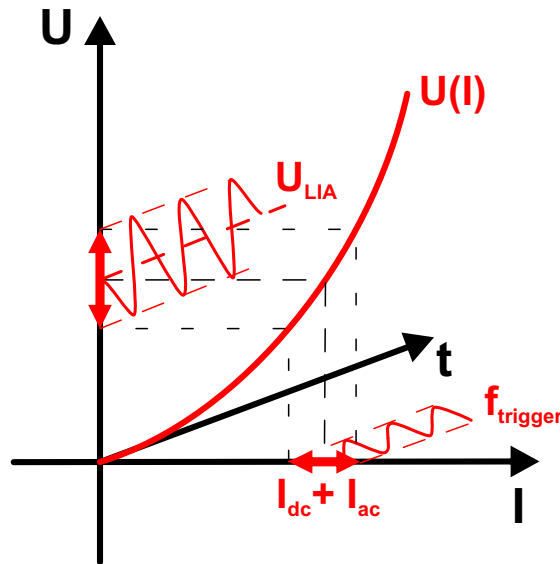

Figure 61: Illustration of the basic dV/dI measurement principle.

9.2 Measurement setup construction

Figure 62 shows an image of the 3D construction of the measurement setup, which is designed in the Solide edge software. It shows one of four tip-arms, which are mounted on x-y-z tables. The arm in the middle is holding the RF-tip, which reaches down to the sample holder in the center of the coil arrangement.
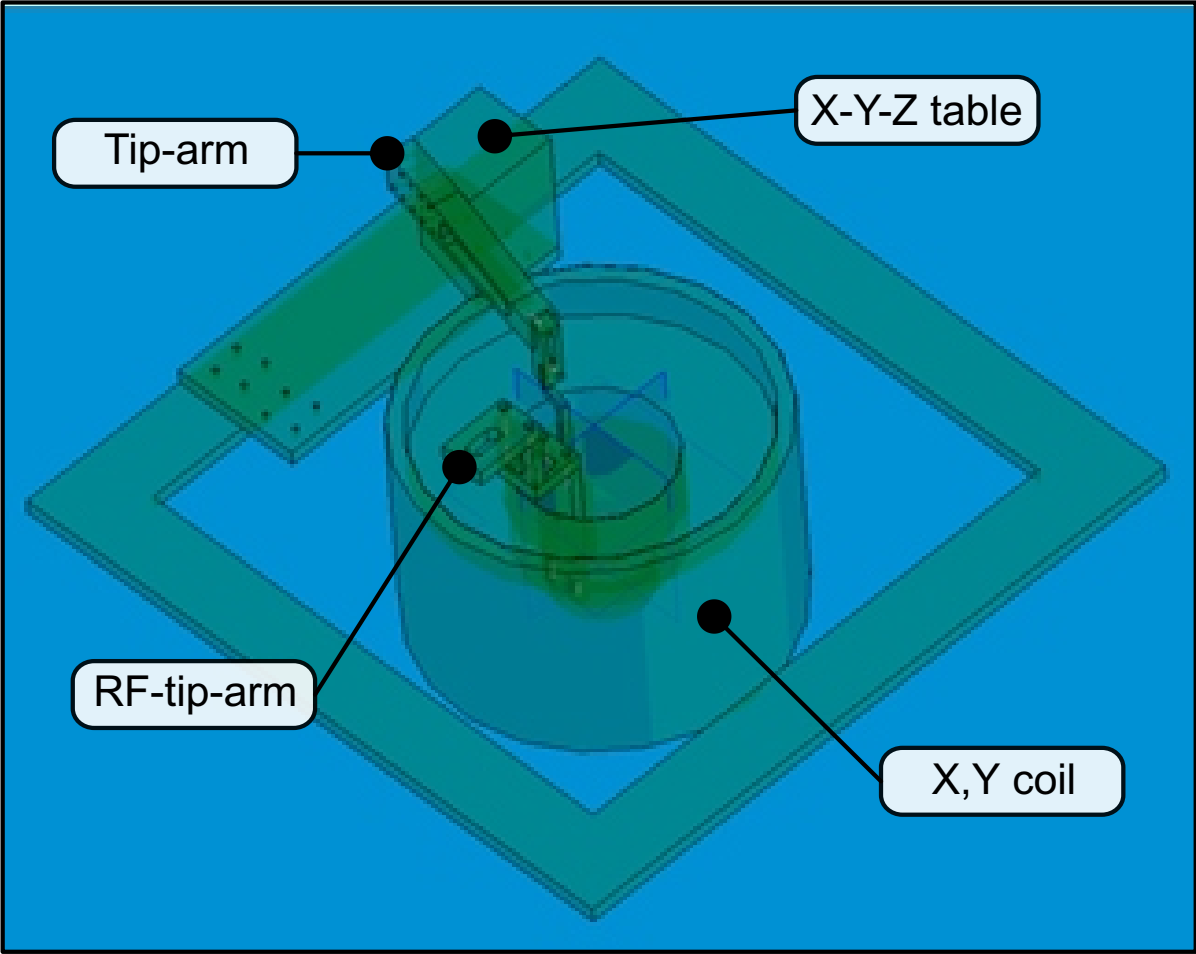
Figure 62: Measurement station designed in Solide edge with coil arrangement and tip arms.